

REPORT DOCUMENTATION PAGE			Form Approved OMB No. 0704-0188	
Public reporting burden for this collection of information is estimated to average 1 hour per response, including the time for reviewing instructions, searching existing data sources, gathering and maintaining the data needed, and completing and reviewing the collection of information. Send comments regarding this burden estimate or any other aspect of this collection of information, including suggestions for reducing this burden, to Washington Headquarters Services, Directorate for Information Operations and Reports, 1215 Jefferson Davis Highway, Suite 1204, Arlington, VA 22202-4302, and to the Office of Management and Budget, Paperwork Reduction Project (0704-0188), Washington, DC 20503.				
1. AGENCY USE ONLY (Leave blank)	2. REPORT DATE 18 Apr 97	3. REPORT TYPE AND DATES COVERED		
4. TITLE AND SUBTITLE CHANGES IN MEASURED LIGHTNING RETURN STROKE PEAK CURRENT AFTER THE 1994 NATIONAL LIGHTNING DETECTION NETWORK UPGRADE			5. FUNDING NUMBERS	
6. AUTHOR(S) ROBERT SCOTT WACKER				
7. PERFORMING ORGANIZATION NAME(S) AND ADDRESS(ES) TEXAS A&M UNIVERSITY			8. PERFORMING ORGANIZATION REPORT NUMBER  97-025	
9. SPONSORING/MONITORING AGENCY NAME(S) AND ADDRESS(ES) DEPARTMENT OF THE AIR FORCE AFIT/CI 2950 P STREET WRIGHT-PATTERSON AFB OH 45433-7765			10. SPONSORING/MONITORING AGENCY REPORT NUMBER	
11. SUPPLEMENTARY NOTES				
12a. DISTRIBUTION AVAILABILITY STATEMENT  <div style="border: 1px solid black; padding: 5px; width: fit-content; margin: auto;"> <p style="text-align: center;">DISTRIBUTION STATEMENT A</p> <p style="text-align: center;">Approved for public release; Distribution Unlimited</p> </div>			12b. DISTRIBUTION CODE	
13. ABSTRACT (Maximum 200 words)				
			19970428 176	
14. SUBJECT TERMS			15. NUMBER OF PAGES 139	
			16. PRICE CODE	
17. SECURITY CLASSIFICATION OF REPORT	18. SECURITY CLASSIFICATION OF THIS PAGE	19. SECURITY CLASSIFICATION OF ABSTRACT	20. LIMITATION OF ABSTRACT	

**ABSTRACT**

Changes in Measured Lightning Return Stroke Peak Current  
After the 1994 National Lightning Detection Network Upgrade.

(May 1997)

Robert Scott Wacker, B.S., United States Air Force Academy

Chair of Advisory Committee: Dr. Richard E. Orville

Since a comprehensive upgrade of the US National Lightning Detection Network (NLDN) in 1994, the mean peak current of detected cloud-to-ground (CG) lightning flashes has decreased, the number of detected flashes has increased, and the percentage of flashes with positive polarity has increased. NLDN archived data for the years 1989-95 was analyzed to characterize this change. Models of lightning return stroke radiation and its detection by NLDN sensors were developed to simulate the effects of the changes made to the sensors and explain the cause of the post-upgrade changes in NLDN data.

The US negative mean peak current decreased from a pre-upgrade (1989-93) mean of 37.5 kA to a 1995 value of 30.2 kA, a decrease of 3.39 standard deviations. The positive mean peak current decreased from 54.4 kA to 31.6 kA, a 4.97 standard deviation decrease. The US negative flash count increased 1.16 standard deviations, from a pre-upgrade mean

of 16.7 million flashes  $\text{yr}^{-1}$  to 20.6 million flashes in 1995. The positive flash count increased 6.22 standard deviations, from an average of 696 000 flashes  $\text{yr}^{-1}$  before the upgrade to 2.1 million flashes in 1995. Both the negative and positive flash count increases were predominant at low peak currents.

A model of return stroke detection by NLDN sensors was used to simulate one of the adjustments made to NLDN sensors during the upgrade. Decreasing the pulsewidth detection criterion used by the sensors increases their effective detection range, which increases their sensitivity to weak flashes (due to NLDN sensor geometry, increasing sensitivity has little effect on detection of strong flashes). The increased detection of weak flashes accounts for the decrease in mean peak currents and the increase in flash counts.

CHANGES IN MEASURED LIGHTNING RETURN STROKE PEAK CURRENT  
AFTER THE 1994 NATIONAL LIGHTNING DETECTION NETWORK UPGRADE

A Thesis

by

ROBERT SCOTT WACKER

Submitted to the Office of Graduate Studies of  
Texas A&M University  
in partial fulfillment of the requirements for the degree of

MASTER OF SCIENCE

May 1997

Major Subject: Meteorology

CHANGES IN MEASURED LIGHTNING RETURN STROKE PEAK CURRENT  
AFTER THE 1994 NATIONAL LIGHTNING DETECTION NETWORK UPGRADE

A Thesis

by

ROBERT SCOTT WACKER

Submitted to Texas A&M University  
in partial fulfillment of the requirements  
for the degree of

MASTER OF SCIENCE

Approved as to style and content by:



Richard E. Orville  
(Chair of Committee)



Thomas T. Wilheit, Jr.  
(Member)



George W. Kattawar  
(Member)



Gerald R. North  
(Head of Department)

May 1997

Major Subject: Meteorology

**ABSTRACT**

Changes in Measured Lightning Return Stroke Peak Current  
After the 1994 National Lightning Detection Network Upgrade.

(May 1997)

Robert Scott Wacker, B.S., United States Air Force Academy

Chair of Advisory Committee: Dr. Richard E. Orville

Since a comprehensive upgrade of the US National Lightning Detection Network (NLDN) in 1994, the mean peak current of detected cloud-to-ground (CG) lightning flashes has decreased, the number of detected flashes has increased, and the percentage of flashes with positive polarity has increased. NLDN archived data for the years 1989-95 was analyzed to characterize this change. Models of lightning return stroke radiation and its detection by NLDN sensors were developed to simulate the effects of the changes made to the sensors and explain the cause of the post-upgrade changes in NLDN data.

The US negative mean peak current decreased from a pre-upgrade (1989-93) mean of 37.5 kA to a 1995 value of 30.2 kA, a decrease of 3.39 standard deviations. The positive mean peak current decreased from 54.4 kA to 31.6 kA, a 4.97 standard deviation decrease. The US negative flash count increased 1.16 standard deviations, from a pre-upgrade mean

of 16.7 million flashes  $\text{yr}^{-1}$  to 20.6 million flashes in 1995. The positive flash count increased 6.22 standard deviations, from an average of 696 000 flashes  $\text{yr}^{-1}$  before the upgrade to 2.1 million flashes in 1995. Both the negative and positive flash count increases were predominant at low peak currents.

A model of return stroke detection by NLDN sensors was used to simulate one of the adjustments made to NLDN sensors during the upgrade. Decreasing the pulsewidth detection criterion used by the sensors increases their effective detection range, which increases their sensitivity to weak flashes (due to NLDN sensor geometry, increasing sensitivity has little effect on detection of strong flashes). The increased detection of weak flashes accounts for the decrease in mean peak currents and the increase in flash counts.

**DEDICATION**

This thesis is dedicated to my parents, Herb and Judy Wacker, for the lifetime of love, encouragement, and support they have given me.

**ACKNOWLEDGMENTS**

The author wishes to acknowledge the Fannie and John Hertz Foundation for its financial support of his graduate studies; the United States Air Force for providing the opportunity to pursue his master's degree; and Dr. Richard E. Orville and the Cooperative Institute for Applied Meteorological Studies at Texas A&M University for the guidance and resources necessary to complete it.

## TABLE OF CONTENTS

	Page
ABSTRACT.....	iii
DEDICATION.....	v
ACKNOWLEDGMENTS.....	vi
TABLE OF CONTENTS.....	vii
LIST OF FIGURES.....	ix
LIST OF TABLES.....	xii
CHAPTER	
I    INTRODUCTION.....	1
II   BACKGROUND.....	3
1.    The lightning return stroke.....	4
2.    Wideband magnetic direction finder operation.....	12
3.    The National Lightning Detection Network.....	16
III  MEASURING PEAK CURRENT.....	22
1.    Electromagnetic theory.....	22
2.    Peak current calibration.....	31
IV   NLDN DATA ANALYSIS.....	35
1.    Previous work.....	35
2.    Data set and analysis methods.....	35
3.    Results.....	38
V    RETURN STROKE DETECTION MODELING.....	71
1.    Previous work.....	71
2.    Finite difference return stroke field model.....	76
3.    Stochastic return stroke detection model.....	88
VI   DISCUSSION AND CONCLUSIONS.....	96

1.	Statistical significance of data...	96
2.	Detection modeling results.....	97
3.	Possible explanation of peak current decrease and flash count increase.....	98
4.	Recommendations.....	101
REFERENCES.....		103
APPENDIX A:	ORVILLE (1991) AND IDONE ET AL. (1993) PEAK CURRENT CALIBRATIONS.....	106
APPENDIX B:	NLDN DATA ANALYSIS SAMPLE.....	119
APPENDIX C:	FINITE DIFFERENCE FIELD MODEL.....	127
APPENDIX D:	STOCHASTIC DETECTION MODEL.....	132
VITA.....		139

## LIST OF FIGURES

FIGURE		Page
2.1	Chronology of a CG lightning flash.....	7
2.2	Magnetic field loop antenna and electric field flat antenna configuration in wideband magnetic direction finders.....	13
2.3	The National Lightning Detection Network after the 1994 upgrade.....	19
3.1	Typical first and subsequent return stroke waveforms with dart-stepped leaders and dart leaders.....	29
4.1	Kansas annual and monthly negative flash count, 1989-95.....	41
4.2	Kansas annual and monthly negative mean peak current, 1989-95.....	42
4.3	Kansas annual and monthly positive flash count, 1989-95.....	43
4.4	Kansas annual and monthly positive mean peak current, 1989-95.....	44
4.5	Ohio Valley annual and monthly negative flash count, 1989-95.....	47
4.6	Ohio Valley annual and monthly negative mean peak current, 1989-95.....	48
4.7	Ohio Valley annual and monthly positive flash count, 1989-95.....	49
4.8	Ohio Valley annual and monthly positive mean peak current, 1989-95.....	50
4.9	Florida annual and monthly negative flash count, 1989-95.....	53
4.10	Florida annual and monthly negative mean peak current, 1989-95.....	54
4.11	Florida annual and monthly positive flash count, 1989-95.....	55

FIGURE		Page
4.12	Florida annual and monthly positive mean peak current, 1989-95.....	56
4.13	US annual and monthly negative flash count, 1989-95.....	59
4.14	US annual and monthly negative mean peak current, 1989-95.....	60
4.15	US annual and monthly positive flash count, 1989-95.....	61
4.16	US annual and monthly positive mean peak current, 1989-95.....	62
4.17	US negative peak current distribution, 1989-95.....	65
4.18	US negative pre- to post-upgrade flash count ratio.....	66
4.19	US positive peak current distribution, 1989-95.....	67
4.20	US positive pre- to post-upgrade flash count ratio.....	68
5.1	Finite difference field model channel geometry.....	78
5.2	Model channel current vs. height 15 $\mu$ s after return stroke initiation.....	80
5.3	Electric field strength and magnetic flux density measured 100 km from the 30 kA peak current model return stroke in Fig. 5.2.....	82
5.4	Raw and normalized signal strength vs. range.....	84
5.5	Signal pulsewidth vs. range for the 30 kA return stroke modeled in Fig. 5.2.....	85
5.6	Detection range vs. peak current for modeled return strokes having waveforms identical to Fig. 5.2 using detection pulsewidth criteria of 10 $\mu$ s and 7 $\mu$ s.....	87

FIGURE		Page
5.7	Detection model randomly generated return stroke locations.....	89
5.8	Modeled return stroke detected flash count vs. peak current and detected flash counts at 10 $\mu$ s and 7 $\mu$ s pulsewidth criteria.....	92
5.9	Model detection efficiency vs. peak current at 10 $\mu$ s and 7 $\mu$ s pulsewidth criteria and model post-upgrade flash count vs. peak current normalized to pre-upgrade flash count.....	93

## LIST OF TABLES

TABLE		Page
4.1	Data analysis geographical subsets.....	36
4.2	Post- vs. pre-upgrade negative flash count and mean peak current comparison.....	38
4.3	Post- vs. pre-upgrade positive flash count and mean peak current comparison.....	39

## CHAPTER I

### INTRODUCTION

Since 1989 the National Lightning Detection Network (NLDN) has detected cloud-to-ground (CG) lightning flashes within the continental United States. The network is administered by Global Atmospheric, Inc., of Tucson, Arizona, and consists of approximately one hundred lightning sensors located throughout the country. These sensors are linked via satellite to a centralized network control center (NCC) in Tucson, which disseminates detected CG flash data to NLDN subscribers.

NLDN data has a number of applications: protection of electrical utility assets; forest fire prevention; protection of aircraft and spacecraft; public safety (according to Orville 1993, lightning is the largest weather related killer in the United States, killing 100-150 people annually); and meteorological research.

During the latter half of 1994, the NLDN underwent a system-wide upgrade intended to improve detection efficiency, location accuracy, data delivery, and network reliability. This upgrade consisted of adjustments to existing sensor hardware, decommissioning or movement of selected sensors, inclusion of a new type of sensor absorbed

---

This thesis follows the style and format of *Monthly Weather Review*.

from another network, and implementation of a new flash location algorithm (Cummins et al. 1995).

Since the upgrade, the following changes have been observed in NLDN data: 1) a decrease in the mean peak current of detected CG flashes, 2) an increase in the number of detected flashes, and 3) an increase in the percentage of the flashes having positive polarity.

The purpose of this thesis is to describe quantitatively the post-upgrade change in NLDN peak current and flash count data and determine its probable cause. Chapter II includes background on CG lightning flashes, magnetic direction finder (DF) operation, and the NLDN. Chapter III discusses the theoretical basis for remote measurement of return stroke peak current and the calibration of the sensors used in the NLDN. Chapter IV contains a quantitative analysis of the changes in mean peak currents and flash counts in the NLDN archived data. Chapter V presents two models representing the electromagnetic radiation emitted by a CG lightning return stroke and its detection by NLDN sensors before and after simulating the changes made to them during the NLDN upgrade. Finally, Chapter VI draws conclusions as to the cause of the change in NLDN data based on the similarities between the analysis in Chapter IV and the model results in Chapter V.

## CHAPTER II

### BACKGROUND

The purpose of this chapter is to provide the necessary background knowledge of 1) the physical processes involved in lightning flashes, 2) the operation of magnetic direction finders, and 3) the operation of the NLDN required for understanding of the later chapters discussing radiation theory, data analysis, and modeling.

#### 1. Terminology and coordinates

Several conventions are used in the lightning literature and this thesis. The first distinguishes lightning *strokes* from lightning *flashes*. A stroke is a single lightning discharge. A lightning flash consists of multiple lightning strokes occurring in rapid succession within the same channel from cloud to ground. Lightning flashes appear to flicker because the unaided eye is just able to resolve the individual luminosity pulses of each stroke. This is referred to as the flash's multiplicity.

Polarity refers to the sign of charge a flash lowers to ground. Since positive and negative flashes are different in several respects, they are considered separately in analyzing lightning data.

## 2. The Lightning Return Stroke

### a. *Types of lightning discharges*

Cloud-to-ground (CG) lightning flashes transfer charge between cloud and ground. These flashes are the type the NLDN is designed to detect exclusively. They can have peak currents of tens or even hundreds of kA.

Cloud flashes occur between charge regions within a cloud, between clouds, or between a cloud and the surrounding air. Cloud flashes comprise approximately 80% of all lightning discharges and have peak currents of only a few kA (Orville 1993). The electronics of the sensors used in the NLDN are specifically designed to screen out cloud flashes.

Triggered flashes occur between cloud charge regions and man-made objects on the ground or in the air which artificially intensify the local electric field. The sensor calibration discussed in Chapter III was accomplished using lightning flashes triggered by rockets launched into thunderstorms at the Kennedy Space Center.

Numerous other names exist to describe lightning or lightning-like discharges: heat lightning, bead lightning, ribbon lightning, and ball lightning, for instance. Some of these phenomena, like ribbon lightning, are well understood, while others, like ball lightning, are not. Recently, faint

transient optical emissions called sprites and jets have been discovered above thunderstorms.

*b. CG lightning flash processes*

A CG lightning flash occurs at the end of a complex chain of events set in motion by the nature of the Earth-atmosphere global electrical circuit.

1) The Earth-atmosphere circuit

In fair weather, the ambient electric field is directed downward with a strength of approximately  $100 \text{ V m}^{-1}$  at the earth's surface, decreasing with height. The total potential difference between the surface and 50 km is approximately  $3 \times 10^5 \text{ V}$ . This potential difference is a consequence of the net negative charge of approximately  $4.5 \times 10^5 \text{ C}$  residing on the Earth's surface. The Earth and atmosphere act as a "leaky spherical capacitor", with a total current of 1000-1500 A continuously flowing toward the surface.

Radioactive decay, cosmic radiation, and short-wave ultraviolet radiation all create charge in the atmosphere through ionization (Uman 1987). However, we would expect the downward current to neutralize the surface charge and eliminate the fair weather electric field in a matter of minutes. Therefore, there must be some mechanism which continually maintains the ambient charge distribution.

Thunderstorms serve this role by carrying negative charge from cloud to ground, thus acting as a battery in the Earth-atmosphere circuit.

## 2) Charge separation

Fig. 2.1 illustrates the processes occurring before and during a lightning flash. The first of these is charge separation within a cloud ( $t=0$  in Fig. 2.1). The exact mechanism of charge separation is not well understood, but it is thought to be a consequence of collisions between mixed-phase precipitation (i.e. rain and graupel) within the updraft. Due to the requirement for both frozen and liquid precipitation, the level where charge separation occurs is dependent upon the height of the freezing level.

A typical cumulonimbus cloud contains a double-dipole charge structure: a large region of positive charge, perhaps 40 C, exists near the  $-45^{\circ}\text{C}$  level; another large region of equal negative charge exists lower, near the  $-15^{\circ}\text{C}$  level; and a small region of positive charge typically exists near cloud base (Uman 1987). This charge distribution induces a positive charge region at the surface below the cloud and results in a potential difference between cloud base and ground on the order of  $10^7$  V. Within this large-scale structure, smaller sub-regions of cloud charge exist.

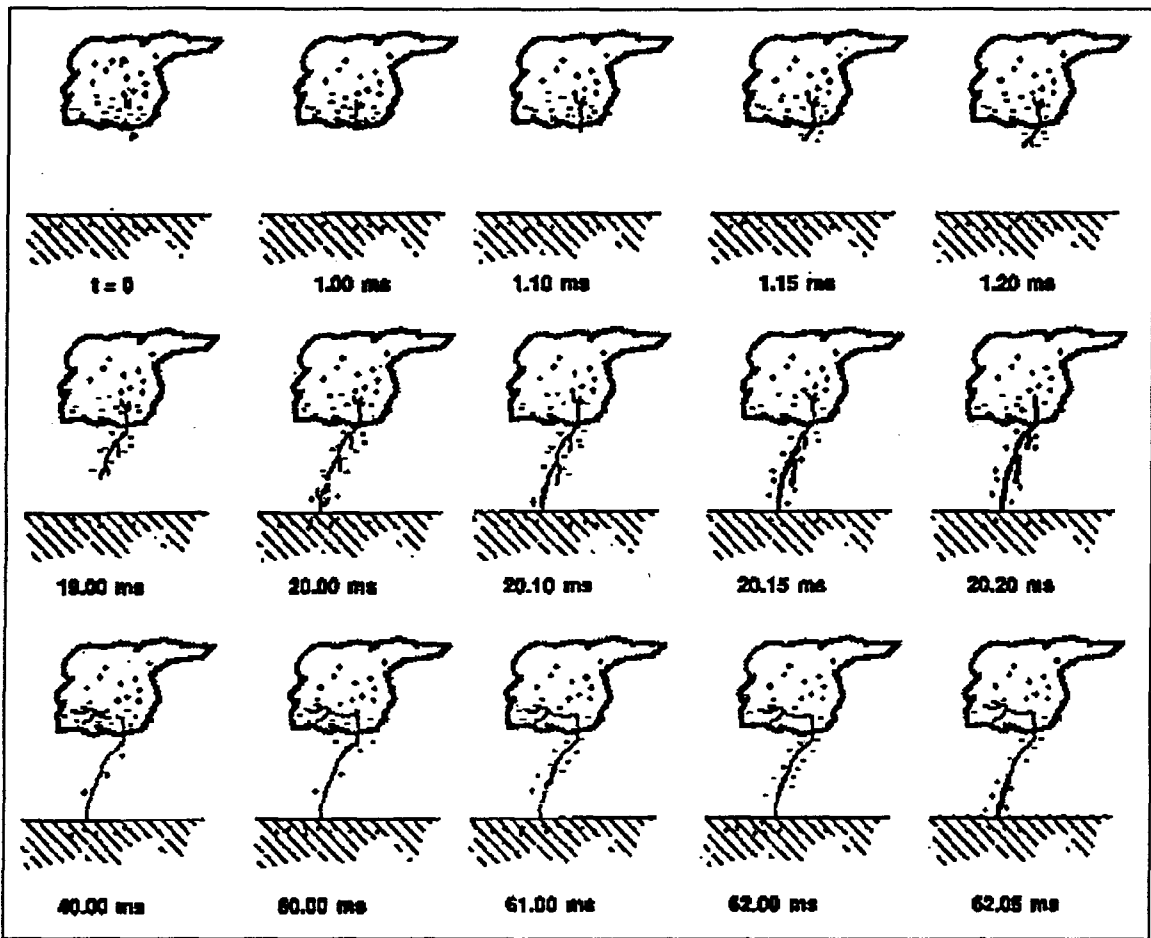


Fig. 2.1. Chronology of a CG lightning flash (adapted from Uman 1987). Note the approximate time reference below each frame.

### 3) Stepped leader

When the electric field between cloud charge regions exceeds the ionization potential of air (approximately  $500\,000\text{ V m}^{-1}$ , depending on pressure), breakdown occurs ( $t=1.00\text{ ms}$  in Fig. 2.1). The ionized air forms a conducting channel into which cloud charge flows, further intensifying the potential gradient, and hence the electric field. This causes another breakdown to occur, adding another ionized segment to the conducting channel. This faintly luminous process, the *stepped leader*, repeats itself approximately every  $50\text{ }\mu\text{s}$ , adding segments tens of m long to the channel and branching occasionally as it moves toward ground with an average velocity of approximately  $2 \times 10^5\text{ m s}^{-1}$  ( $t=1.00\text{ ms}$  to  $t=19.00\text{ ms}$  in Fig. 2.1).

### 4) Return stroke

As the stepped leader nears ground, the potential difference between the tips of the leader branches and ground remains constant, but as the distance decreases the potential *gradient* grows very large, especially in the presence of tall, pointed objects on the ground where charge can accumulate. Breakdown occurs at such an object when the field grows large enough, inducing an upward streamer (Fig. 2.1,  $t=20.00\text{ ms}$ ). When the upward streamer meets the tip of one of the stepped leader branches the cloud charge is

short-circuited to ground, initiating the *return stroke* (Fig 2.1,  $t=20.10$  ms to 20.20 ms). A wave of ground potential travels up the channel toward the cloud charge region at a velocity of approximately  $10^8$  m s<sup>-1</sup>. Once this potential wave passes a point on the channel, the charge stored there flows to ground. Charge stored in a branch flows to ground after the potential wave passes the point where it connects to the channel. The resulting large current flowing in the channel ionizes the various gaseous constituents of the atmosphere, producing the intense luminosity we see. It also heats the channel to approximately 30 000 K, causing an overpressure of about 100 atm. This causes the outward-propagating shockwave heard as thunder.

#### 5) Dart leader

The first return stroke discharges one region of charge within the cloud. The channel, however, remains a conductor until the ionized air composing it can recombine. While this is taking place, the channel may connect to another cloud charge region (Fig. 2.1,  $t=40.00$  ms). A new leader, the *dart leader*, moves down the partially-recombined channel, recharging it. Since it already has the existing channel to follow, the dart leader about ten times faster than the stepped leader (Fig. 2.1,  $t=60.00$  ms to 62.00 ms). Sometimes recombination will have already occurred at the bottom of the channel where pressure is higher, causing the

dart leader to finish its downward movement as a stepped leader.

6) Subsequent return stroke(s)

Once the dart leader has recharged the channel and contacted ground another return stroke occurs (Fig. 2.1, 62.05 ms). *Subsequent return strokes* differ from first return strokes in that they have no branches, since only the existing main channel is re-ionized by the dart leader. The dart leader-subsequent return stroke process can repeat itself several times with tens of ms between return strokes (Uman 1987). In a significant fraction of CG return strokes, a continuing current of approximately 100 A may flow for as long as tenths of a second (Uman 1987).

7) Return stroke characteristics

Typical return stroke characteristics are summarized here:

Time required for the return stroke to propagate up the channel can range from 10  $\mu\text{s}$  (Beasley et al. 1993) to 20-50  $\mu\text{s}$  (Cummins et al. 1995) to 100  $\mu\text{s}$  (Uman 1987). Time between subsequent return strokes ranges between 20 and 100 ms (Cummins et al. 1995).

Return stroke velocity averages  $10^8 \text{ m s}^{-1}$  (Beasley et al. 1995) and decreases as each branch is passed (Uman 1987).

Cummins et al. (1995) report a peak current range of 5 to 300 kA. Mean peak current appears to decrease with latitude (Orville 1990).

Multiplicity averages between 2 and 3, but values may range between 1 and 20 (Cummins et al. 1995).

Orville (1994) reports a total CG flash count of approximately  $10^7$  CG flashes per year in the United States. About 4% of CG flashes are of positive polarity, with considerable latitudinal and seasonal variation.

*c. Positive flashes*

CG flashes may lower positive or negative charge to ground. Positive CG flashes, which comprise approximately 5% of all CG flashes, differ significantly from negative flashes. Typically positive flashes have higher peak currents (approximately 45 kA mean peak current vs. approximately 30 kA for negative flashes) and transfer more charge. Positive leaders typically are not branched and positive flashes usually do not have subsequent return strokes.

The percentage of positive flashes is higher in winter, at high latitudes, at high elevations, and in severe storms (Uman 1987; Orville 1994). This leads us to conclude that positive CG flashes occur between the upper (positive) charge region of the cloud and ground. A lower freezing level or higher terrain decrease the distance from the

positive charge to ground, and strong shear tilts the dipole structure, providing a more direct path from the positive charge to ground.

### **3. Wideband magnetic direction finder operation**

An entire CG lightning flashes can last as long as 1 s, while the individual processes within it occur on a sub-microsecond timescale, so the frequencies of radiation emitted during a flash can range from below 1 Hz to well in excess of 10 MHz (Uman 1987). Therefore, sensors designed to detect lightning radiation waveforms must operate over a wide frequency range.

The first wideband magnetic direction finders were developed in the late 1970s for use by the US Bureau of Land Management (BLM) for forest fire protection in the Western United States (Krider et al. 1980). The descendants of those original DFs are in service today in the NLDN.

For reasons discussed in Chapter III, these DFs are designed to measure the vertical component of the local electric field using horizontal flat plate antennae and the horizontal components of the local magnetic flux density using orthogonal loop antennae in the vertical plane. Fig. 2.2 depicts the antenna configuration.

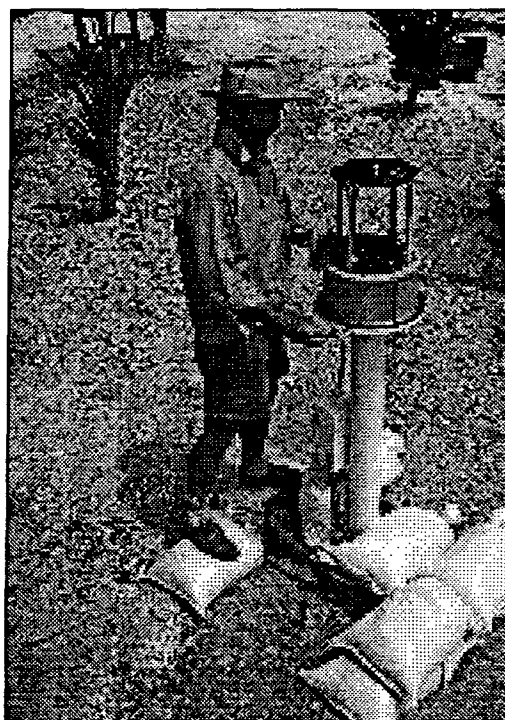
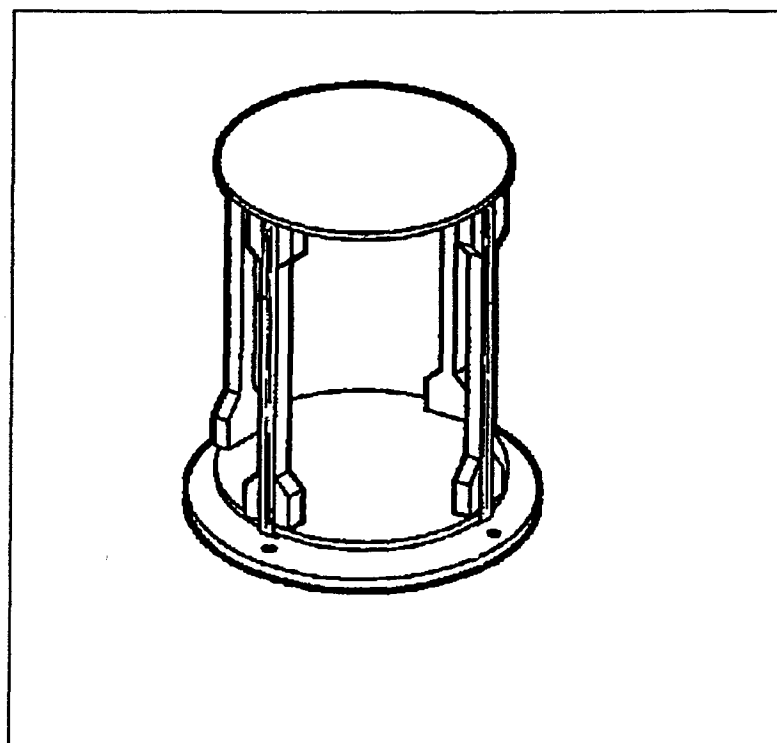


Fig. 2.2. Magnetic field loop antenna and electric field flat plat antenna configuration in wideband magnetic direction finders (top, adapted from Lightning Location and Protection, Inc., 1992). An IMPACT DF manufactured by LLP, Inc., used in the TOGA COARE field experiment (bottom).

a. *Magnetic field loop antennae*

From the integral form of Faraday's law,  $\epsilon = -d\Phi/dt$ , we see that a changing magnetic flux,  $\Phi$ , through a current loop produces an electromotive force,  $\epsilon$ , in the loop (Griffiths 1989). Two orthogonal vertical loops can then measure the component of the horizontal magnetic flux normal to each loop by integrating in time the voltage in the loop (Krider et al. 1980). The vector sum of the two components yields the total horizontal magnetic flux density. Additionally, the ratio of the two components is the tangent of the azimuth to the radiation source (Uman 1987).

b. *Electric field flat plate antenna*

Since reciprocal angles have the same tangent, the vertical electric field must be measured to determine the polarity of the return stroke and eliminate the ambiguity in the azimuth determined by the vertical loop antennae. This is accomplished using an elevated horizontal flat plate. From the integral form of Gauss' law,  $Q = E_n \epsilon_0 A$ , the charge,  $Q$ , induced on the plate is proportional to the electric field component normal to it,  $E_n$  (Griffiths 1989). A change in normal electric field strength,  $dE_n/dt$ , will result in a current,  $dQ/dt$ , flowing to or from the plate, which is integrated to yield the total field (Uman 1987).

c. *Detection criteria*

The electronics of a DF are configured to distinguish the unique radiation waveforms of CG return strokes from the radiation of cloud flashes and background noise. The waveform characteristics used to distinguish a return stroke signature are: 1) its risetime from the detection threshold to the initial peak value, 2) its pulsewidth, 3) the magnitude of any subsidiary peaks, and 4) the magnitude of the field overshoot (Krider et al. 1980). Return stroke radiation waveforms are discussed in greater detail in Chapter III.

d. *LLP units*

The magnetic DFs used in the NLDN are manufactured by Lightning Location and Protection, Inc. (LLP). Their output for both magnetic flux density and electric field strength are calibrated in *LLP units*. One LLP unit corresponds to a magnetic flux density of  $1.5 \times 10^{-10}$  wb m<sup>-2</sup> and an electric field strength of  $4.5 \times 10^{-2}$  V m<sup>-1</sup> (Hiscox and Cummins 1993). All signal strength data used by the NLDN are in LLP units and in Chapter III a calibration of return stroke peak current in terms of range normalized signal strength (in LLP units) is presented.

#### 4. The National Lightning Detection Network

##### a. *History*

The National Lightning Detection Network has its roots in three smaller networks that came into existence during the 1970s and '80s. The first was the BLM network established in the late 1970s for forest fire prevention in the Western United States and Alaska and developed by Krider et al. (1980). Another network was operated by the National Severe Storms Laboratory (NSSL) in the Midwestern United States. The first network with centralized data processing was developed at the State University of New York at Albany (SUNYA) and initially consisted of ten sensors covering an area along the East Coast from North Carolina to Canada (Cummins et al. 1995; Orville et al. 1983).

In 1987 the three separate networks were combined into the NLDN and by 1989 enough sensors had been added to provide complete coverage of the continental United States (Cummins et al. 1995). In 1991, GeoMet Data Services (GDS) was established to administer the NLDN as a commercial venture. GDS, LLP, and Atmospheric Research Systems (ARS, another sensor manufacturer) comprise Global Atmospheric, Inc., with headquarters in Tucson, Arizona.

##### b. *Flash location methods*

Flashes are located by the NLDN using three different methods:

### 1) Time-of-arrival (TOA) method

The TOA method is used by LPATS sensors developed by ARS and incorporated into the NLDN in the 1994 upgrade. LPATS sensors only record the arrival time of the peak signal strength of the detected return stroke signal; they have no direction-finding capability. The difference in TOAs recorded by a pair of sensors is used to compute a hyperbola along which the flash must have occurred. The intersection of hyperbolae computed from multiple pairs of sensors defines the flash location. At least four sensors are required to obtain an unambiguous flash location (Orville 1993).

### 2) Triangulation method

When azimuth data from at least two DFs is available, flash locations can be determined by triangulation. This gives good results as long as the flash is not near the baseline between two DFs whose azimuths are being used (Orville 1993). In this case, azimuth error results in very large position error.

### 3) IMPACT (Improved Performance from Combined Technology) method

To accommodate the addition of TOA sensors to the existing network of magnetic DFs, Global Atmospheric developed a flash location algorithm using arbitrary combinations of TOA and azimuth data. Such a combination

defeats the shortcomings of each method used individually (Cummins et al. 1995; Orville 1993).

When multiple sensors detect a flash the redundant data is used to optimize the flash location estimation. As a minimum, the IMPACT method requires one more data point than the number of parameters desired. For instance, a two-dimensional flash location and time requires four data points (i.e. two azimuths and two TOAs, one azimuth and three TOAs, etc.) (Cummins et al. 1995).

*c. Network configuration*

Since the 1994 upgrade the network consists of 45 existing magnetic DFs updated to the IMPACT standard, which provide azimuth and TOA based on the Global Positioning System (GPS) time reference, and 60 LPATS sensors acquired from the ARS network and added to the network, which provide GPS-based time of arrival only. Fig. 2.3 depicts the locations of both types of sensors.

The sensors send their data via satellite link to the Network Control Center (NCC) in Tucson. At the NCC, data from all sensors in the network is combined to determine flash time, location, peak current, polarity, and multiplicity. The processed flash data is then disseminated to NLDN subscribers via satellite. The entire process takes 30-40 s (Cummins et al. 1995).

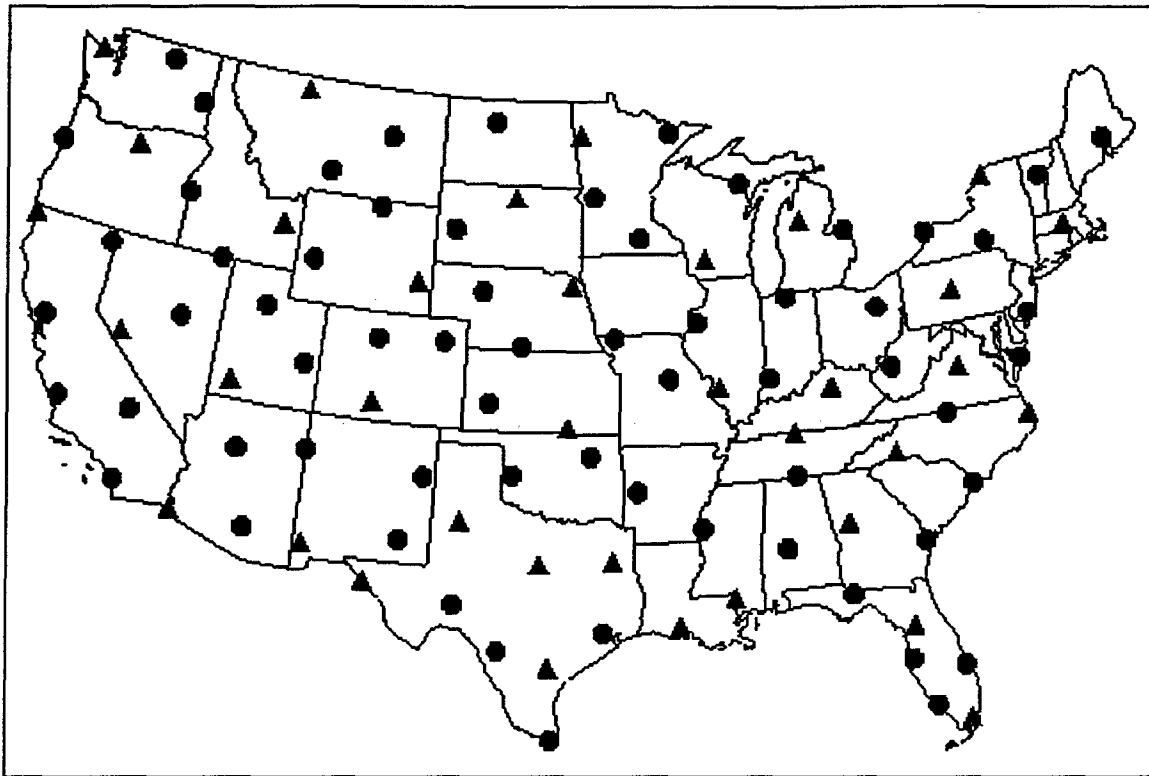


Fig. 2.3. The National Lightning Detection Network after the 1994 upgrade. Red triangles represent IMPACT DFs and blue circles represent LPATS time-of-arrival (TOA) sensors (adapted from Cummins et al. 1995).

d. *The 1994 NLDN upgrade*

Since Global Atmospheric is a commercial venture, changes and upgrades to improve network performance have been ongoing since the NLDN's inception. For example, in late 1992 four IMPACT DFs were installed in Tennessee and during March-April 1993 the original DFs from the BLM network were replaced by IMPACT sensors while others were added in South Carolina (Cummins 1995).

The 1994 upgrade, however, was far greater in scope. According to a Global Atmospheric technical note describing the upgrade, its primary objective was to improve location accuracy through implementation of the IMPACT method. It also sought to improve the data processing infrastructure to deliver stroke and flash data in real-time, improve detection efficiency of weak flashes (as low as 5 kA), and improve the long-term reliability of the NLDN hardware (Cummins et al. 1995). It took place during July-December 1994, with the majority of the work being accomplished during July and August (Cummins 1996).

In keeping with the goal of increasing weak flash detection efficiency, several hardware changes were made to NLDN DFs: 1) sensor gain was increased 50%, improving nominal detection range from 400 km to 600 km (Cummins 1996); 2) the pulsewidth criterion for recognizing return strokes was reduced from 10  $\mu$ s to 7  $\mu$ s (Lucas and Orville

1996; Cummins 1996); and 3) the subsidiary peak tolerance was increased from .85 of the initial signal strength to 1.2 (Cummins 1996), allowing detection of distant weak flashes, whose ground wave may be attenuated to a strength comparable to the reflected sky wave. The effects of these detection criteria changes are discussed further in Chapter V.

## CHAPTER III

## MEASURING PEAK CURRENT

The purpose of this chapter is to discuss the physical and mathematical basis for measuring peak current with remote lightning sensors. It presents the mathematical relation between return stroke peak current and peak measured field strength and the assumptions used to derive it. Finally, it presents results of previous sensor peak current calibrations, corrects for an erroneous data point in one calibration, and investigates the effects of using a more physically reasonable calibration.

## 1. Electromagnetic theory

## a. Maxwell's equations

Electromagnetic radiation is governed by Maxwell's equations (Equations 3.1a through d), compiled by Maxwell in the late 19th century. They describe the interrelation of the charge density,  $\rho$ , current,  $\mathbf{J}$ , electric field,  $\mathbf{E}$ , and magnetic field,  $\mathbf{B}$ , (Griffiths 1989):

$$\text{Gauss' law} \quad \nabla \cdot \mathbf{E} = \frac{\rho}{\epsilon_0} \quad (3.1a)$$

$$\text{(no name)} \quad \nabla \cdot \mathbf{B} = 0 \quad (3.1b)$$

$$\text{Faraday's law} \quad \nabla \times \mathbf{E} = -\frac{\partial \mathbf{B}}{\partial t} \quad (3.1c)$$

$$\text{Ampere's law} \quad \nabla \times \mathbf{B} = \mu_0 \mathbf{J} + \mu_0 \epsilon_0 \frac{\partial \mathbf{E}}{\partial t} \quad (3.1d)$$

Maxwell's equations provide a conceptual picture of the fields we should expect from a return stroke. If we consider a current flowing in a long straight conductor, Gauss' law predicts a change in the electric field along the conductor due to the charge carried from one end to the other by the current. Ampere's law predicts that the current (and electric field change) will produce a magnetic field in the azimuthal direction (in accordance with the right-hand rule). If the conductor is vertical (as we approximate a return stroke channel to be), the electric field change will also be vertical, and the magnetic field will be azimuthal. This is why the magnetic direction finders discussed in Chapter II sense the vertical electric field component and the horizontal magnetic field components.

*b. Solution to Maxwell's equations*

The first step in obtaining a solution to Maxwell's equations is to formulate the scalar and vector potentials,  $\phi$  and  $\mathbf{A}$  (Griffiths 1989; Uman 1987; Uman et al. 1975):

$$\phi(\mathbf{r}, t) = \frac{1}{4\pi\epsilon_0} \int_V \frac{\rho(\mathbf{r}', t - R/c)}{R} dV \quad (3.2)$$

$$\mathbf{A}(\mathbf{r}, t) = \frac{\mu_0}{4\pi} \int_V \frac{\mathbf{J}(\mathbf{r}', t - R/c)}{R} dV \quad (3.3)$$

The potentials are related by (Griffiths 1989):

$$\nabla \cdot \mathbf{A} + \mu_0 \epsilon_0 \frac{\partial \phi}{\partial t} = 0 \quad (3.4)$$

The position vectors  $\mathbf{r}$ ,  $\mathbf{r}'$ , and  $\mathbf{R}$ , are related by:

$$\mathbf{R} = \mathbf{r} - \mathbf{r}' \quad (3.5)$$

The electric and magnetic fields expressed in terms of the scalar and vector potentials are (Griffiths 1989):

$$\mathbf{E}(\mathbf{r}, t) = -\nabla \phi - \frac{\partial \mathbf{A}}{\partial t} \quad (3.6)$$

$$\mathbf{B}(\mathbf{r}, t) = \nabla \times \mathbf{A} \quad (3.7)$$

We solve by substituting for the potentials in these expressions. The boundary condition on a conductor dictates that there be no electric field component tangent to the conductor. Thus, if we think of the ground as a perfect conductor, the electric field must have only a vertical component,  $E_z$ , and the magnetic field must have only an azimuthal component,  $B_\phi$ . The solution in this case is obtained using the "method of images", whereby the fields are computed including mirror image charges and currents of opposite sign on the opposite side of the conductor. This produces an electric field with only a component normal to the surface.

Using the method of images to compute the potentials and substituting into equations 3.6 and 3.7, we obtain the following solutions for the vertical electric field and the

azimuthal magnetic flux density (based on Uman 1987 and Uman et al. 1975):

$$E_z(r, t) = \frac{1}{2\pi\epsilon_0} \left[ \int_{h_b}^h \frac{2h^2 - r^2}{R^5} \int_0^\tau i(h, \tau - R/c) d\tau dh \right. \\ \left. + \int_{h_b}^h \frac{2h^2 - r^2}{cR^4} i(h, t - R/c) dh \right. \\ \left. - \int_{h_b}^h \frac{r^2}{c^2 R^3} \frac{\dot{a}(h, t - R/c)}{\dot{a}} dh \right] \quad (3.8)$$

$$B_\phi(r, t) = \frac{\mu_0}{2\pi} \left[ \int_{h_b}^h \frac{r}{R^3} i(h, t - R/c) dh \right. \\ \left. + \int_{h_b}^h \frac{r}{cR^2} \frac{\dot{a}(h, t - R/c)}{\dot{a}} dh \right] \quad (3.9)$$

If we assume that  $r$  is large compared to  $h$  (i.e., we are a long distance from the channel), we can neglect  $h$  and make the following approximation:

$$E_z(r, t) \approx \frac{1}{2\pi\epsilon_0} \left[ \int_{h_b}^h \frac{1}{r^3} \int_0^\tau i(h, \tau - r/c) d\tau dh \right. \\ \left. + \int_{h_b}^h \frac{1}{cr^2} i(h, t - r/c) dh \right. \\ \left. - \int_{h_b}^h \frac{1}{c^2 r} \frac{\dot{a}(h, t - r/c)}{\dot{a}} dh \right] \quad (3.10)$$

$$B_\phi(r, t) \approx \frac{\mu_0}{2\pi} \left[ \int_{h_b}^h \frac{1}{r^2} i(h, t - r/c) dh \right. \\ \left. + \int_{h_b}^h \frac{1}{cr} \frac{\dot{a}(h, t - r/c)}{\dot{a}} dh \right] \quad (3.11)$$

The three electric field terms are: the electrostatic term, proportional to  $r^{-3}$ , produced by the time integral of current; the induction term, proportional to  $r^{-2}$ , produced by the channel current; and the radiation term, proportional to

$r^{-1}$ , produced by the time derivative of the current. The two magnetic field terms are the induction and radiation terms, analogous to their electric field counterparts (Uman 1987).

Near the radiation source all three electric field terms and both magnetic field terms contribute significantly to the total radiation, complicating the solution considerably. But since  $r^{-3}$  and  $r^{-2}$  approach 0 much more rapidly than  $r^{-1}$ , we can neglect the electrostatic, induction, and magnetostatic terms at large distances, leaving only the radiation terms (Equations 3.12 and 3.13). We can make this so-called radiation field, or far field, approximation without much loss of accuracy when  $r$  is many times the height of the channel (Uman et al. 1975; Uman 1987; Griffiths 1989).

$$E_z(r,t) \approx -\frac{1}{2\pi\epsilon_0 c^2} \int_{h_b}^h \frac{1}{r} \frac{\partial \tilde{a}(h,t-r/c)}{\partial t} dh \quad (3.12)$$

$$B_\phi(r,t) \approx \frac{\mu_0}{2\pi c} \int_{h_b}^h \frac{1}{r} \frac{\partial \tilde{a}(h,t-r/c)}{\partial t} dh \quad (3.13)$$

If we make the further assumptions that the return stroke's velocity up the channel,  $v$ , and current waveform are both constant in time (as in the transmission line model discussed in Chapter V) we can eliminate the integral and the current derivative as follows:

$$\begin{aligned}\frac{di}{dt} &= \frac{\partial i}{\partial t} + v \frac{\partial i}{\partial h} = 0 \\ \frac{\partial i}{\partial t} &= -v \frac{\partial i}{\partial h} \\ \int_{h_b}^{h_t} \frac{\partial i}{\partial t} dh &= -v \int_{h_b}^{h_t} \frac{\partial i}{\partial h} dh = -v \int_{h_b}^{h_t} di = -v(i(h_t) - i(h_b))\end{aligned}$$

The solutions then take the form:

$$E_z(r, t) \approx \frac{\mu_0 v}{2\pi r} [i(h_t, t-r/c) - i(h_b, t-r/c)] \quad (3.14)$$

$$B_\phi(r, t) \approx -\frac{\mu_0 v}{2\pi cr} [i(h_t, t-r/c) - i(h_b, t-r/c)] \quad (3.15)$$

Thus, the radiation field strength is proportional to the return stroke velocity,  $v$ , and inversely proportional to the distance,  $r$ , from the channel. The  $t-r/c$  appearing in the current expression is the *retarded time* and accounts for the time required for the radiation to travel from the channel to the observer.

The temporal waveform of the fields is initially identical to the waveform at the channel base,  $h_b$ . As the return stroke wavefront reaches the top of the channel, the field waveform becomes a "mirror image" of the current at the channel top,  $h_t$ . These "turn-on" and "turn-off" fields have been documented in the literature (Uman et al. 1975 and LeVine and Meneghini 1978) but generally are not observed in nature, since we do not expect an actual return stroke channel to behave as a straight vertical segment.

LeVine and Meneghini (1978) point out, however, that the turn-on and turn-off effects are the source of the noisiness of actual return stroke radiation. They suggest that the channel can be represented by a series of randomly oriented segments connected at their endpoints. The channel then radiates from each junction point between segments where the return stroke current turns on and off. The intensity of the radiation detected from each junction point depends on the adjoining segments' orientation relative to each other and to the observer (LeVine and Meneghini 1978).

*b. Documented return stroke electric and magnetic fields*

Return stroke radiation has been analyzed extensively in the literature using a variety of sensors with a range of capabilities (Uman et al. 1970; Weidman and Krider 1978; Lin et al. 1979; Krider et al. 1980; Willet et al. 1989; Cooray and Pérez 1994). Typical characteristics of documented return stroke fields are summarized here. Examples of measured return stroke radiation are depicted in Fig. 3.1.

Signal amplitudes are typically normalized to a range of 100 km in the literature; the NLDN uses this convention as well. This is accomplished (assuming the  $r^{-1}$  signal strength range dependence) by multiplying the measured signal strength by a factor of  $(r/100 \text{ km})$  (Orville 1991; Idone et al. 1993; Hiscox and Cummins 1993). Typical normalized return stroke peak electric fields are 6 to 8 V

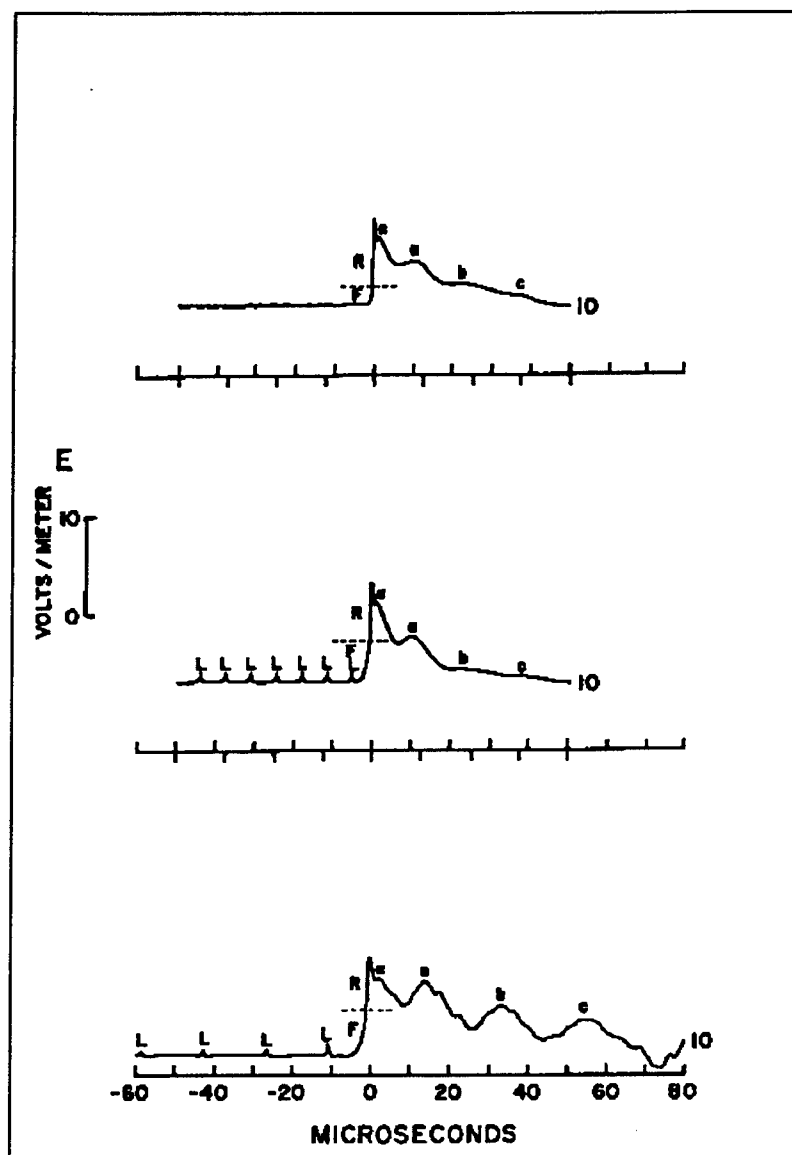


Fig. 3.1. Typical first (bottom) and subsequent return stroke waveforms with dart-stepped leaders (middle) and dart leaders (top) (adapted from Uman 1987).

$\text{m}^{-1}$  for first return strokes and 4 to 6  $\text{V m}^{-1}$  for subsequent return strokes (Uman 1987).

Return stroke fields typically rise to peak strength in two stages: an initial "slow front" lasting a few  $\mu\text{s}$  (Uman 1987; Weidman and Krider 1978); and a "fast transition" in which the signal rises from about 10% to 90% of peak signal strength in approximately .1  $\mu\text{s}$  (Uman 1987). Subsequent strokes have faster slow front risetimes (.5-1  $\mu\text{s}$ ) and do not reach peaks as high as first strokes (Weidman and Krider 1978).

Pulsewidth after the initial peak is typically tens of  $\mu\text{s}$  (Uman 1987). After the peak, signal strength drops off more slowly and the waveform may have a "shoulder" of a few  $\mu\text{s}$  width. First return strokes have multiple subsidiary peaks at 10 to 30  $\mu\text{s}$  intervals corresponding to current flowing in the channel branches (Weidman and Krider 1978).

As discussed in Chapter II, the wide range of timescales in lightning flash processes causes radiation over a wide frequency range. Higher frequencies are attenuated preferentially in propagation over a surface with finite conductivity, which creates uncertainty in the actual upper frequency limit of return stroke radiation. However, documented return stroke radiation has been measured well into the hundreds of MHz (Uman 1987).

## 2. Peak Current Calibration

Since the radiation approximation discussed above results in field strengths that are proportional to the channel current, we can solve the reverse problem--determining channel current from measured fields--by rearranging the expression:

$$i_{peak} \approx \frac{2\pi c}{\mu_0 v} r B_{peak} \approx \frac{2\pi}{\mu_0 v} r E_{peak} \quad (3.16)$$

This linear relation between peak field strength and peak current is the basis for estimating return stroke peak current from remote field measurements (Rachidi and Thottappillil 1992; Rakov et al. 1992). Note that this requires knowledge of the return stroke velocity,  $v$ , which we have assumed to be constant. Since there is no way of determining  $v$  for each detected stroke we cannot obtain a theoretical conversion constant from field strength to peak current; a calibration must be accomplished to determine it empirically.

### a. Orville calibration

Orville (1991) was the first to publish such a calibration for a network of magnetic DFs. He accomplished it using 18 return strokes triggered by a French research group at the Kennedy Space Center during 1985-88. The current of the triggered return strokes was measured directly at the channel base and their radiation was

detected by 6 DFs from the SUNYA network in Florida and Georgia with known distances from the triggering site.

He computed the average range-normalized signal strength (*RNSS*) from each DF that detected a triggered return stroke, then derived the following linear best-fit relation between the average *RNSS* and the measured peak current:

$$I = 2.3 \text{ kA} + (.19 \text{ kA LLP}^1) \text{RNSS} \quad (3.17)$$

The standard deviation of the data points about the best-fit line is approximately 6 kA (Fig. 3.1).

This work validated the approximate rule of thumb used to date with LLP DFs: dividing *RNSS* by 5 to obtain peak current (Hiscox and Cummins 1993). This rule of thumb produces results within approximately 6% of Orville's calibration.

As a further step, Orville calibrated for each DF individually and determined that measured signal strength fell off as  $r^{-1.13}$ , due to attenuation.

*b. Idone et al. calibration*

In 1993, Idone et al. published a reexamination of Orville's calibration, using an expanded data set of 57 triggered return strokes from 36 different flashes. Their best-fit relation, using the same technique as Orville, is:

$$I = 4.20 \text{ kA} + (.171 \text{ kA LLP}^1) \text{RNSS} \quad (3.18)$$

with a comparable standard deviation.

If Orville's  $r^{-1.13}$  power law relationship is used to compute the normalized signal strength ( $RNSS=(r/100 \text{ km})^{-1.13}$ ), the best-fit relation becomes:

$$I = 5.20 \text{ kA} + (.145 \text{ kA LLP}^1)RNSS \quad (3.19)$$

This is the calibration adopted by Global Atmosphericics for use with the NLDN (Hiscox and Cummins 1993). Idone et al. estimate a peak current uncertainty of 10-15% in flashes with peak currents between 15 and 60 kA (Fig. 3.2).

*c. Forcing calibration best-fit intercept to 0 kA*

The non-zero intercepts in the Orville and Idone et al. calibrations are troubling and have yet to be explained. Based on Eq. 3.16, we expect the best-fit line relating peak current and RNSS to pass through the origin.

As a result of the increased number of weak flashes detected by the NLDN since the upgrade (discussed in Chapter IV), Global Atmosphericics has been forced to deal with this issue. It has introduced a new peak current calibration with a 0 kA intercept,  $I = (.185 \text{ kA LLP}^1)RNSS$ , effective May 1996 (Cummins et al. 1996).

Best-fit relations using the same data as Orville and Idone et al. but with intercepts constrained to 0 kA results in higher slopes (resulting in larger estimated peak currents) and increased standard deviations of the data

about the lines (since the relation is no longer a best-fit to the data). The slope of the Orville calibration increases from .178 to .195 kA LLP<sup>-1</sup> and the standard deviation increases from 6.304 to 6.427 kA; the Idone et al. calibration slope increases from .171 to .203 kA LLP<sup>-1</sup> and the standard deviation increases from 4.649 to 4.984 kA.

Appendix A contains a verification of the Orville and Idone et al. calibrations using their published raw data, a correction to Orville's calibration to account for an error in one DF location, and the recalibration of both data sets with forced 0 kA intercepts.

## CHAPTER IV

### DATA ANALYSIS

The purpose of this chapter is to describe quantitatively the change in mean peak current, flash count, and percent positive flashes observed since the NLDN upgrade.

#### 1. Previous work

In a study of thunderstorm prediction in the Whiteman Air Force Base, Missouri vicinity Bass (1996) documented several changes in NLDN archived data: 1) the percent of flashes in 1994 and 1995 having positive polarity doubled compared to 1989-93, 2) the 1995 mean peak current decreased 10-15% for negative flashes and 20% for positive flashes, and 3) in 1995 twice as many negative flashes with peak currents less than 20 kA were detected and most of the positive flash count increase was for flashes with peak currents less than 30 kA.

#### 2. Data set and analysis methods

##### a. 1989-95 NLDN archived data

The NLDN records the time, location, polarity, RNSS, and multiplicity of every CG lightning flash it detects. These data are encoded in binary form, using eleven bytes per flash and disseminated to NLDN subscribers in near real-time. This analysis uses NLDN lightning data archived from 1989 through 1995.

Flash counts and mean peak currents are analyzed on a monthly and yearly basis for both positive and negative flashes. To provide for regional comparisons and to develop the initial data analysis process, three regions within the US data set were chosen to analyze before undertaking the whole archive. Table 4.1 lists the three regions and their boundaries. Each contains approximately ten million flashes for the seven year period.

Table 4.1. Data analysis geographical subsets

Area	Latitude bounds (°N)	Longitude bounds (°W)
Kansas	36.0 - 41.0	93.25 - 103.5
Ohio Valley	36.0 - 41.0	78.0 - 88.25
Florida	27.0 - 29.5	81.25 - 82.25

After completing the analysis for each region, the full US data set of over 134 million flashes was analyzed in greater detail. Positive and negative monthly and yearly flash counts and mean peak currents were computed as in the original three regions. In addition, flash count distributions as a function of peak current were computed to determine if the increase in flash count occurred preferentially for stronger or weaker flashes.

*b. Analysis tools*

The NLDN archived data were initially analyzed with the FLASH lightning analysis software, a DOS-based package that

uses a monochrome monitor as a user interface and a color monitor to display graphical results. FLASH can be used to produce scatter plots, time series, and contours of flash counts, peak currents, multiplicity, polarity, and other parameters of detected CG flashes. It reads NLDN data in the binary format described above.

FLASH produces useful results, but can be very time consuming to use because it has no capability for running scripts, so the user must input commands and record results manually. For this reason, the author wrote FORTRAN code that reads binary NLDN data files, computes monthly, seasonal, and yearly flash counts, mean peak currents and peak current distributions, and stores the results in text files.

The text files containing flash counts, mean peak currents, and peak current distributions are then read with the MathCAD 6.0+ software package, where further statistical analysis was performed (i.e. computed weighted mean peak currents and standard deviations) and preliminary graphical results were produced. Final graphical results were produced using Axum 5.0 software. A sample of the statistical analysis is contained in Appendix B.

### 3. Results

Tables 4.2 and 4.3 summarize the flash counts and mean peak currents for each of the subset regions and for the

Table 4.2. Post- vs. pre-upgrade negative flash count and mean peak current comparison

	Kansas	Ohio	Florida	US
Flash count				
1989-93 mean flash count ( $\times 10^6$ )	1.199	1.409	1.311	16.65
1994 flash count ( $\times 10^6$ )	1.692	1.869	1.531	23.02
Z	1.16	1.03	1.23	1.87
1995 flash count ( $\times 10^6$ )	1.144	1.796	1.195	20.61
Z	-0.13	0.86	-0.65	1.16
Mean peak current				
1989-93 mean peak current (kA)	32.9	33.7	41.2	37.5
1994 mean peak current	29.8	31.8	36.2	34.26
Z	-3.36	-1.37	-0.68	1.73
1995 mean peak current	26.1	26.5	33.2	30.2
Z	-7.26	-5.07	-1.08	-3.39

Z = standard deviations above pre-upgrade mean

Table 4.3. Post- vs. pre-upgrade positive flash count and mean peak current comparison

	Kansas	Ohio	Florida	US
Flash count				
1989-93 mean flash count ( $\times 10^6$ )	0.079	0.037	0.038	0.696
1994 flash count ( $\times 10^6$ )	0.138	0.052	0.061	1.193
Z	1.86	1.02	1.85	2.19
1995 flash count ( $\times 10^6$ )	0.148	0.164	0.128	2.107
Z	2.20	8.57	7.24	6.22
Mean peak current				
1989-93 mean peak current (kA)	55.2	54.2	33.9	54.4
1994 mean peak current	44.7	48.3	26.5	45.8
Z	-8.64	-0.72	-1.11	-1.87
1995 mean peak current	37.6	23.4	19.3	31.6
Z	-14.53	-3.79	-2.21	-4.97

Z = standard deviations above pre-upgrade mean

entire US before the upgrade (1989-93), during the upgrade (1994), and after the upgrade (1995). For purposes of comparison, 1989-93 are considered pre-upgrade years and 1995 is considered the post-upgrade year. Since the network upgrade occurred during 1994, it is considered separately from the pre- and post-upgrade data sets.

a. *Kansas*

The Kansas data set consisted of slightly over 9.5 million flashes, approximately 8.8 million negative and 680 000 positive:

1) *Negative flashes*

As Table 4.2 and Fig. 4.1 show, the post-upgrade negative flash count remains close to the pre-upgrade mean of approximately 1.2 million flashes per year. 1994 and 1995 monthly flash counts are, with three exceptions, within two standard deviations of the pre-upgrade means. The 1995 negative flash count is approximately 1.14 million flashes, only .13 standard deviation below the 1989-93 Kansas mean negative flash count.

While the negative flash count remains relatively constant, the Kansas negative mean peak current decreases significantly after the upgrade, as depicted in Table 4.2 and Fig. 4.2. From a pre-upgrade value of 32.9 kA the 1994 mean peak current drops 3.36 standard deviations to 29.8 kA and the 1995 mean sinks to 26.1 kA, a decrease of 7.26

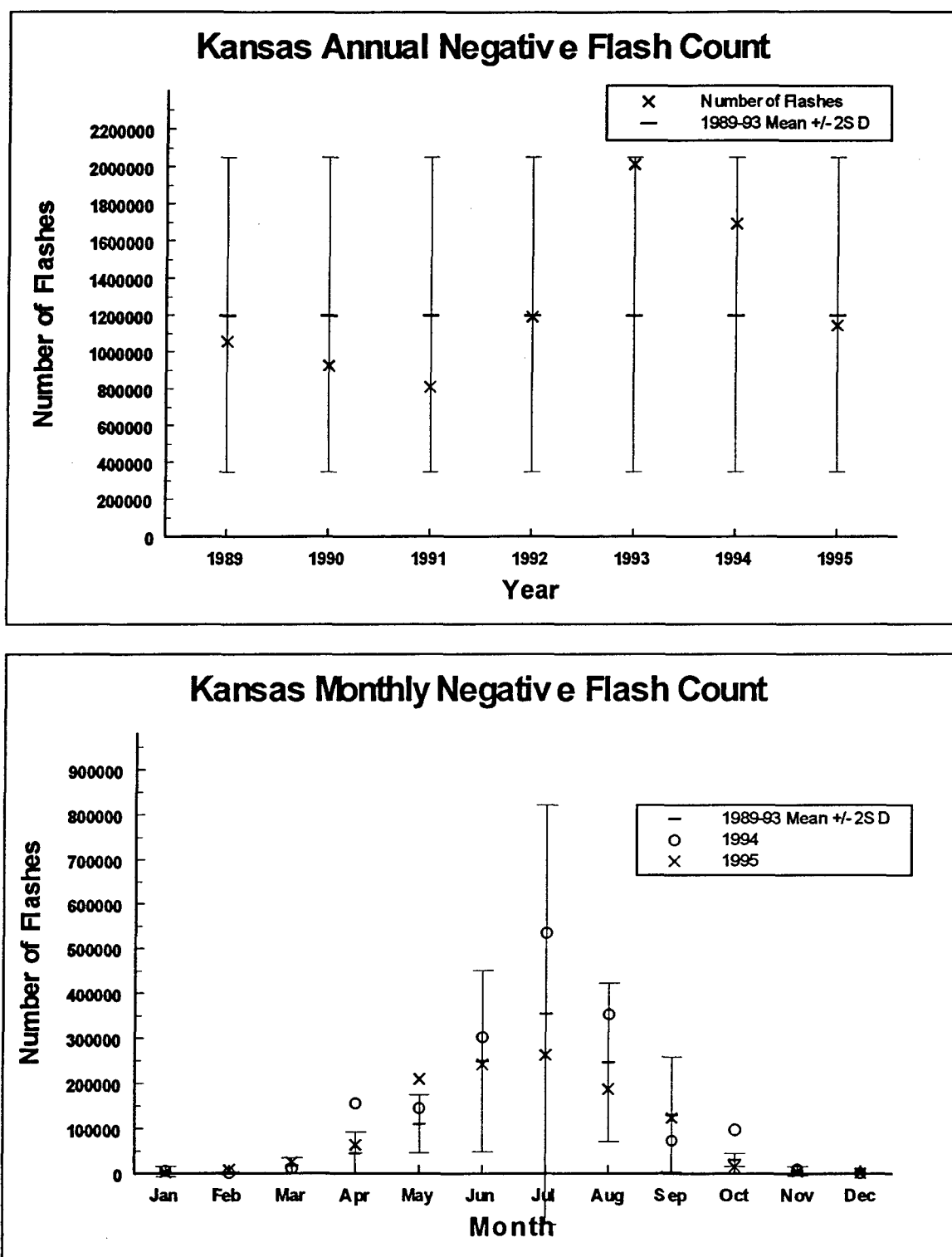


Fig. 4.1. Kansas annual (top) and monthly (bottom) negative flash count, 1989-95. Error bars are two standard deviations above and below the mean.

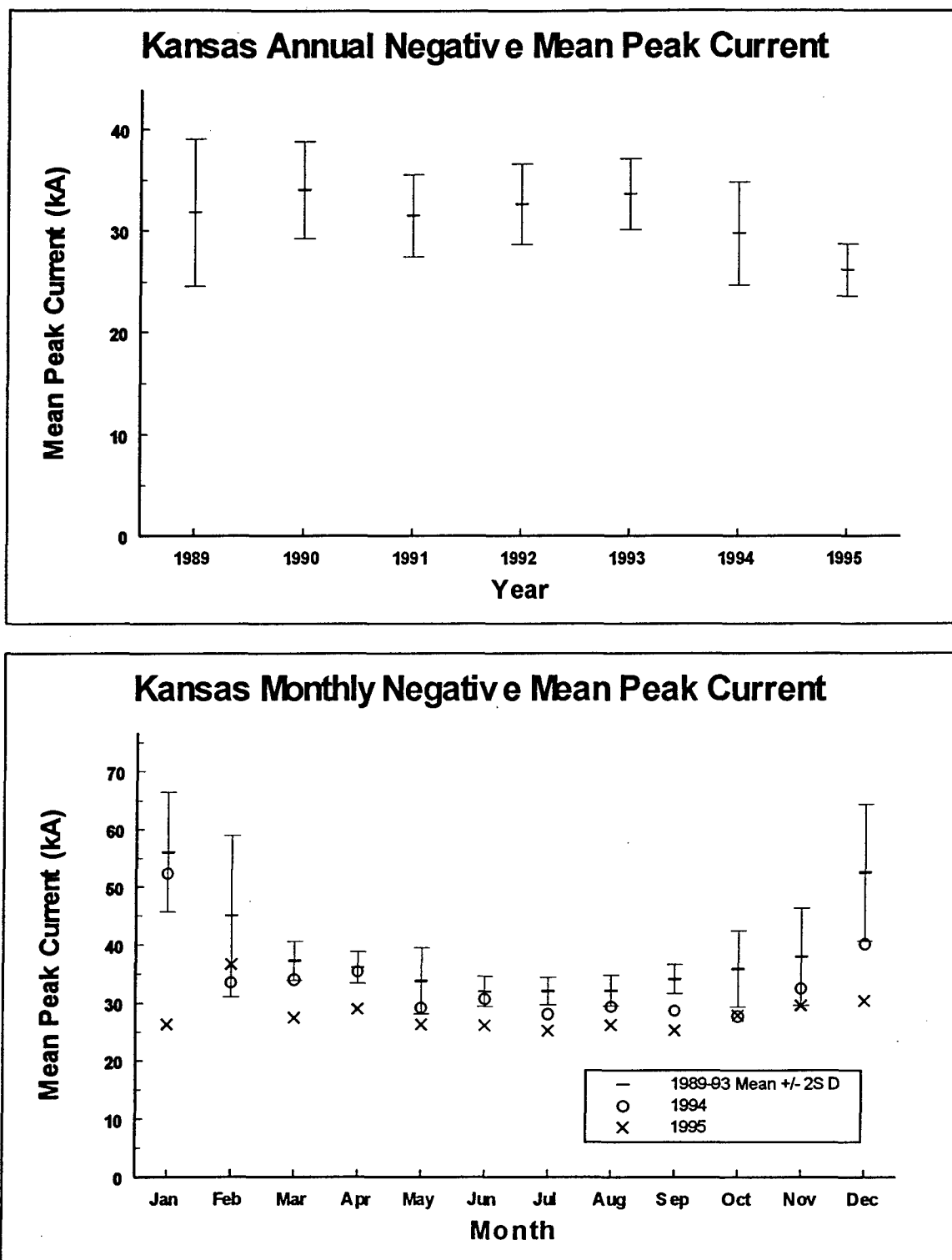


Fig. 4.2. Kansas annual (top) and monthly (bottom) mean peak current, 1989-95. Error bars are two standard deviations above and below the mean.

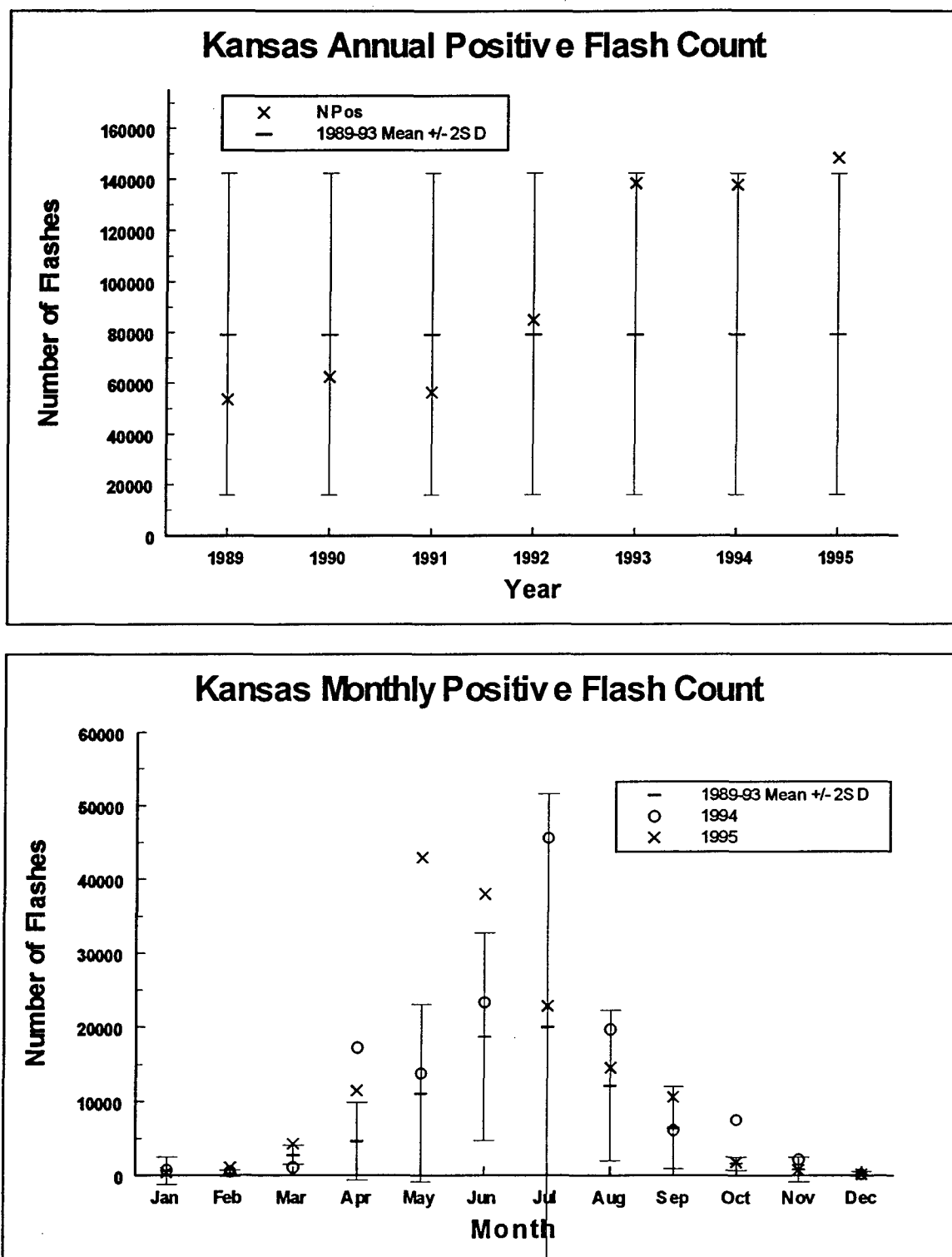


Fig. 4.3. Kansas annual (top) and monthly (bottom) positive flash count, 1989-95. Error bars are two standard deviations above and below the mean.

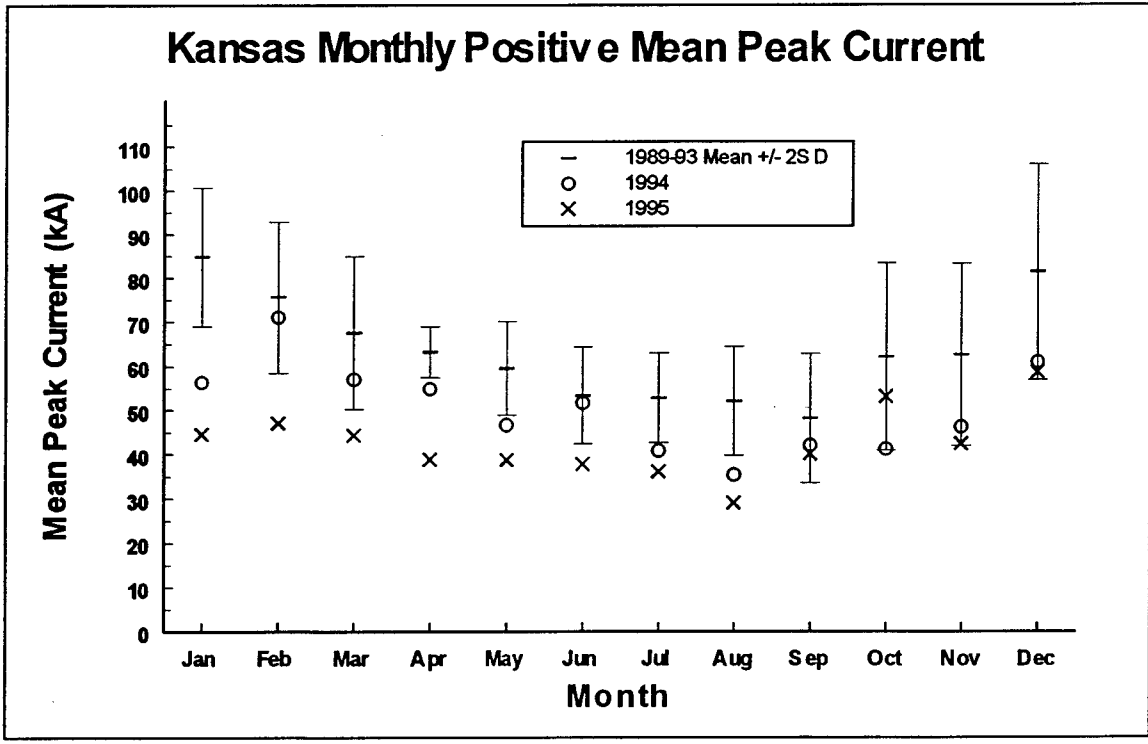
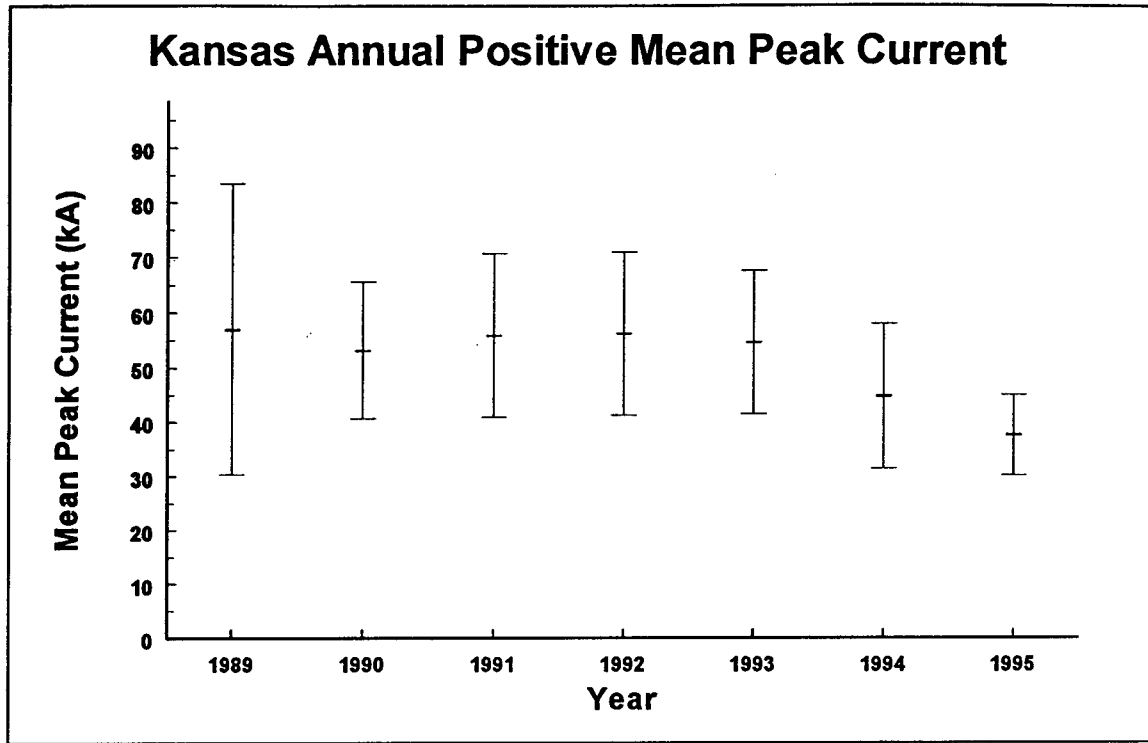


Fig. 4.4. Kansas annual (top) and monthly (bottom) positive mean peak current, 1989-95. Error bars are two standard deviations above and below the mean.

standard deviations. Mean peak currents first exceed two standard deviations below the pre-upgrade mean in July 1994; every month of 1995 has a mean peak current less than two standard deviations below the pre-upgrade monthly mean.

## 2) Positive flashes

Unlike the Kansas negative flash count, the positive flash count increases significantly after the upgrade, as depicted in Table 4.3 and Fig. 4.3. From a pre-upgrade mean of approximately 79 000 flashes per year, the 1995 total increases by 2.2 standard deviations to 148 000 flashes. The monthly flash count shows that this increase occurs primarily in the late spring and early summer of 1995.

The Kansas positive mean peak current decreases even more dramatically than the negative mean peak current, from a pre-upgrade mean of 55.2 kA to a 1994 mean of 44.7 kA, an 8.64 standard deviation decrease, and a 1995 mean of 37.6 kA, a 14.53 standard deviation decrease. Fig. 4.4 shows that this decrease begins in July 1994, as it did for negative flashes.

## b. Ohio Valley

The Ohio Valley data set consists of approximately 11.1 million flashes, 10.7 million negative and just under 400 000 positive:

1) Negative flashes

Table 4.2 and Fig. 4.5 show that the Ohio Valley negative flash count averages approximately 1.4 million flashes  $\text{yr}^{-1}$  before the upgrade. 1994 and 1995 both have approximately 1.8 million flashes, an increase of less than one standard deviation after the upgrade. As in the Kansas data set, with few exceptions the post-upgrade monthly negative flash counts are all within two standard deviations of the pre-upgrade mean flash count. The large flash count in 1993 corresponds to the Midwest flood during that summer. If 1993 were not considered, the negative flash count standard deviation would be much lower and the post-upgrade flash count increase would be statistically more significant.

Ohio Valley negative mean peak currents exhibit a very similar pre- to post-upgrade change as Kansas mean peak currents, as shown in Fig. 4.6. From a pre-upgrade mean peak current of 33.7 kA, the 1994 mean decreases to 31.8 kA, a 1.37 standard deviation increase, and the 1995 mean decreases further to 26.5 kA, a 5.07 standard deviation decrease. For the Ohio valley, the decrease in negative mean peak current appears to begin in September or October 1994.

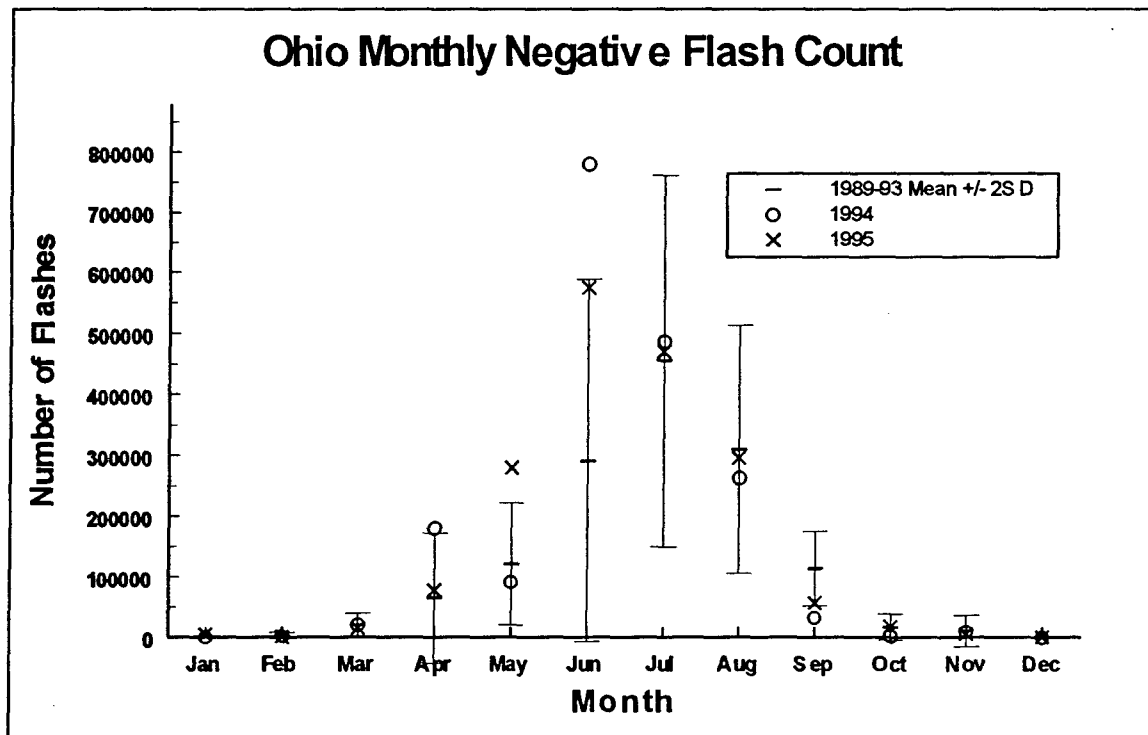
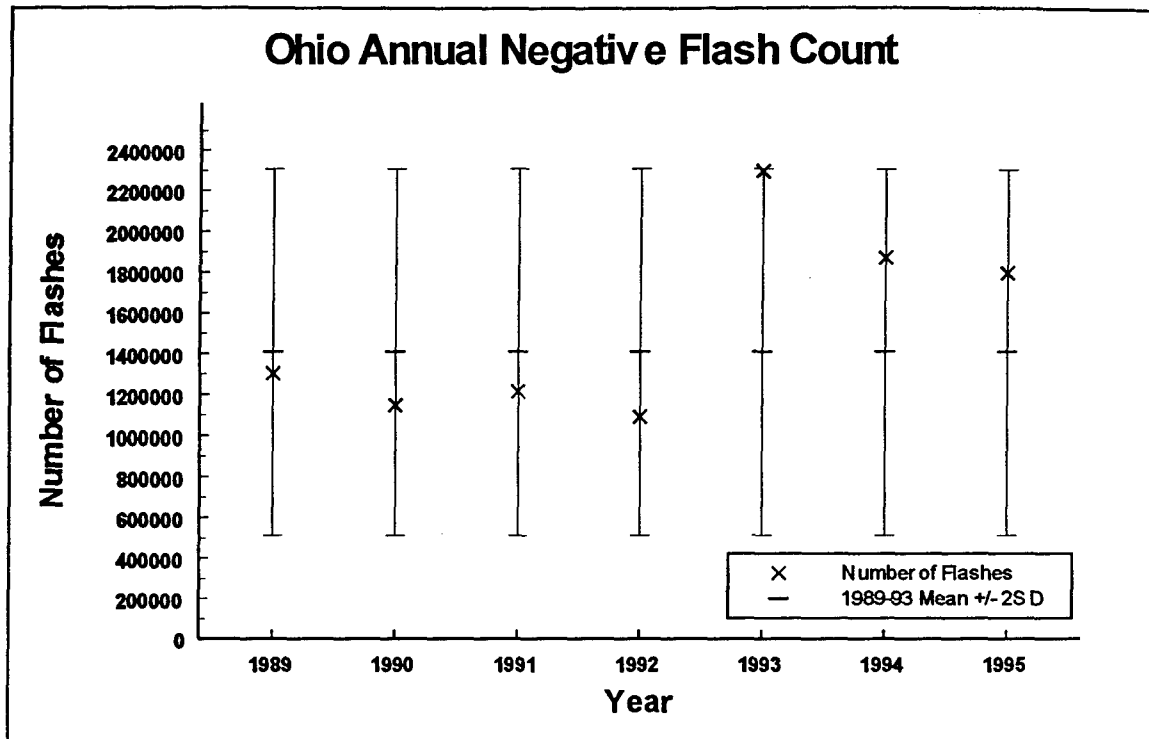


Fig. 4.5. Ohio Valley annual (top) and monthly (bottom) negative flash count, 1989-95. Error bars are two standard deviations above and below the mean.

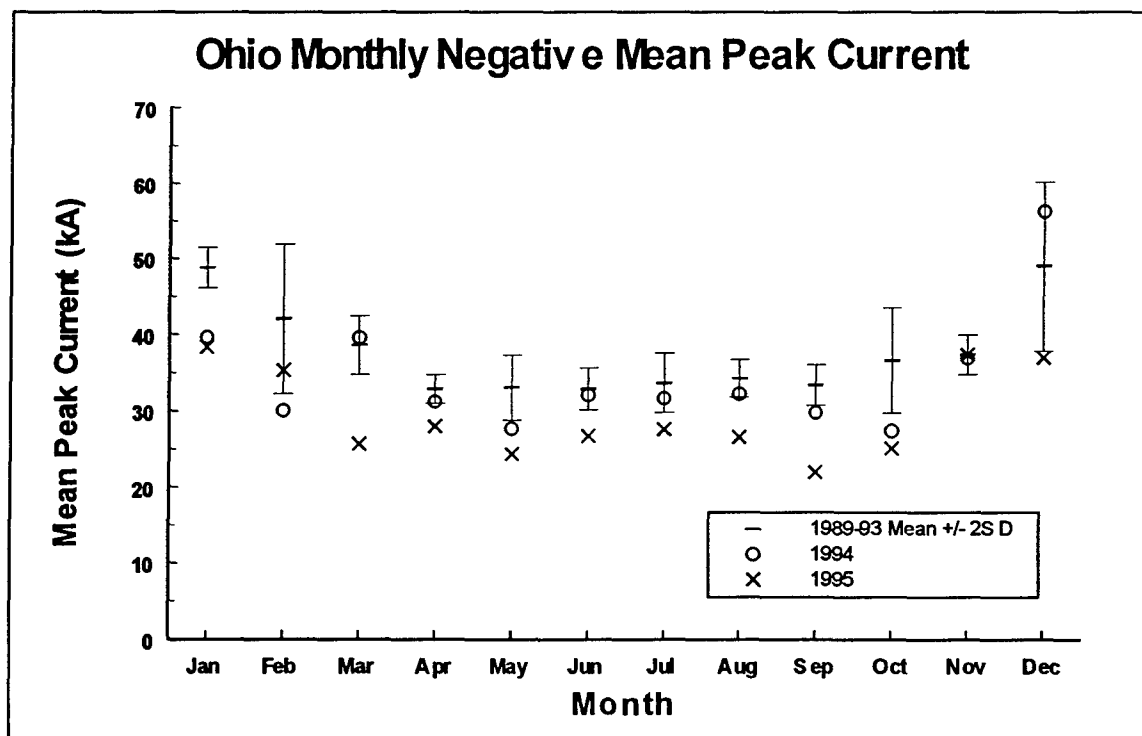
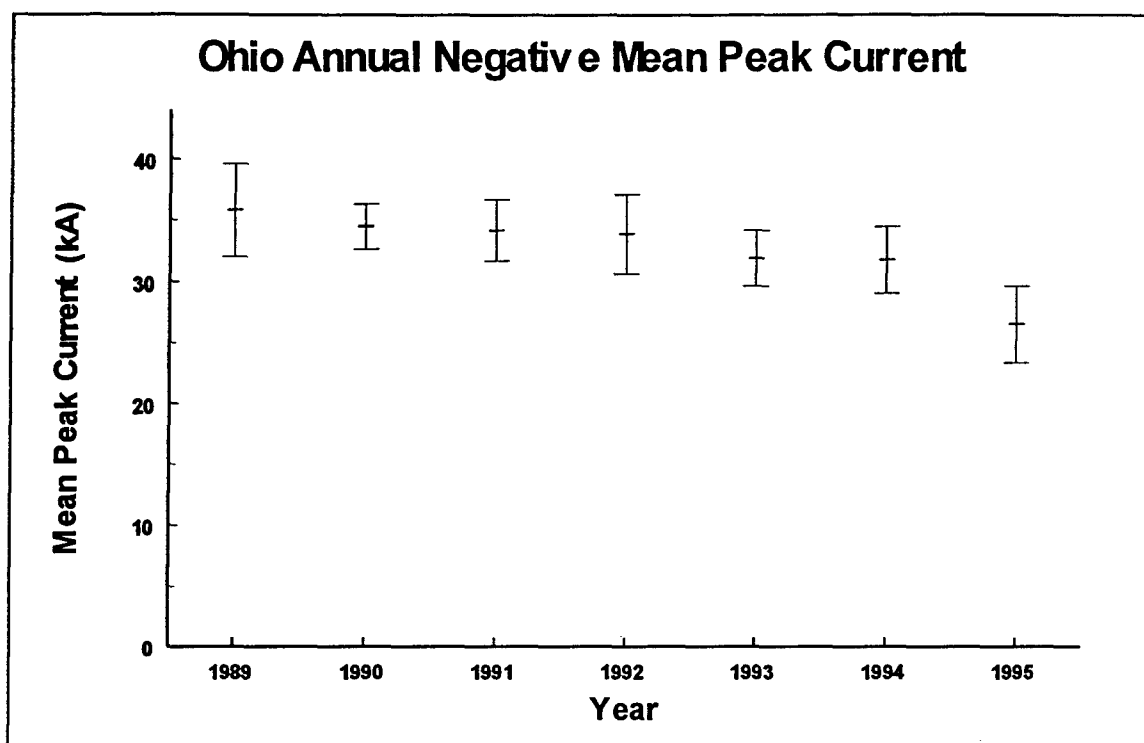


Fig. 4.6. Ohio Valley annual (top) and monthly (bottom) negative mean peak current, 1989-95. Error bars are two standard deviations above and below the mean.

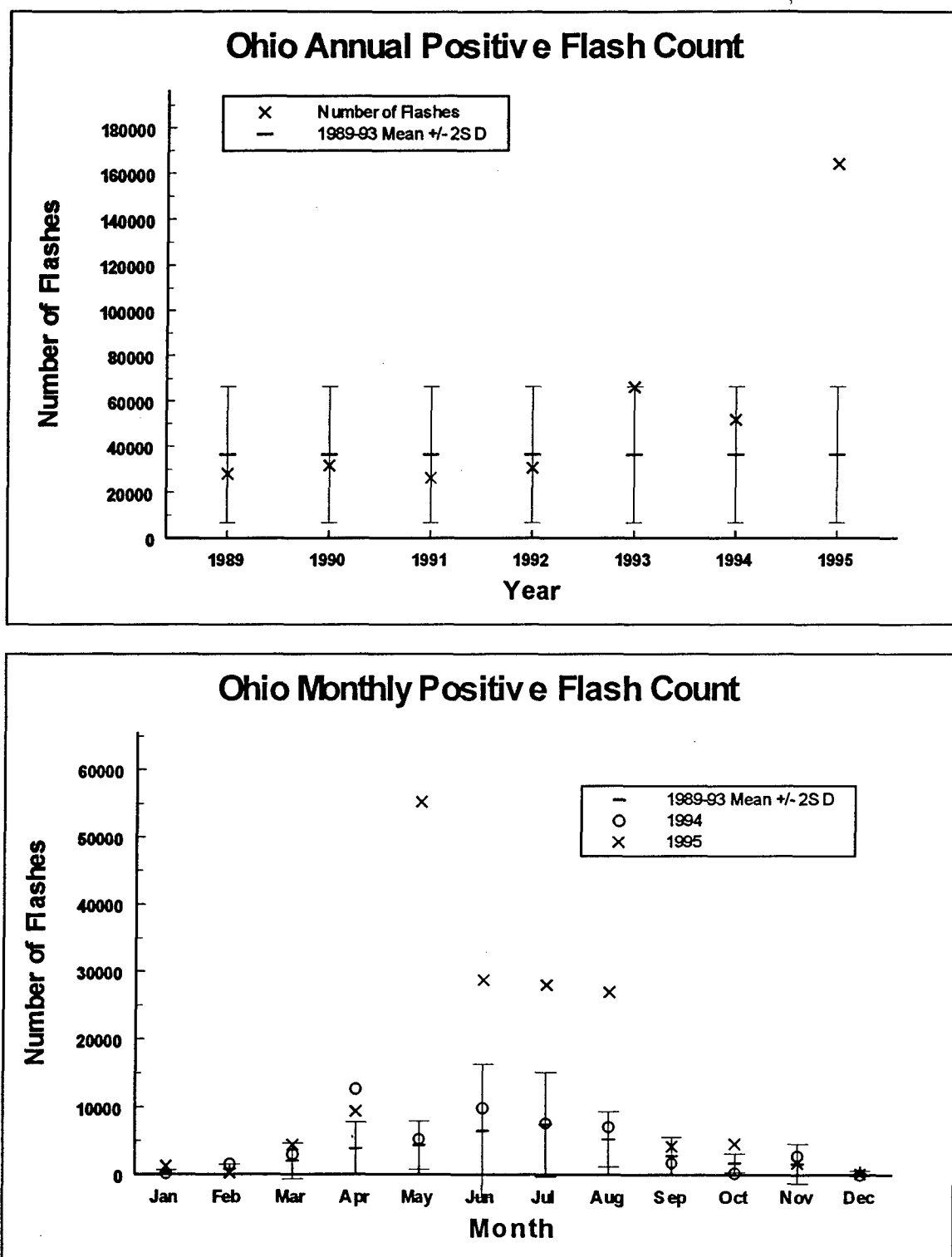


Fig. 4.7. Ohio Valley annual (top) and monthly (bottom) positive flash count, 1989-95. Error bars are two standard deviations above and below the mean.

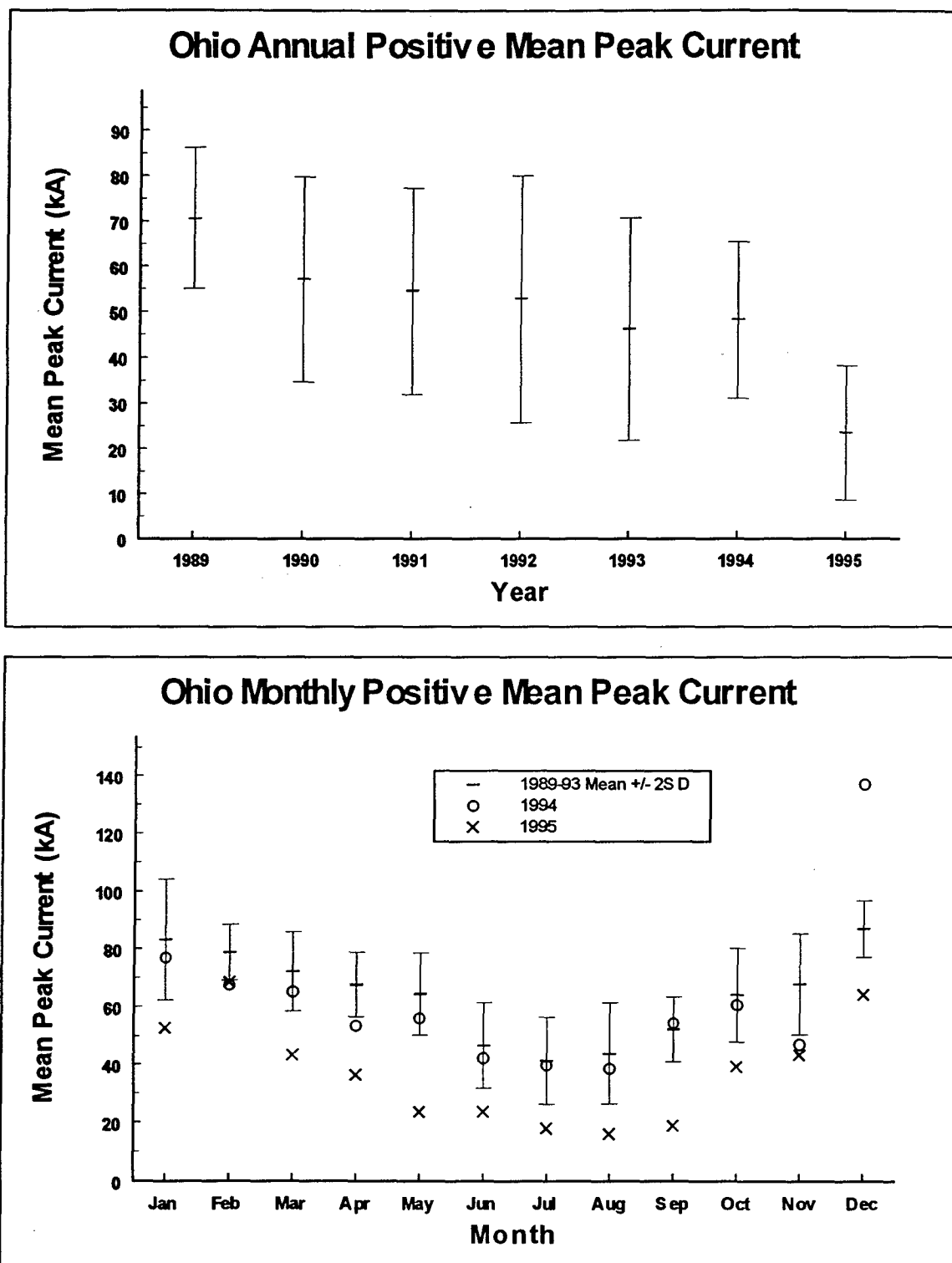


Fig. 4.8. Ohio Valley annual (top) and monthly (bottom) positive mean peak current, 1989-95. Error bars are two standard deviations above and below the mean.

## 2) Positive flashes

As shown in Table 4.3 and Fig 4.7, the Ohio Valley post-upgrade positive flash count increases much more dramatically than the Kansas positive flash count--from a pre-upgrade mean of approximately 37 000 flashes  $\text{yr}^{-1}$  to a 1994 count of 52 000, about a one standard deviation increase, and a 1995 count of 164 000, an 8.57 standard deviation increase. As with Kansas, this appears to be primarily a warm-season effect, with the 1995 increase occurring mainly during the months April through August.

While the Ohio Valley positive mean peak current decrease is more modest than Kansas' in terms of standard deviations below the pre-upgrade mean, the actual numerical change is larger. This is due to the large variance in the Ohio Valley data caused by the abnormally high positive mean peak current of 70.6 kA in 1989. The pre-upgrade mean peak current is 54.2 kA; in 1994 the mean drops less than one standard deviation (but 6 kA) to 48.3 kA and in 1995 it decreases further to 23.4 kA, only 3.79 standard deviations, but over 50% less than the pre-upgrade value. Fig. 4.8 shows the decrease to have begun in about November 1994.

### c. Florida

The Florida data set consists of approximately 9.7 million flashes, 9.3 million negative and just under 380 000 positive:

1) Negative flashes

As depicted in Table 4.2 and Fig. 4.9, Florida negative flash counts average just over 1.3 million flashes  $\text{yr}^{-1}$  before the upgrade. In 1994 the count increases 1.23 standard deviations to over 1.5 million, but in 1995 it decreases to just under 1.2 million. Every 1994 and 1995 monthly negative flash count except one is within two standard deviations of the pre-upgrade monthly negative mean flash count.

As is the case with positive flashes in the Ohio Valley, one abnormally high annual peak current (1990) causes a large variance in the pre-upgrade Florida negative mean peak current, so a relatively large post-upgrade change produces less meaningful statistical results. The pre-upgrade negative mean peak current is 41.2 kA, approximately 8 kA higher than the Kansas and Ohio Valley negative mean peak currents. In 1994 this decreases to 36.2 kA, a 12% decrease, but only .68 standard deviations; in 1995 the mean peak current sinks to 33.2 kA, a 19% decrease from the pre-upgrade mean, but only 1.08 standard deviations. As Fig. 4.10 shows, monthly mean peak currents after April 1994 are below the pre-upgrade mean, but relatively few exceed two standard deviations below the mean.

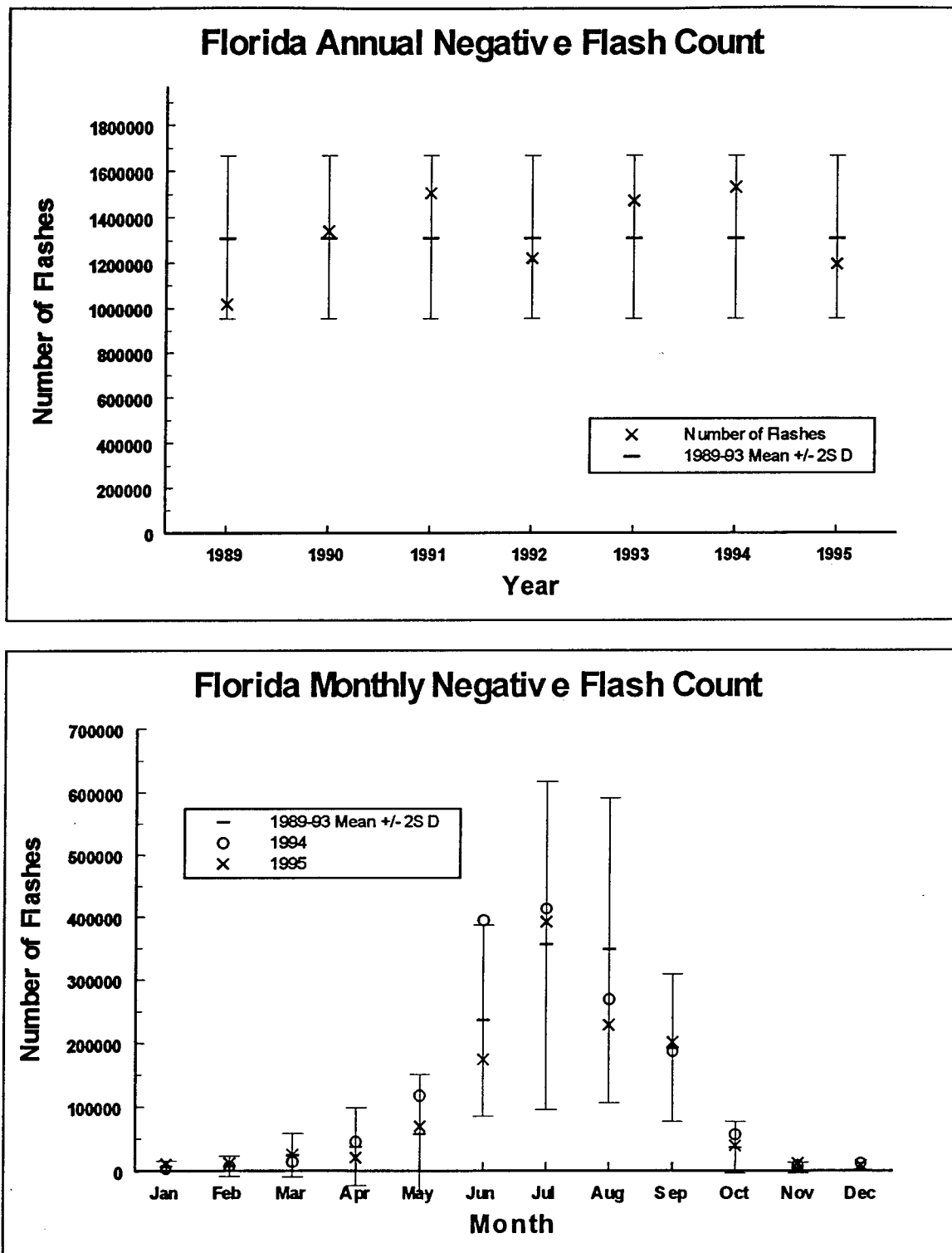


Fig. 4.9. Florida annual (top) and monthly (bottom) negative flash count, 1989-95. Error bars are two standard deviations above and below the mean.

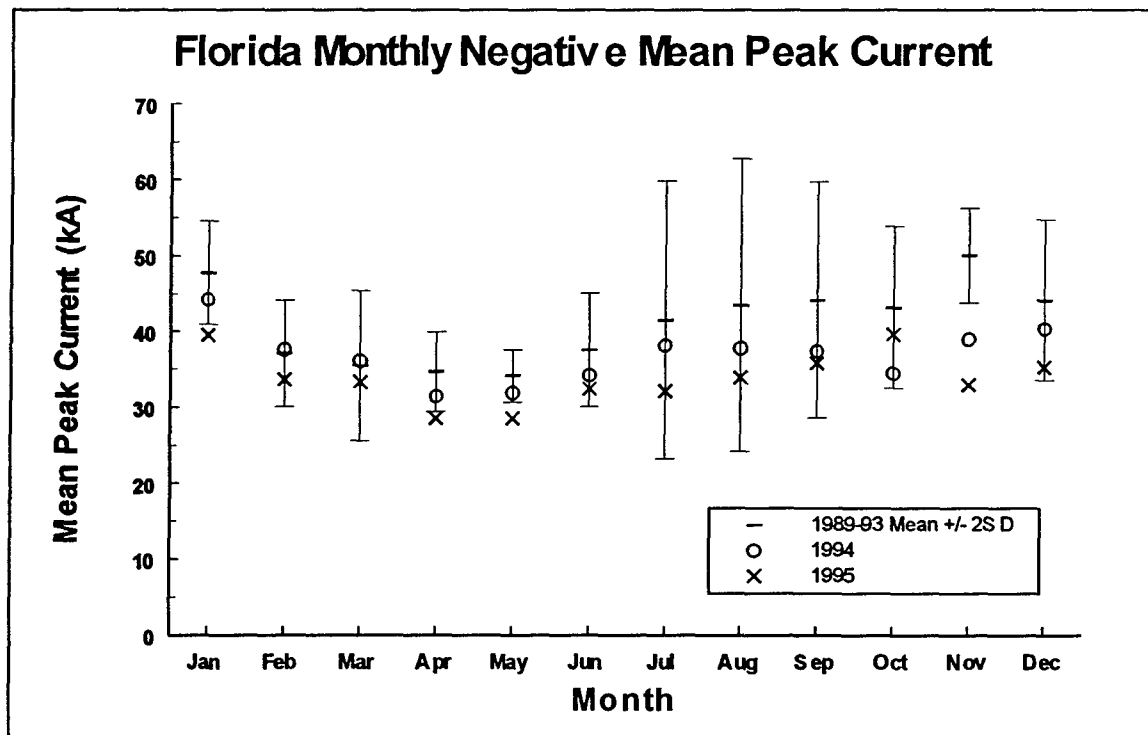
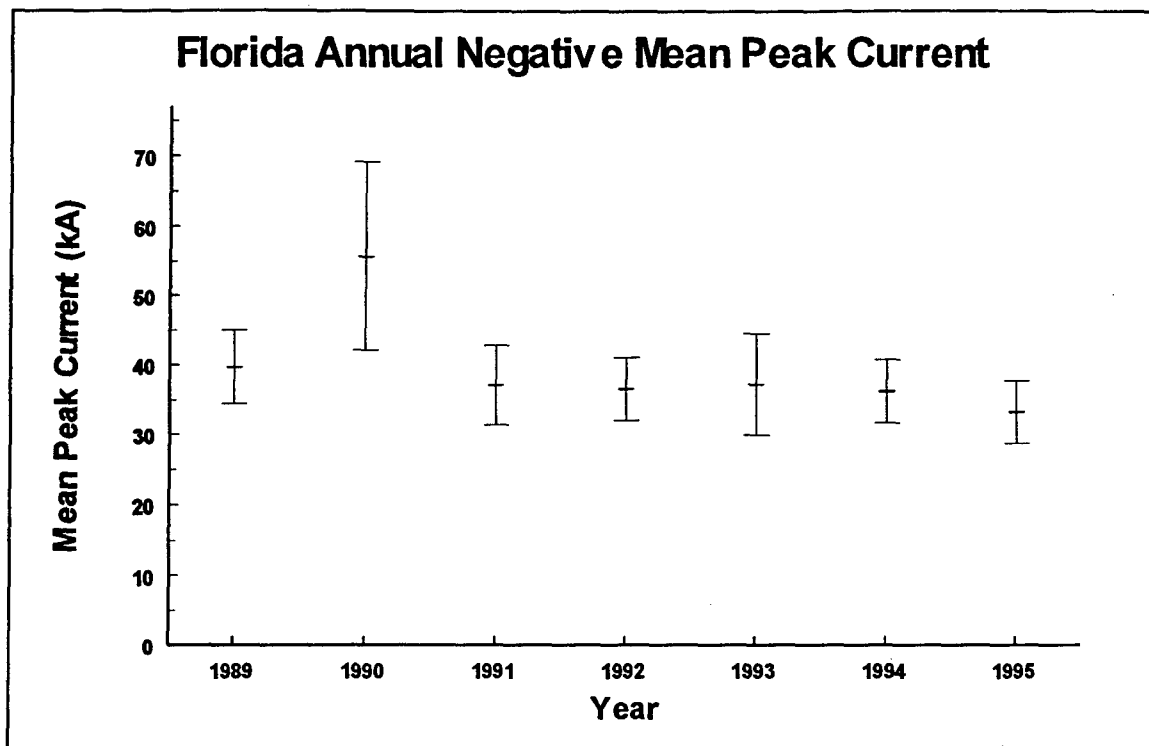


Fig. 4.10. Florida annual (top) and monthly (bottom) negative mean peak current, 1989-95. Error bars are two standard deviations above and below the mean.

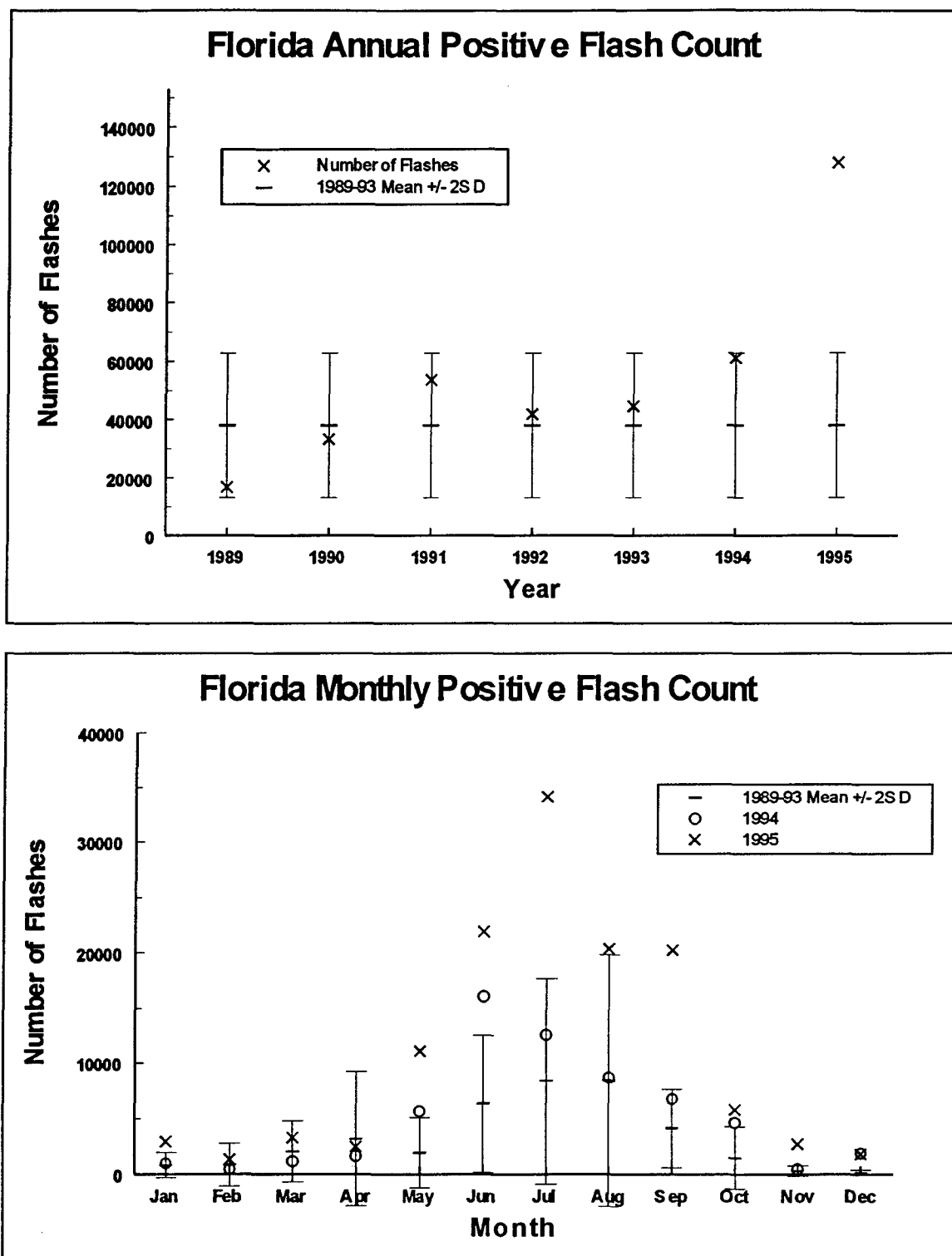


Fig. 4.11. Florida annual (top) and monthly (bottom) positive flash count, 1989-95. Error bars are two standard deviations above and below the mean.

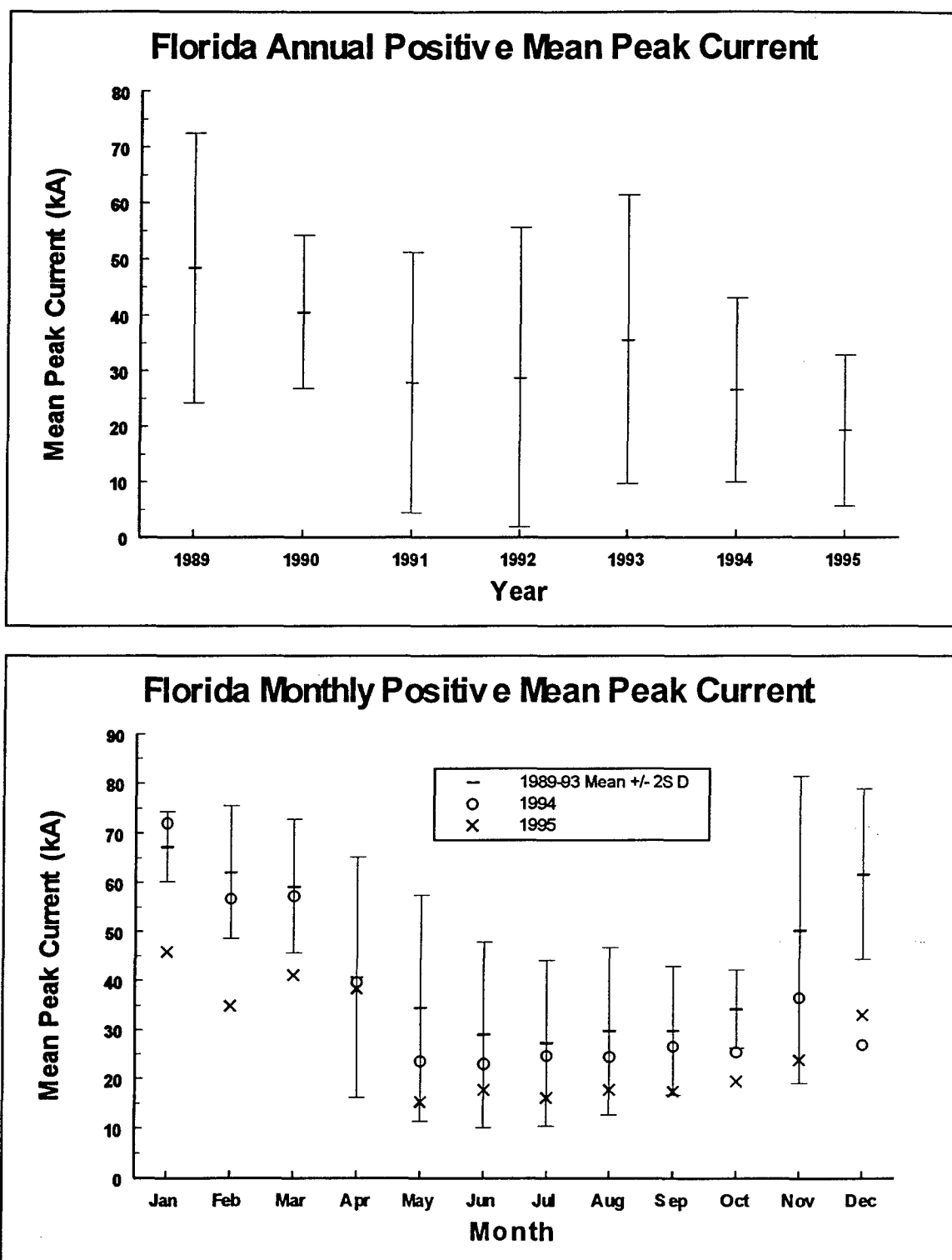


Fig. 4.12. Florida annual (top) and monthly (bottom) positive mean peak current, 1989-95. Error bars are two standard deviations above and below the mean.

## 2) Positive flashes

As in the Kansas and Ohio Valley data, the Florida positive flash count increases more dramatically after the upgrade than the negative flash count. There are an average of just over 38 000 flashes  $\text{yr}^{-1}$  before the upgrade. In 1994, the count increases by 1.85 standard deviations to 61 000 flashes; in 1995 it increases to 128 000 flashes--a 7.24 standard deviation increase. Fig. 4.11 shows that, as with Ohio positive flashes, the increase is most dramatic during the warm season, from May to September 1995.

The large variance that affected Florida negative mean peak currents also affects Florida positive mean peak currents, causing large numerical changes to have relatively little statistical significance. The pre-upgrade positive mean peak current is 33.9 kA, about 20 kA lower than the Kansas and Ohio Valley means. In 1994 the mean drops to 26.5 kA, a 1.11 standard deviation decrease, and in 1995 it sinks to 19.3 kA, a 2.21 standard deviation decrease (although the value is 43% lower). The decrease is evident in Fig. 4.12 after September 1994.

### *d. Continental United States*

The full US NLDN archived data set contains roughly 133.7 million flashes, 126.9 million of which are negative and 6.8 million of which are positive. Many of the same pre- and post-upgrade flash characteristics are exhibited by

the full data set as in the smaller regions. Due to its much larger sample size, though, it tends to have less "noisiness" than the smaller samples in the subsets, resulting in smaller standard deviations for flash counts and mean peak currents.

1) Negative flashes

As Table 4.2 and Fig. 4.13 show, the pre-upgrade US negative mean flash count is 16.65 million flashes  $\text{yr}^{-1}$ . The 1994 flash count is 1.87 standard deviations higher at 23.02 million flashes, while the 1995 flash count is only 1.16 standard deviations higher at 20.61 million flashes. As with the Kansas and Ohio Valley data sets, only a handful of post-upgrade monthly negative flash counts exceeds two standard deviations above the pre-upgrade mean negative flash count.

Table 4.2 and Fig. 4.14 depict US negative mean peak currents. The pre-upgrade mean is 37.5 kA, roughly 4 kA higher than the Kansas and Ohio Valley pre-upgrade means and 4 kA below the Florida pre-upgrade mean. In 1994 the mean decreases 1.73 standard deviations to 34.3 kA and in 1995 it decreased to 30.2 kA, 3.39 standard deviations below the pre-upgrade mean. The monthly negative mean peak current first exceeds two standard deviations below the pre-upgrade mean after September 1994 and remains well below that value for all of 1995.

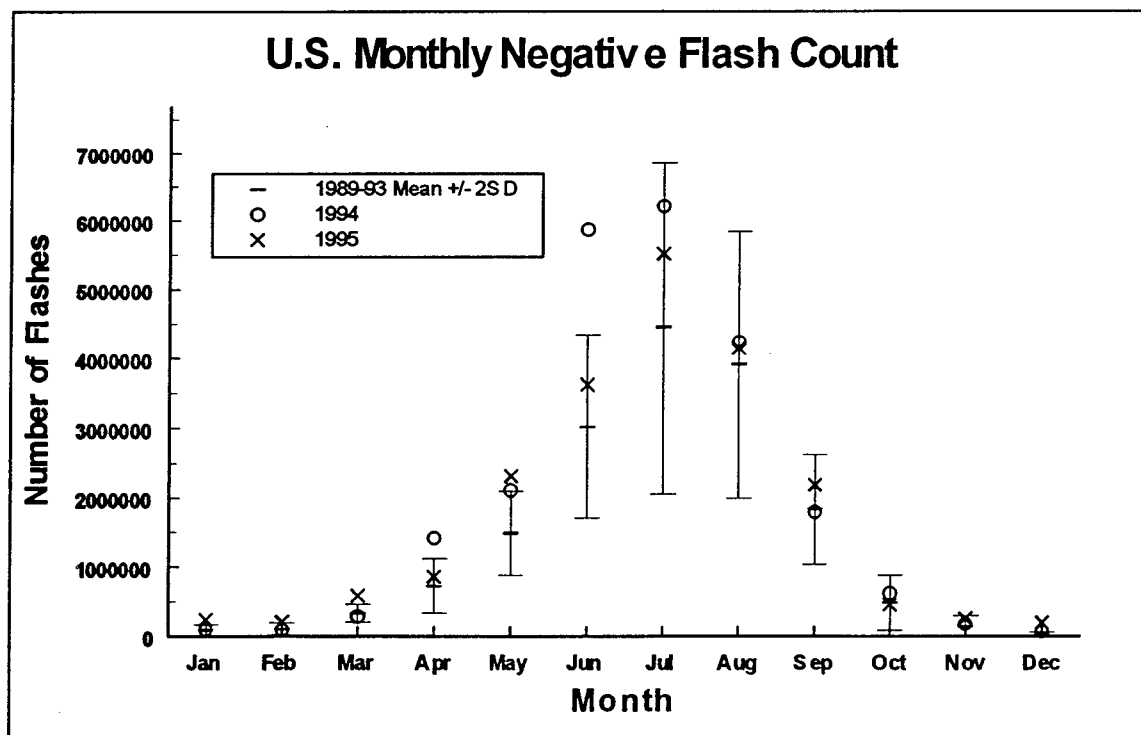
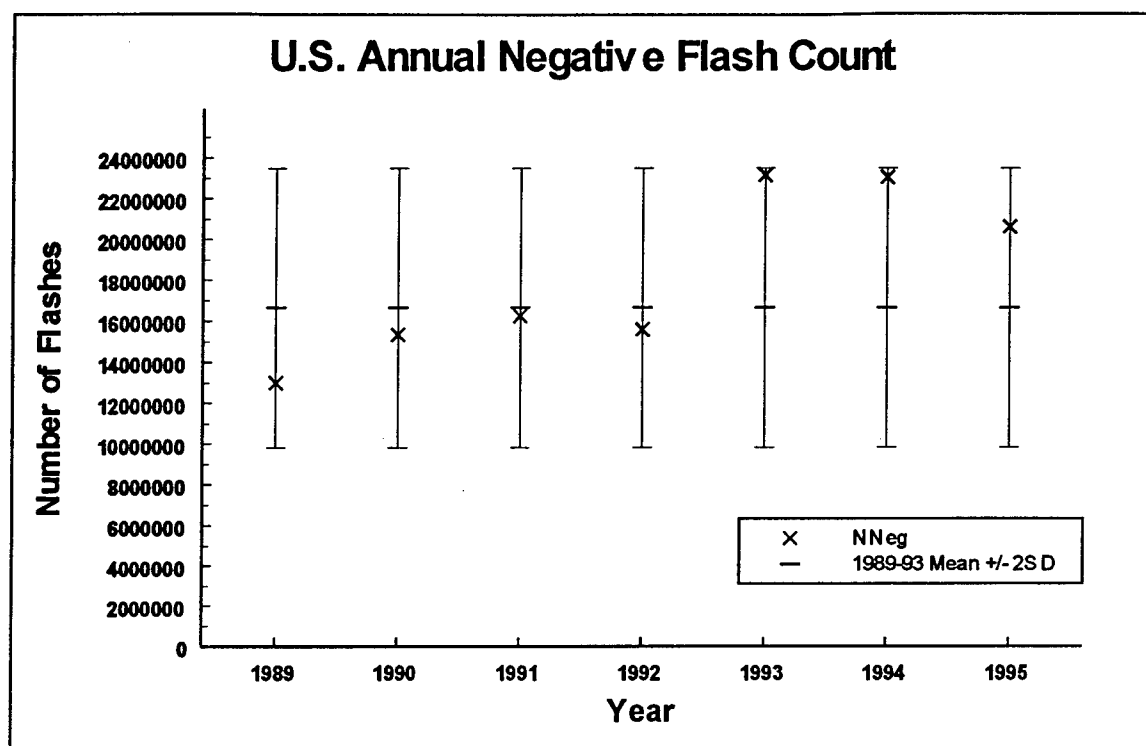


Fig. 4.13. US annual (top) and monthly (bottom) negative flash count, 1989-95. Error bars are two standard deviations above and below the mean.

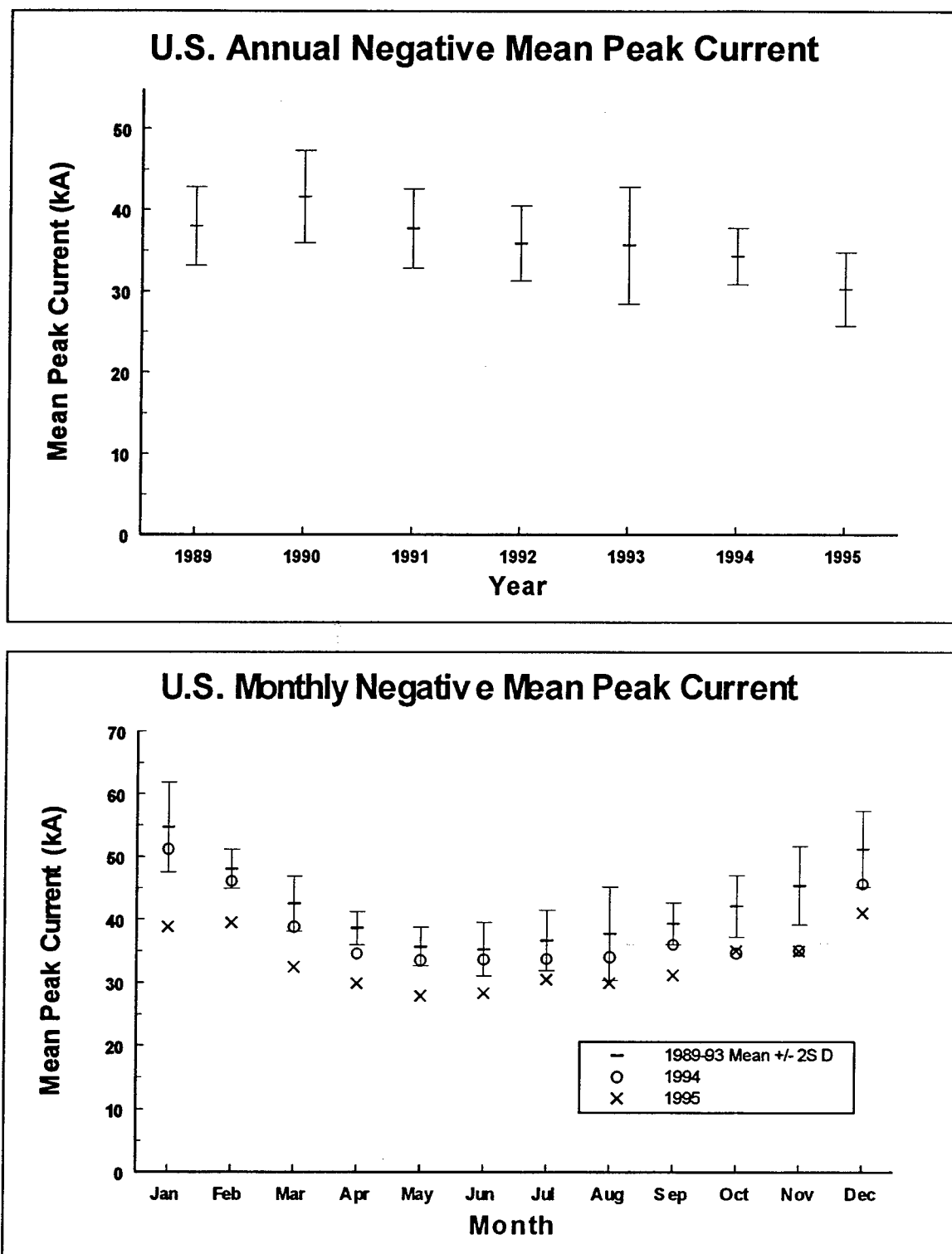


Fig. 4.14. US annual (top) and monthly (bottom) negative mean peak current, 1989-95. Error bars are two standard deviations above and below the mean.

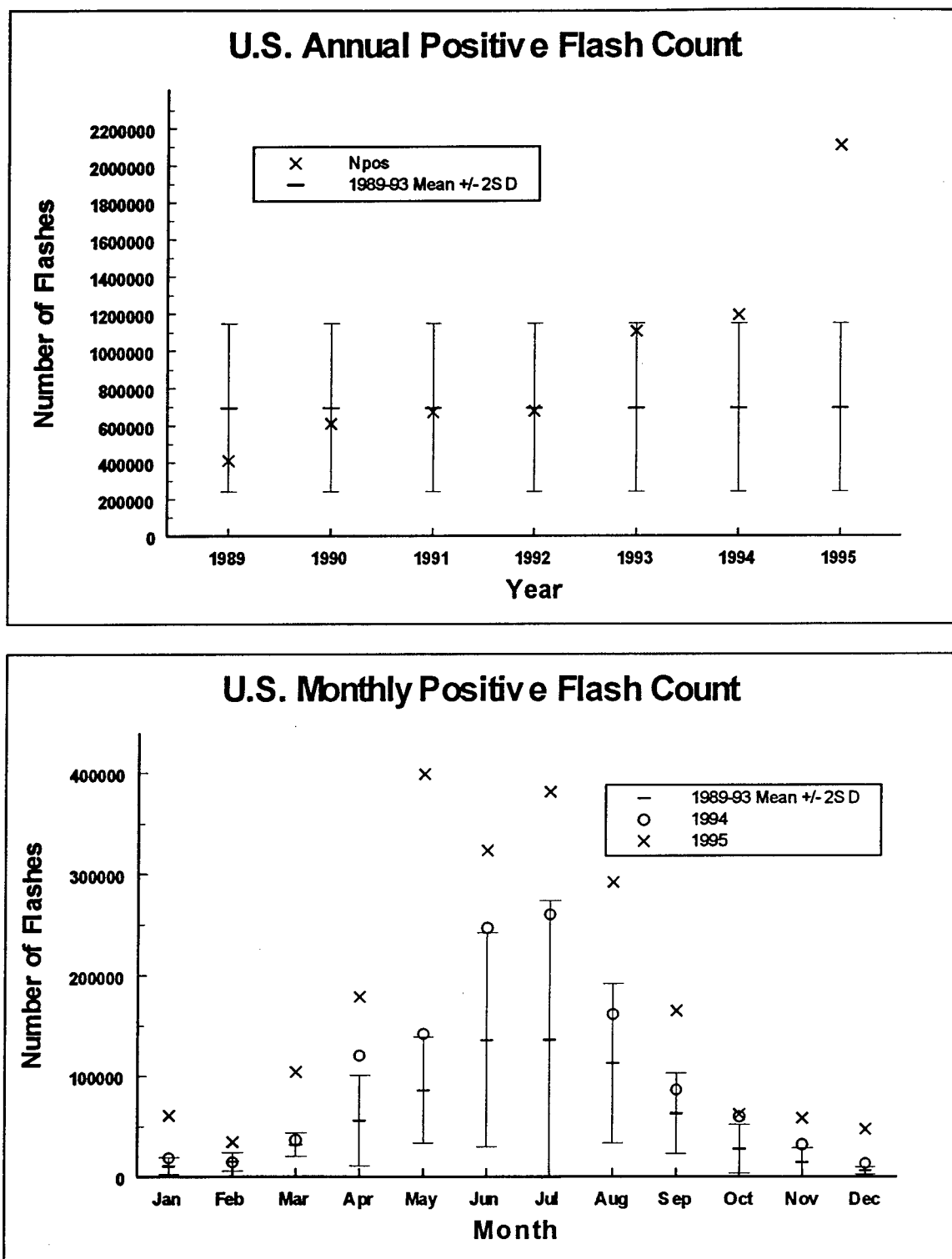


Fig. 4.15. US annual (top) and monthly (bottom) positive flash count, 1989-95. Error bars are two standard deviations above and below the mean.

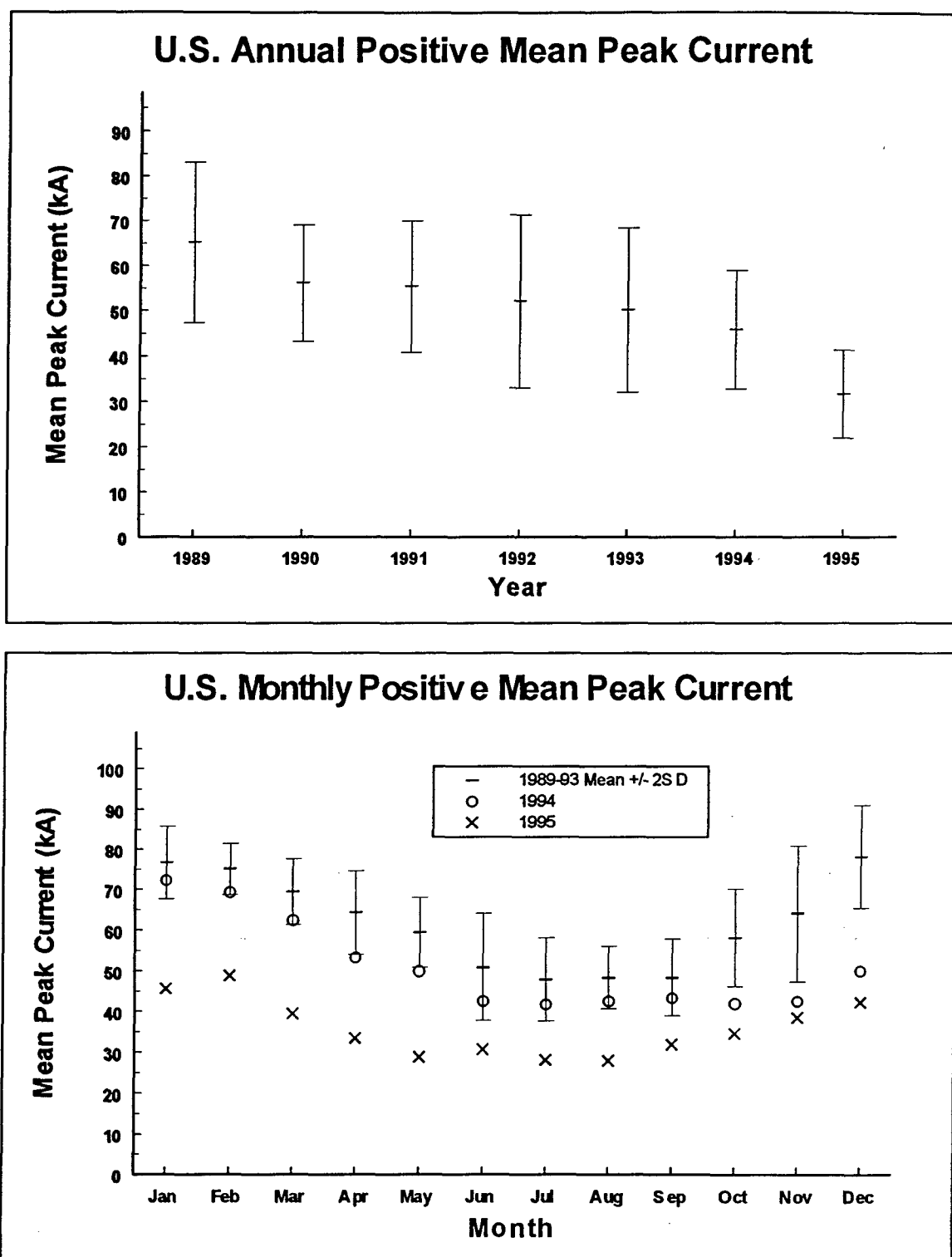


Fig. 4.16. US annual (top) and monthly (bottom) positive mean peak current, 1989-95. Error bars are two standard deviations above and below the mean.

## 2) Positive flashes

While the US negative flash count increases only slightly, the positive flash count increases significantly, as it does in each of the three regions. Table 4.3 and Fig. 4.15 show that the pre-upgrade mean positive flash count is approximately 696 000 flashes  $\text{yr}^{-1}$ . In 1994 this increases 2.19 standard deviations to 1.193 million flashes. The 1995 positive flash count is 6.22 standard deviations higher than the pre-upgrade mean at 2.107 million flashes, a threefold increase. Every month's positive flash count exceeds two standard deviations above the pre-upgrade mean after September 1994.

Table 4.3 and Fig. 4.16 depict US positive mean peak currents. The pre-upgrade mean is 54.4 kA, in close agreement with the Kansas and Ohio Valley data sets, but significantly higher than the Florida pre-upgrade mean. The 1994 US positive mean peak current is 1.87 standard deviations lower at 45.8 kA and the 1995 mean is 4.97 standard deviations lower at 31.6 kA. As for negative flashes, September 1994 marks the point where monthly positive mean peak currents first exceed two standard deviations below the pre-upgrade monthly mean peak currents.

### e. *US peak current distributions*

We conclude the NLDN data analysis by looking at the distribution of peak currents in negative and positive

flashes. The purpose for doing this is to determine if the increase in NLDN detected flash counts is dependent upon peak current.

1) Negative flashes

Fig. 4.17 is a histogram of US annual negative flash counts binned in 1 kA intervals. After the upgrade, the mode of the negative peak current distribution decreases from pre-upgrade values of between 24 and 26 kA to 20 kA in 1995. The flash count also increases slightly, as discussed earlier. The bottom half of Fig. 4.17 depicts the same data but with the pre-upgrade years (1989-93) replaced by the pre-upgrade mean flash count distribution with error bars two standard deviations above and below.

Fig. 4.18 depicts the same data normalized to the 1989-93 mean annual flash count distribution. The top half of the figure shows the ratio of flashes detected to the pre-upgrade mean flash count at each peak current interval. The bottom half depicts the same data in terms of standard deviations above or below the mean. This figure clearly shows that the post-upgrade increase in negative flash count is confined to flashes having peak currents less than 30 kA. Above 30 kA the 1995 flash counts are actually below the pre-upgrade mean. By contrast, 7 times the pre-upgrade mean number of flashes is detected at 5 kA in 1995. At 6 kA, the 1995 flash count is nineteen standard deviations above the

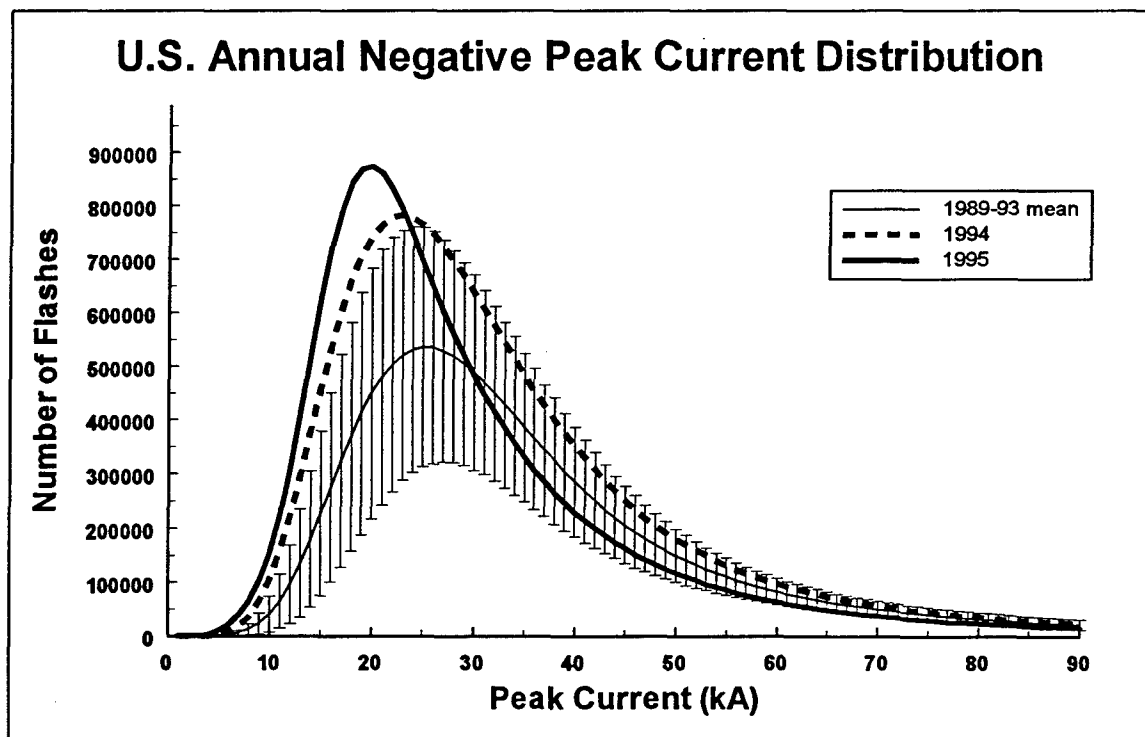
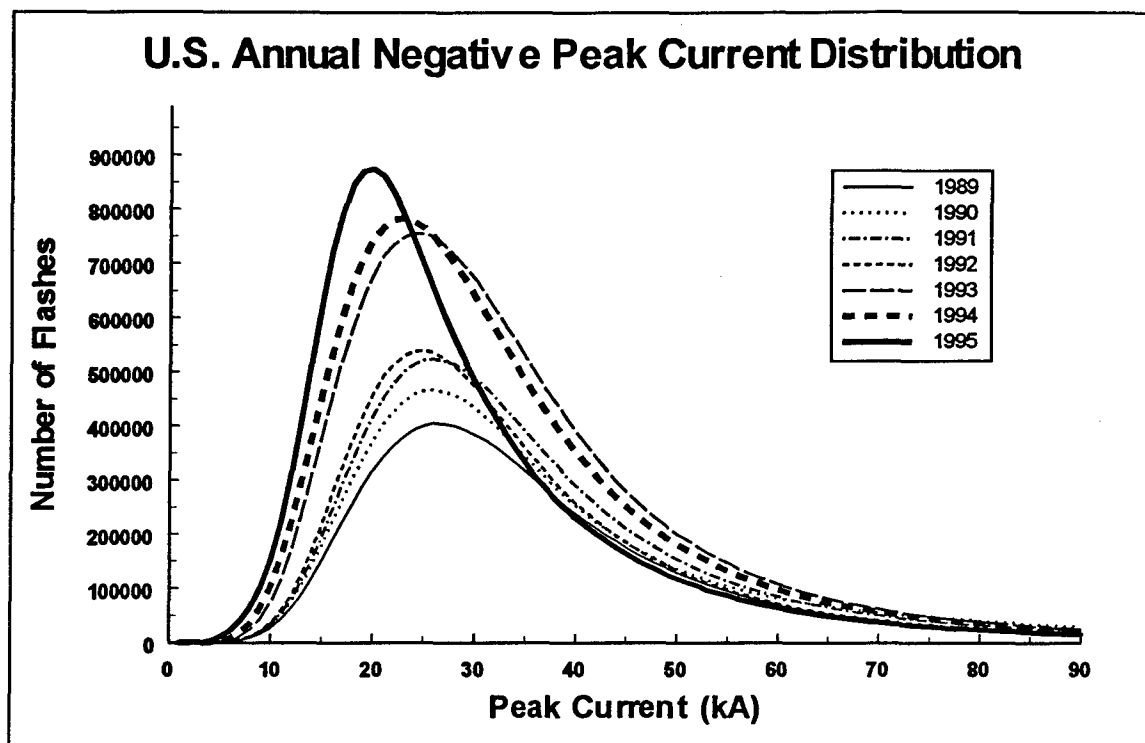


Fig. 4.17. US negative peak current distribution, 1989-95. Pre-upgrade years are depicted individually at top and the pre-upgrade mean is depicted at bottom. Error bars are two standard deviations above and below the 1989-93 mean.

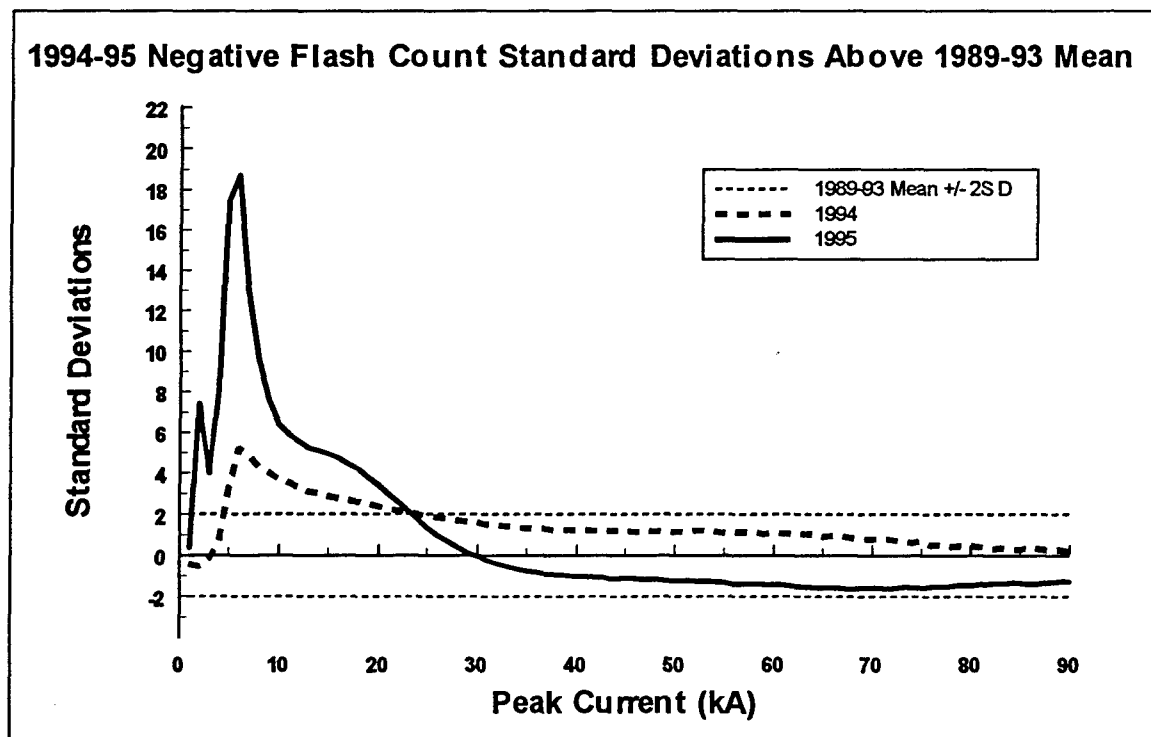
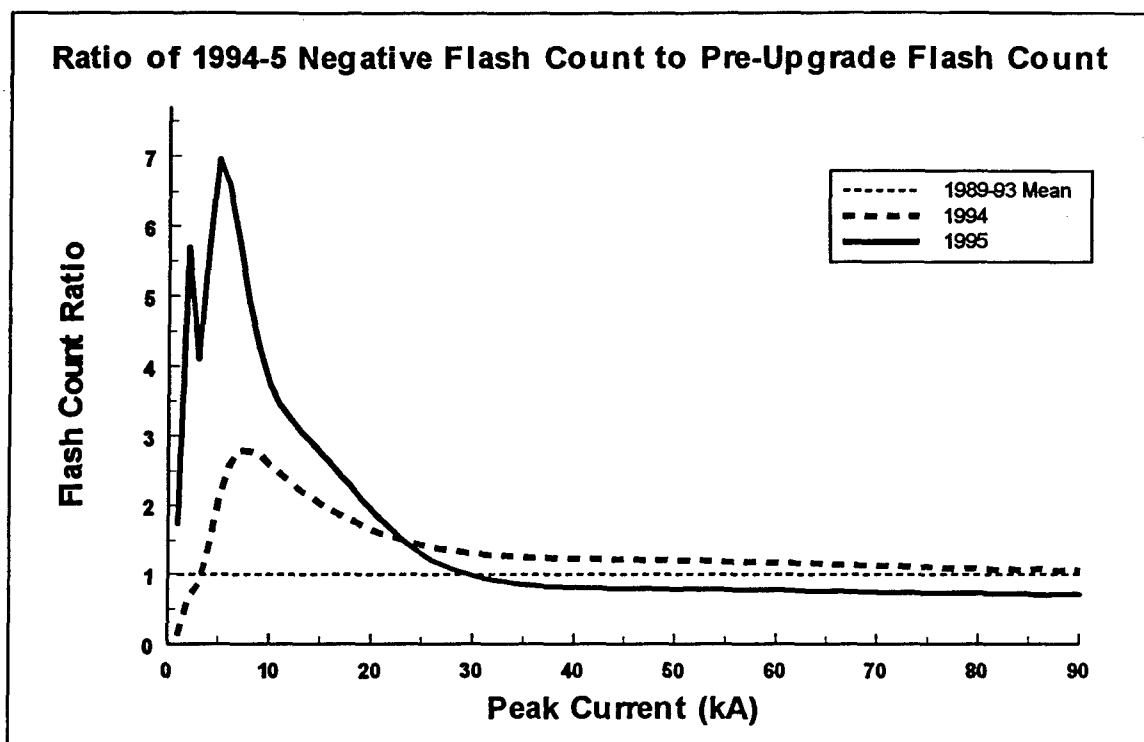


Fig. 4.18. US negative pre- to post-upgrade flash count ratio. 1994 and '95 flash counts are expressed as a ratio of the pre-upgrade mean at top and in terms of standard deviations above the pre-upgrade mean at bottom.

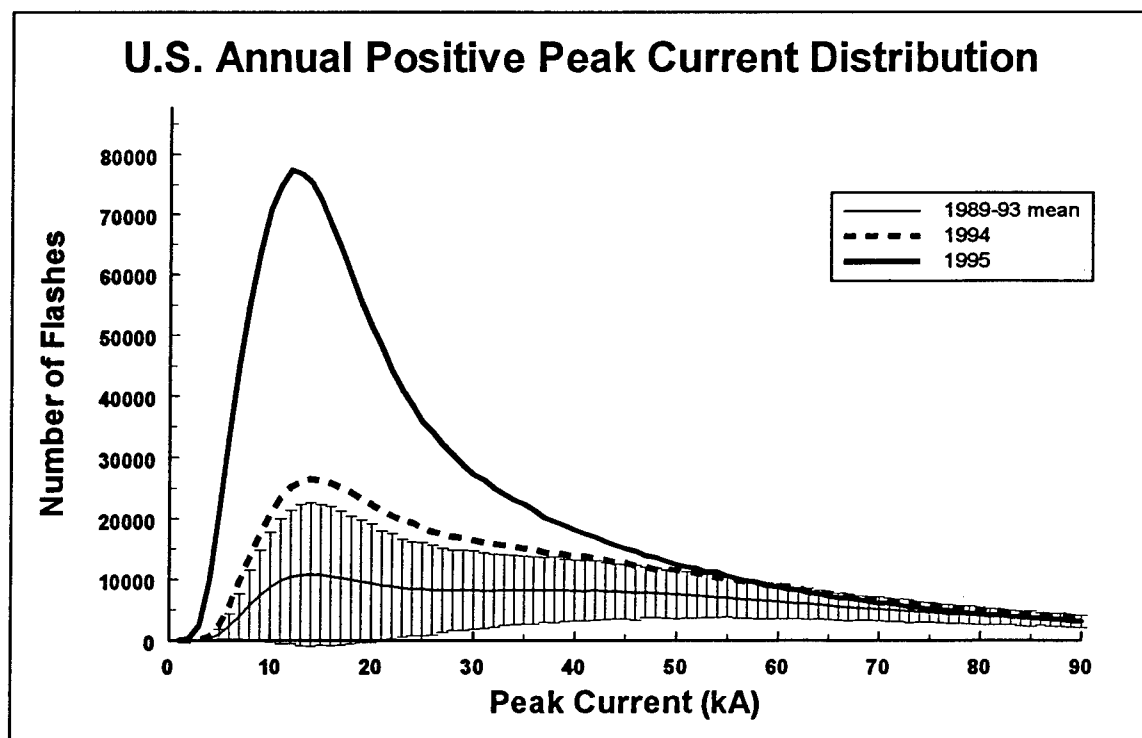
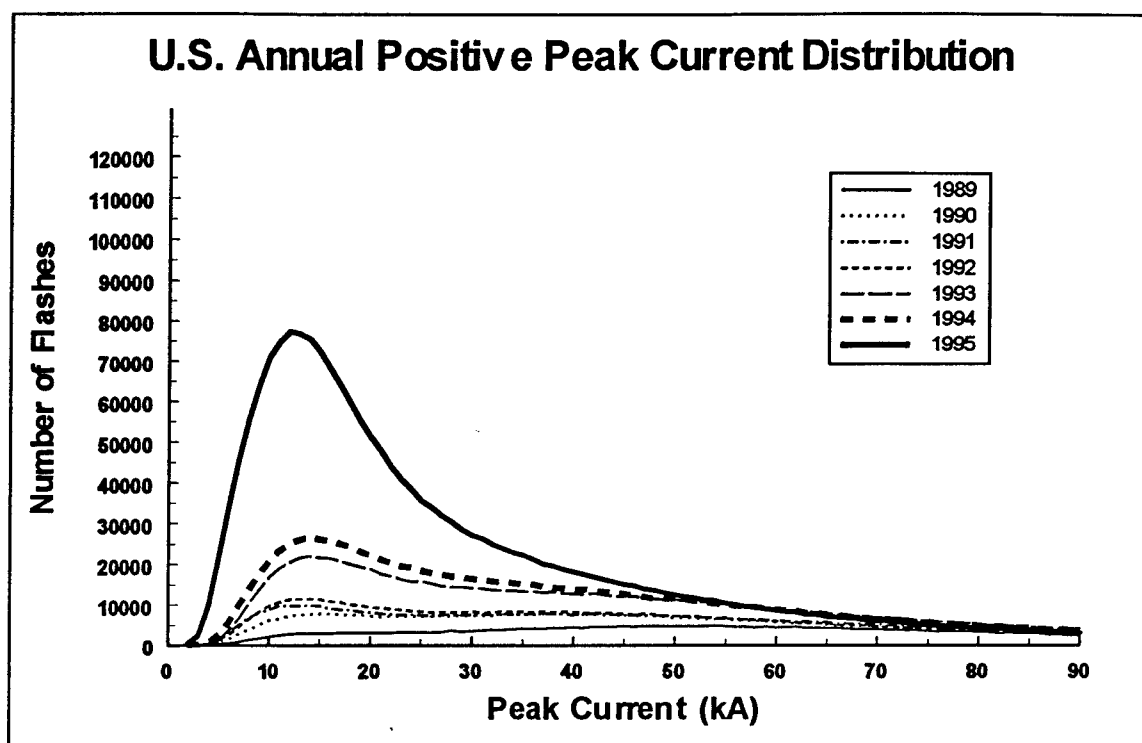


Fig. 4.19. US positive peak current distribution, 1989-95. Pre-upgrade years are depicted individually at top and the pre-upgrade mean is depicted at bottom. Error bars are two standard deviations above and below the 1989-93 mean.

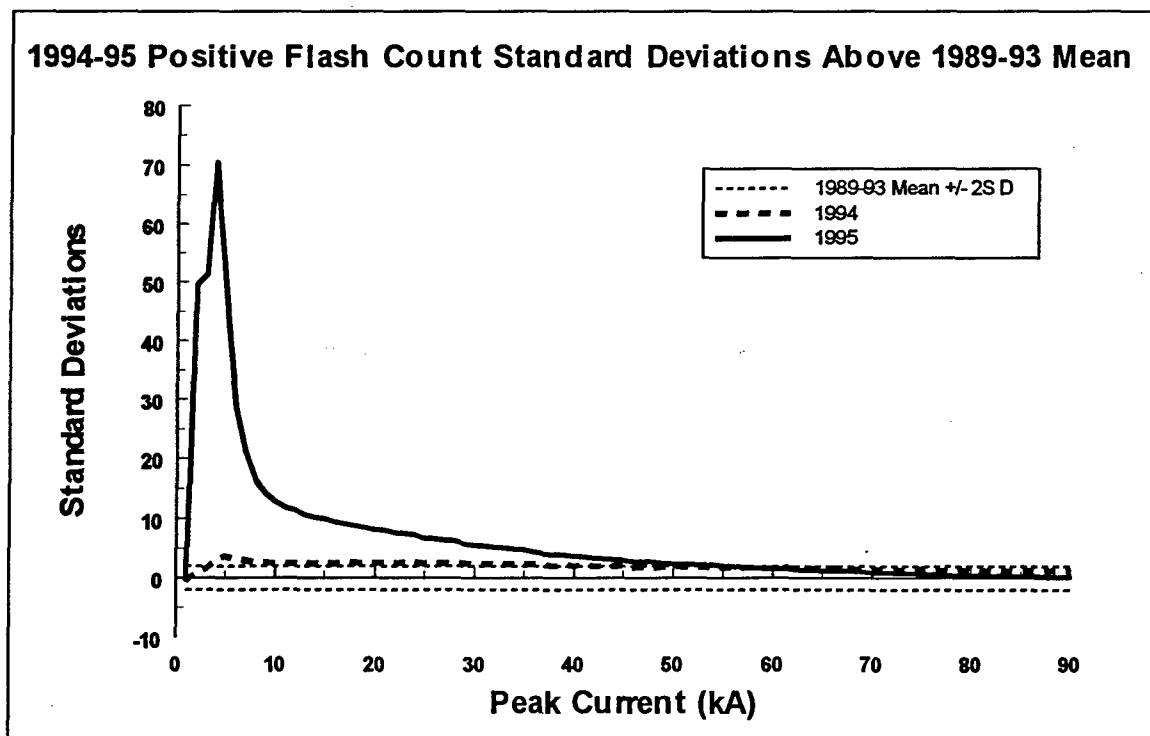
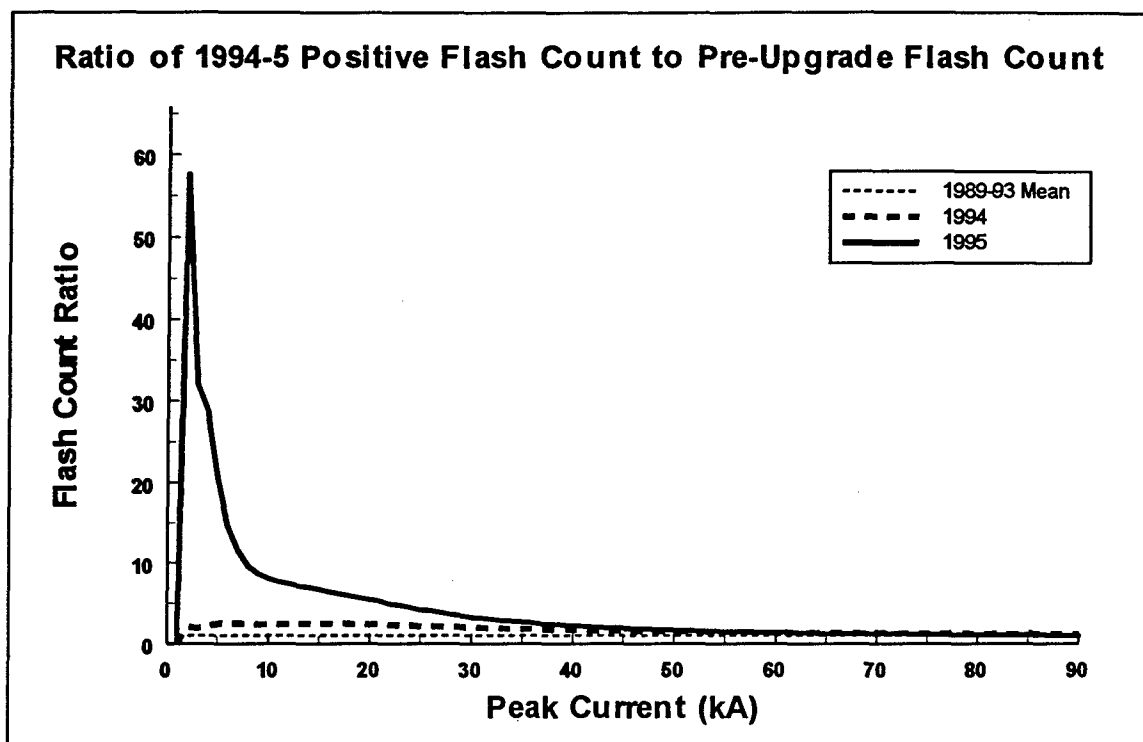


Fig. 4.20. US positive pre- to post-upgrade flash count ratio. 1994 and '95 flash counts are expressed as a ratio of the pre-upgrade mean at top and in terms of standard deviations above the pre-upgrade mean at bottom.

pre-upgrade mean flash count. At all peak currents less than 24 kA the 1995 flash count is in excess of two standard deviations greater than the pre-upgrade mean flash count.

## 2) Positive flashes

Like the negative flash count distribution, the positive flash count distribution is right-tailed, as shown in Fig. 4.19. Its mode is between 12 and 14 kA during 1989-93; the 1995 mode is also 12 kA. The post-upgrade increase in flash count is more evident than in the negative peak current distribution.

Fig. 4.20 depicts the positive flash count distribution normalized to the 1989-93 mean. The increase in weak flash counts is even more pronounced than for negative flashes. The 1995 2 kA positive flash count is 58 times greater than the pre-upgrade mean flash count, a 50 standard deviation increase. At 4 kA, the 1995 positive flash count is 72 standard deviations higher than the pre-upgrade mean flash count. As with negative flashes, the increase is confined to weaker flashes; above approximately 60 kA, there is no appreciable increase in positive flash count after the upgrade, while all flash counts below 56 kA are increased by more than two standard deviations.

## *f. Summary*

The statistical analysis of the US NLDN archived data set contained in this chapter has shown us that:

- 1) The post-upgrade negative flash count, while increased, is not statistically different from the pre-upgrade value.
- 2) The post-upgrade negative mean peak current decreases significantly after September 1994.
- 3) Unlike the post-upgrade negative flash count, the positive flash count increases significantly after September 1994.
- 4) The post-upgrade positive mean peak current decreases significantly after September 1994.
- 5) September 1994 marks the point where the upgrade first has a statistically significant (defined as a change in excess of two standard deviations) effect on all observed parameters except negative flash count.
- 6) The increase in both negative and positive flash counts occurs preferentially in weak flashes.

## CHAPTER V

### RETURN STROKE DETECTION MODELING

The purpose of this chapter is to model the changes made to the NLDN DFs during the 1994 network upgrade and compare the resulting changes in flash counts and mean peak currents to the results from Chapter IV. Two models are utilized. The first is a return stroke radiation model which computes radiation waveforms, peak signal strength, and signal pulsewidth of a model return stroke. The second is a detection model which uses output from multiple runs of the return stroke radiation model to compute peak current distributions of randomly located flashes with random peak currents detected by DFs. The peak current distribution of flashes detected by the model using pre- and post-upgrade pulsewidth detection criteria are compared with pre- and post-upgrade peak current distributions of archived NLDN data.

#### 1. Previous work

The processes composing a lightning flash have been modeled in various levels of detail for several decades. Most of this work has centered around modeling the electromagnetic radiation emitted by a return stroke, or the opposite problem, determining the spatial and temporal structure of the return stroke current from measured fields.

Over the course of this work, several return stroke current models have been developed and used.

a. *Return stroke current models*

All return stroke models in the literature assume a return stroke wavefront that travels up the channel, as in Chapter II, with a current waveform behind the wavefront that is a function of space, time, or both.

1) Simple models

Uman et al. (1975) use a simple triangular wave propagating up a channel, which has the disadvantage of two discontinuities in the current derivative. LeVine and Meneghini (1978) avoid this difficulty by using a compound exponential waveform.

2) The Bruce-Golde model

The Bruce-Golde, or BG, model is the oldest in use (it dates back to 1948) and assumes a current that is uniform behind the return stroke wavefront and 0 everywhere ahead of it (Uman and McLain 1970). Lin et al. (1980) showed that this is not a physically reasonable model, and the BG model's use has declined in recent years.

3) The transmission line model

The transmission line, or TL, and modified transmission line, or MTL, models are a broad category of models which represent the return stroke as a current pulse on a lossless transmission line (Uman 1987). This causes the return

stroke's waveform to remain constant in time as it propagates up the channel. TL models are still widely used in the literature and will be used in the model discussed in this chapter.

4) The Lin, Uman, and Standler model

In 1980, Lin et al. introduced the most complex model to date, the LUS model. It has three distinct components: a pulse component representing breakdown at the return stroke wavefront, a uniform component representing the residual leader current, and a corona component representing the discharge of the corona sheath created by the leader process.

The LUS pulse velocity is arbitrary and its risetime is equal to that of the measured fields. The uniform current component is determined by the measured vertical electric field derivative. The corona current is modeled as a series of discrete current sources turned on as the pulse passes and whose amplitude decreases exponentially with height (Lin et al. 1980).

The corona and uniform current components account for most of the charge transfer in the model. Channel tortuosity, or the degree of random twisting of the channel, as well as uncertainty in return stroke pulse velocity, leads to inaccuracies in modeled radiation (Lin et al. 1980).

#### 5) Modifications to the Lin, Uman, and Standler model

In 1981, Master et al. modified the LUS model by introducing a pulse current amplitude that decays with height, to reflect observational data (the MULS model). In 1994, Thottappillil and Uman added a height-dependent time constant to the channel discharge in the corona component (the VDTC model).

#### 6) Model evaluations

Nucci et al. (1990) evaluate the effectiveness of all of the above models using a common channel base current for each. Surprisingly, they find all produced reasonable approximations to actual return stroke radiation fields, while pointing out that no model could adequately represent the random noise imposed on return stroke radiation by channel tortuosity and branching.

For the specific purpose of computing peak fields from peak currents and vice versa, Thottappillil and Uman (1993) recommend using the TL model. During the initial few  $\mu$ s of a return stroke, they find it to perform as well as more complicated models. Since the peak field typically occurs very near the beginning of the return stroke radiation, the TL model's loss of accuracy with time does not affect peak field calculations.

For this reason, the return stroke model used here will be a TL model incorporating a sharp initial peak traveling

up the channel at constant velocity with an exponentially decaying current behind.

*b. Geometric effects*

From Maxwell's equations, we reason that the orientation of the channel affects the measured magnitude of the peak vertical electric field and azimuthal magnetic flux density (LeVine and Meneghini 1978).

Due to the "turn-on" and "turn-off" effects at each channel segment junction discussed in Chapter III, channel tortuosity results in more temporal fine structure in the return stroke radiation (LeVine et al. 1986; Uman 1987).

Channel branching profoundly affects first return stroke radiation fields by causing subsidiary peaks as the charge contained in each branch flows to ground (Weidman and Krider 1978). Willet et al. (1995) measure 18 dB more spectral power at high frequencies (from 500 kHz to 7 MHz) in first return strokes (with branches) than in subsequent return strokes.

Most models, including the one presented in this chapter, consider neither tortuosity nor branching, and so the radiation they produce is "cleaner" than actual return stroke radiation signatures, having neither the high frequency component nor the subsidiary peaks characteristic of actual return stroke radiation.

*c. Surface conductivity effects*

Due to the variability in surface composition, we expect that surface conductivity should vary. In no case, however, do we expect the ground to be a perfect conductor. Electromagnetic radiation propagating along a finitely conducting surface will be attenuated (Griffiths 1989). This causes the range normalized peak field strength of distant signals to be less than that of close signals (Lin et al. 1980). This is the source of the  $r^{-1.13}$  signal strength dependence found by Orville (1991) and Hiscox and Cummins (1993).

Attenuation occurs preferentially for high frequency radiation, causing the fine-structure of the return stroke waveform to decay with distance from the source (Uman 1987). The preferential attenuation at high frequencies may also contribute to a time delay between components of return stroke radiation having different characteristic frequencies (LeVine et al. 1986). Finally, since attenuation is caused by propagation along a non-perfectly conducting surface, it lessens with increasing height from which the radiation was emitted (LeVine et al. 1986).

**2. Finite difference return stroke field model**

Appendix C contains the MathCAD 6.0+ file used to compute the radiation emitted by a model CG return stroke. The user supplies channel geometry, peak current, return

stroke velocity, and spatial and temporal waveform. From this input, the model computes 1) the radiated vertical electric field strength and azimuthal magnetic flux density at a distance  $r$  from the channel, 2) the peak signal strength and range normalized signal strength (in LLP units) vs. range, and 3) the signal pulsewidth (time above the detection signal strength threshold) vs. range.

a. *Geometry*

Fig. 5.1 illustrates the geometry of the return stroke model. It uses a straight vertical channel with specified bottom and top heights. The observer is assumed to be at ground level. For the results presented in this chapter, a 2 km tall channel with base at the ground is used. The channel has no tortuosity and no branches, so high frequency components and subsidiary peaks are absent from the radiation.

The well-defined channel endpoints result in a temporal radiation field waveform that initially follows the current waveform at the bottom of the channel (due to the "turn on" effect), and that becomes a mirror image of the current waveform after it reaches the top of the channel (due to the "turn off" effect). In nature, the channel most often ends in a significant intercloud segment with more horizontal orientation. This tends to decrease or eliminate the "turn off" effect, which is not often observed in nature.

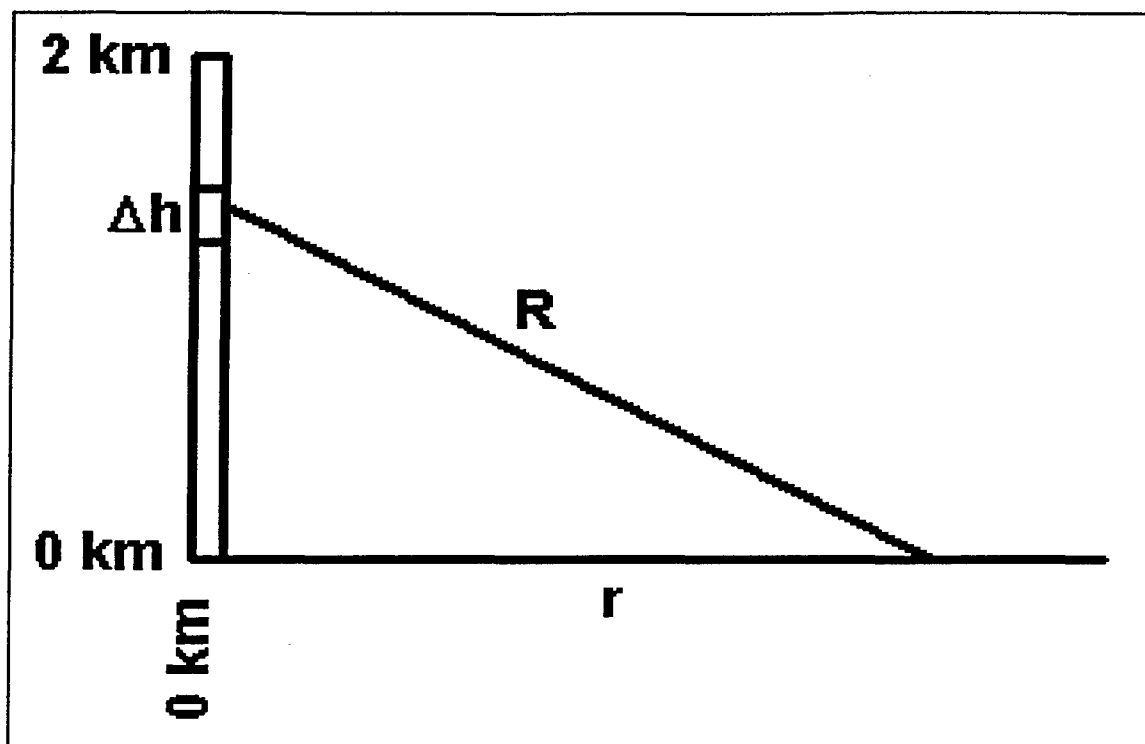


Fig. 5.1. Finite difference field model channel geometry. The channel is 2 km high and vertical. Azimuthal symmetry is assumed, so the radiation has only a radial dependence.

b. *Surface conductivity*

The field model presented here treats the ground as a perfect conductor, as do most models in the literature. This allows the use of the "method of images" discussed in Chapter III to compute the fields. It also eliminates any attenuation effects on the model results, so we expect peak signal strength to decrease as  $r^{-1}$  and the radiation fields to retain their high frequency components.

c. *Return stroke current model*

The return stroke current model presented here is a transmission line model--the temporal waveform of the return stroke current is constant. It is a simplified version of the LUS model, consisting of a sharp initial breakdown peak at the return stroke wavefront followed by a current decaying exponentially with height below it:

$$i(h,t) = i_{peak} \cdot e^{-\left(\frac{vt-h}{.5km}\right)} \quad (5.1)$$

The wavefront propagates up the channel at a constant velocity,  $v$ , of  $10^8$  m s<sup>-1</sup>. Fig. 5.2 is a snapshot of the channel current for a 30 kA peak current return stroke 15  $\mu$ s after the return stroke initiated at the surface. Based on conservation of charge in the channel, we can use a continuity equation to compute the charge density as a function of height and time, and find that its shape is identical to the current waveform. The return stroke

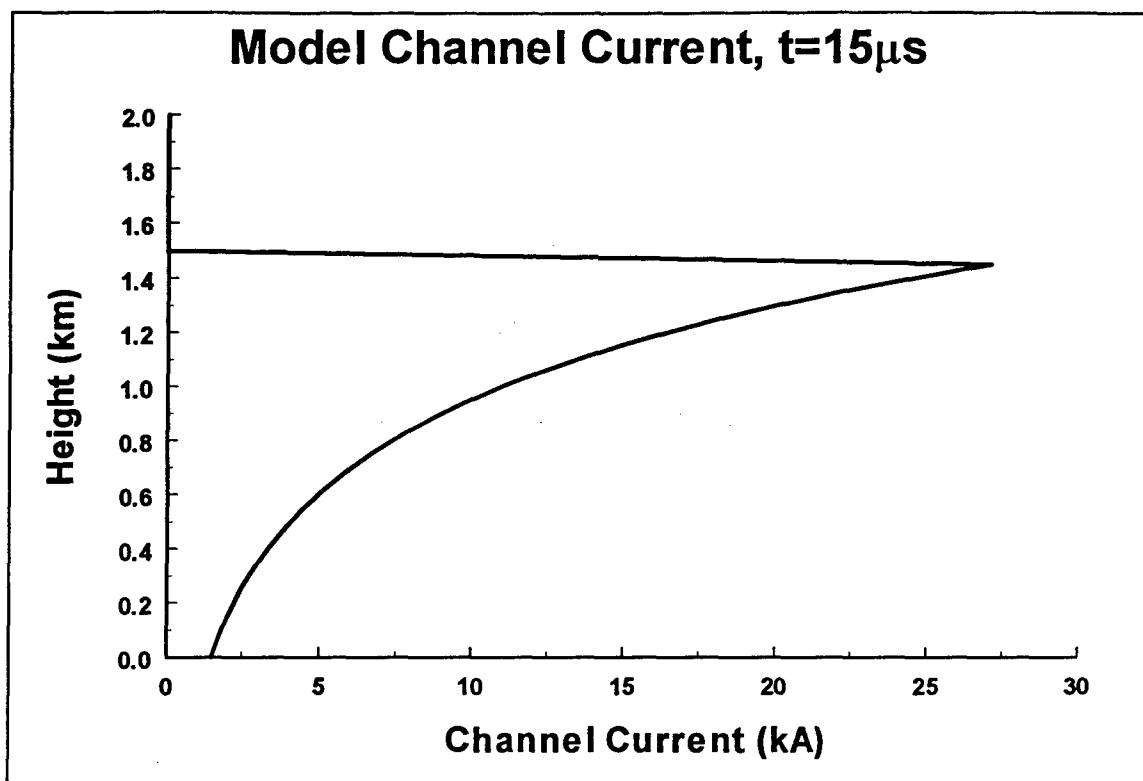


Fig. 5.2. Model channel current vs. height  $15\mu\text{s}$  after return stroke initiation. This is a snapshot of the current waveform for a model return stroke with peak current of 30 kA (the peak falls between channel grid points in this view, causing the peak to be truncated to 27 kA). The wavefront propagates up the channel at a velocity of  $10^8\text{ m s}^{-1}$ .

modeled here contains positive current flowing upward--this delivers a net positive charge upward, equivalent to delivering a net negative charge downward. Thus, we are modeling a negative CG return stroke.

*d. Finite difference representations of field equations*

We compute the fields in the same manner discussed in Chapter III, using the following finite difference approximations for the scalar and vector potential equations, making use of the method of images:

$$\phi(r, z, t) = \frac{1}{4\pi\epsilon_0} \sum_j \left[ \left[ \left( \frac{\rho(h_j, t - R_j/c)}{R_j} + \frac{\rho(h_{j-1}, t - R_{j-1}/c)}{R_{j-1}} \right) \cdot \left( \frac{\Delta h}{2} \right) \right] \right. \\ \left. + \left[ \left( \frac{-\rho(h_j, t - R_j/c)}{R_j} + \frac{-\rho(h_{j-1}, t - R_{j-1}/c)}{R_{j-1}} \right) \cdot \left( \frac{\Delta h}{2} \right) \right] \right] \quad (5.2)$$

$$A_z(r, t) = \frac{\mu_0}{4\pi} \sum_j \left[ \left[ \frac{i(h_j, t - R_j/c)}{R_j} + \frac{i(h_{j-1}, t - R_{j-1}/c)}{R_{j-1}} \right] \cdot \frac{\Delta h}{2} \right] \cdot 2 \quad (5.3)$$

where  $R_j = (r^2 + (h_j - z)^2)^{\frac{1}{2}}$  (refer to Fig. 5.1).

The vertical electric field strength and azimuthal magnetic flux density are then computed from the scalar and vector potentials:

$$E_z(r, t) = - \left[ \frac{\phi(r, z + \Delta z, t) - \phi(r, z - \Delta z, t)}{2\Delta z} \right] \\ - \left[ \frac{A_z(r, t + \Delta t) - A_z(r, t - \Delta t)}{2\Delta t} \right] \quad (5.4)$$

$$B_\phi(r, t) = - \left[ \frac{A_z(r + \Delta r, t) - A_z(r - \Delta r, t)}{2\Delta r} \right] \quad (5.5)$$

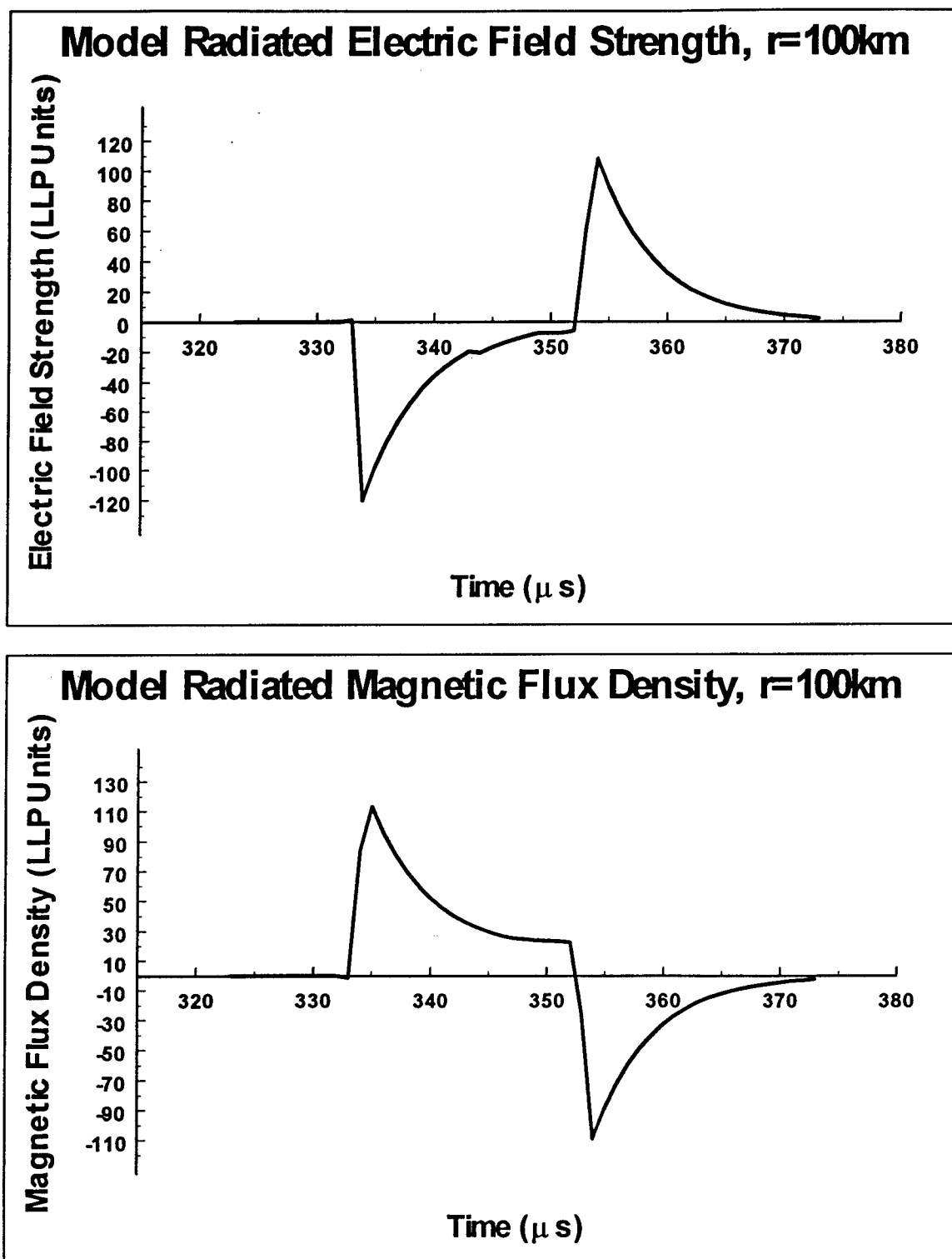


Fig. 5.3. Electric field strength (top) and magnetic flux density (bottom) measured 100 km from the 30 kA peak current model return stroke in Fig. 5.2. Time is measured from initiation of the return stroke.

As one would expect, the results of the numerical integrations and derivatives are sensitive to changes in grid sizes,  $\Delta r$  and  $\Delta z$ , and time step size,  $\Delta t$ , all of which are adjustable by the user.

Fig. 5.3 depicts the vertical electric field strength,  $E_z$ , and azimuthal magnetic flux density,  $B_\phi$ , measured a distance of 100 km from the channel for the 30 kA peak current return stroke depicted in Fig. 5.2. The turn-on and turn-off effects are clearly illustrated. As expected for a negative CG flash, the initial vertical electric field change is negative and the initial azimuthal magnetic flux density is positive (refer to Chapter III). Note that  $E_z$  and  $B_\phi$  are roughly equal to each other when expressed in LLP units. This corresponds to the  $B_\phi = E_z/c$  proportionality we expect based on the radiation field approximation.

e. *Signal strength and pulsewidth*

The model next determines the peak signal strength vs. range from the channel for ranges of 10 km to  $10^4$  km. The RNSS vs. range is computed by multiplying the peak signal strength by  $(r/100 \text{ km})$ . The signal pulsewidth vs. range is computed by measuring the length of time the electric field strength is above a threshold set by the user, in this case .112 mV, the detection threshold used in the NLDN sensors.

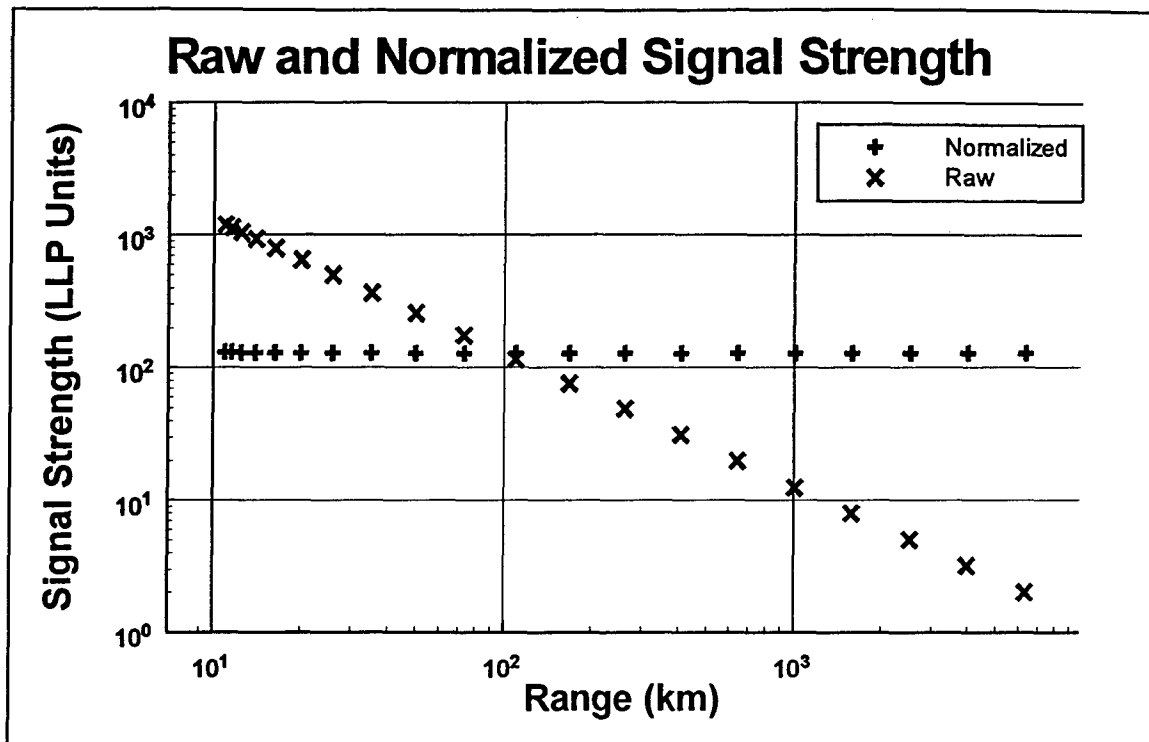


Fig. 5.4. Raw and normalized signal strength vs. range. Note the  $r^{-1}$  range dependence of raw signal strength.

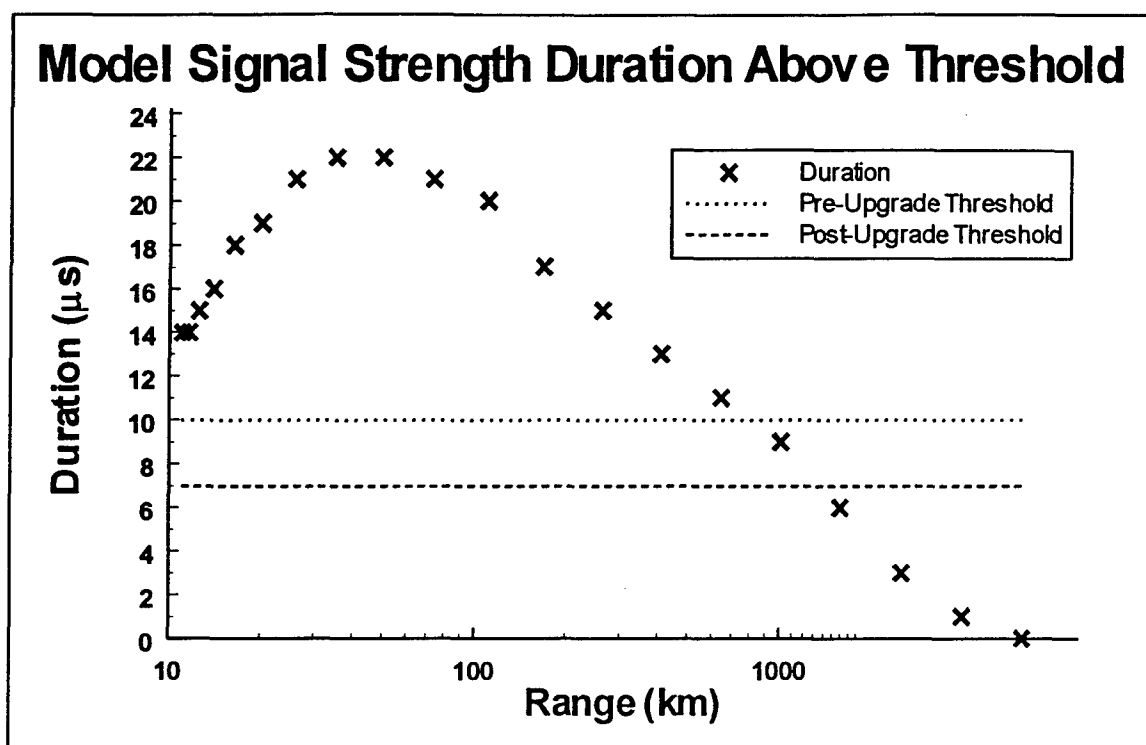


Fig. 5.5. Signal pulsewidth vs. range for the 30 kA return stroke modeled in Fig. 5.2. Both pre- and post-upgrade criteria, 10  $\mu\text{s}$  and 7  $\mu\text{s}$ , are depicted. Note that the range at which the pulsewidth drops below the detection criterion increases when we decrease the pulsewidth criterion.

Fig. 5.4 shows that the peak signal strength exhibits the  $r^{-1}$  dependence expected from the radiation field approximation and neglecting attenuation. The RNSS is constant with range, also as expected from the radiation field approximation.

Fig. 5.5, the pulsewidth vs. range plot, includes dotted and dashed lines at 10  $\mu$ s and 7  $\mu$ s, respectively, corresponding to the pulsewidth detection criteria used in the NLND DFs before and after the upgrade (refer to Chapter II). At large ranges where the pulsewidth is less than the detection criteria, the modeled 30 kA return stroke would not be detected by the model DF. The range where the pulsewidth equals the pulsewidth detection criteria is the theoretical maximum detection range of the DF for a flash having that peak current. Fig. 5.5 shows that decreasing the pulsewidth detection criteria from 10  $\mu$ s to 7  $\mu$ s increases the theoretical maximum detection range of the 30 kA flash.

*f. Repetitive model runs*

The results presented thus far are only for a return stroke with peak current of 30 kA. If we run the model repetitively for return strokes of different peak currents we can derive a maximum detection range vs. peak current relationship. Fig. 5.6 depicts this relationship

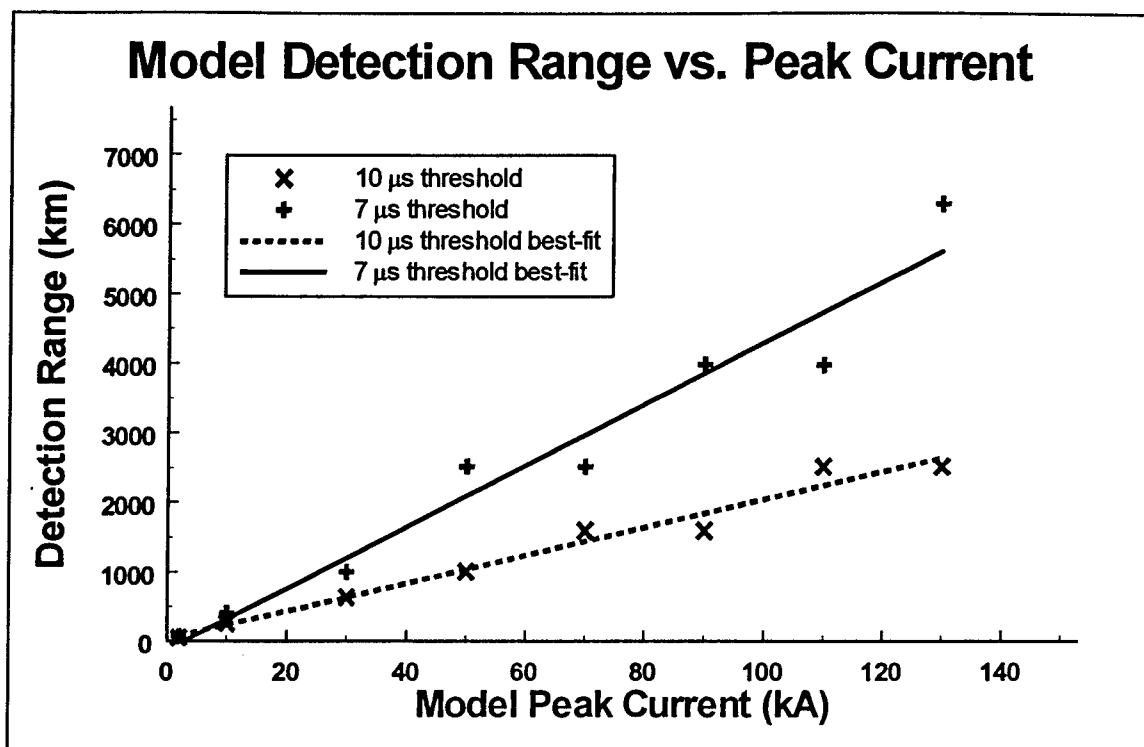


Fig. 5.6. Detection range vs. peak current for modeled return strokes having waveforms identical to Fig. 5.2 using detection pulsewidth criteria of 10  $\mu\text{s}$  and 7  $\mu\text{s}$ . Note that detection range for a flash of any given peak current increases when we decrease the pulsewidth criterion.

for return strokes of the same waveform and peak currents of 2, 10, 30, 50, 70, 90, 110, and 130 kA and both pulsewidth criteria.

Changing the pulsewidth criterion has no effect on the RNSS vs. peak current relationship. However, we see in Fig. 5.6 that decreasing the pulsewidth criterion increases the theoretical maximum detection range of a DF at all peak currents. We next model the detection of return strokes by a DF to investigate the effects of the increase in detection range on the detected flash peak current distribution.

### **3. Stochastic return stroke detection model**

Appendix D contains the MathCAD 6.0+ file used to model return stroke detection. Using the detection range vs. peak current relationships derived above for each pulsewidth criterion, the detection model computes peak current distributions of detected flashes. This is accomplished by generating a large number of model return strokes with random peak currents and random locations relative to a network of DFs and determining how many are detected using the pre- (10  $\mu$ s) and post-upgrade (7  $\mu$ s) pulsewidth criteria.

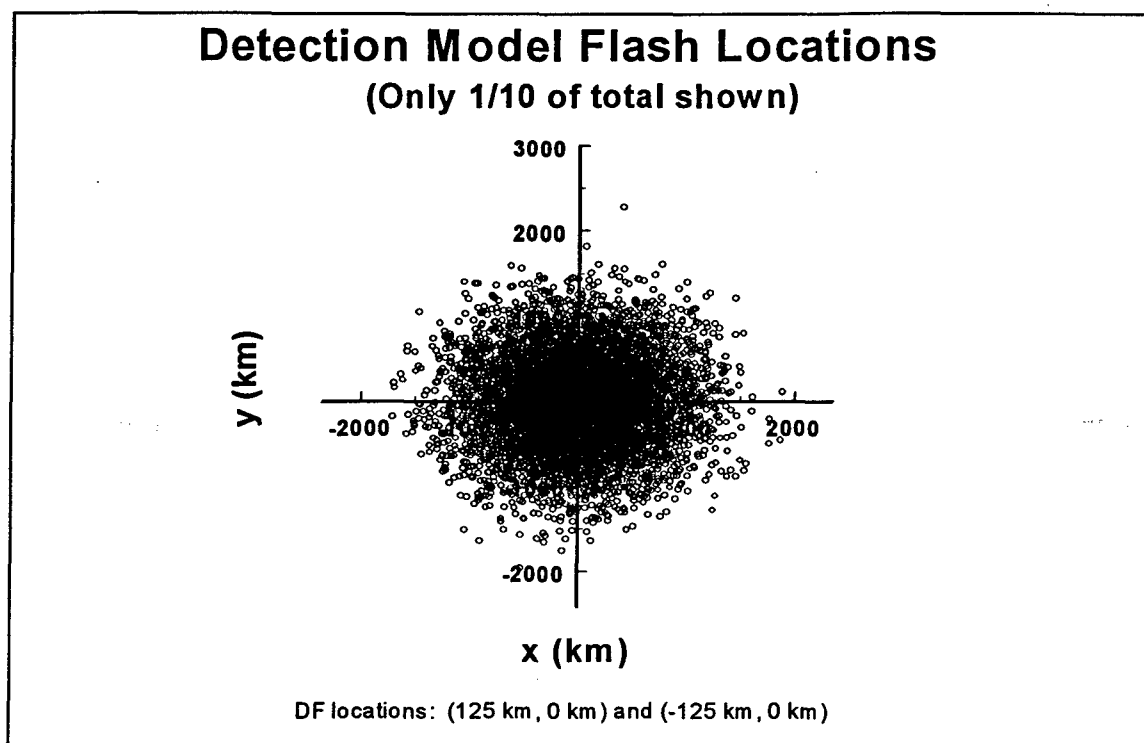


Fig. 5.7. Detection model randomly generated return stroke locations (only 1/10 of total shown for clarity).

a. *Geometry and peak current distribution of the stochastic model*

The model allows the user to set the number and x-y positions of multiple model DFs. For the following discussion, two DFs are used, located along the x-axis at  $x=\pm 125$  km. This 250 km spacing between the two model DFs corresponds to the approximate average spacing of DFs in the NLDN.

$10^5$  negative return strokes are generated with locations normally distributed about the origin with x and y standard deviations of 500 km. Thus we expect roughly 95% of the flashes to be within 1000 km of the origin. Fig. 5.7 depicts one tenth of the randomly generated flash locations to provide a sense of the flash locations.

The  $10^5$  flashes also have randomly generated peak currents. The peak currents were generated using both a  $\chi^2$  distribution and a uniform distribution. The  $\chi^2$  peak current distribution is probably more realistic but has very small sample sizes near the tails of the distribution. Since the analysis from Chapter IV dictates that we focus attention on weak flashes, the small sample size of the  $\chi^2$  distribution near 0 kA is a drawback. While not as realistic, the uniform distribution provides a large sample size at all peak currents of interest and eliminates any

bias the initial peak current distribution has on the detected flash peak current distribution.

*b. Detection criteria*

We consider a flash to be detected by an individual DF if it is within the maximum detection range for its peak current, as determined by the relationship computed earlier. In the NLDN, however, detection by multiple DFs is required in order to determine the location of a flash. We therefore require a model flash to be within detection range of *both* DFs to be detected.

*c. Results*

Fig. 5.8 depicts the peak current distribution of all flashes (solid line), and the peak current distribution of flashes detected with both the 10  $\mu$ s (dashed) and 7  $\mu$ s (dotted) pulsewidth criteria. At large peak currents, above approximately 70 kA, nearly all flashes are detected with either criterion. At lower peak currents, however, significantly more flashes are detected using the 7  $\mu$ s pulsewidth criterion. This increase is maximized around 20 kA, and at the other end of the peak current spectrum, near 0 kA, no flashes are detected using either pulsewidth criterion.

The top half of Fig. 5.9 depicts the detection efficiency, defined as the fraction of flashes detected, for

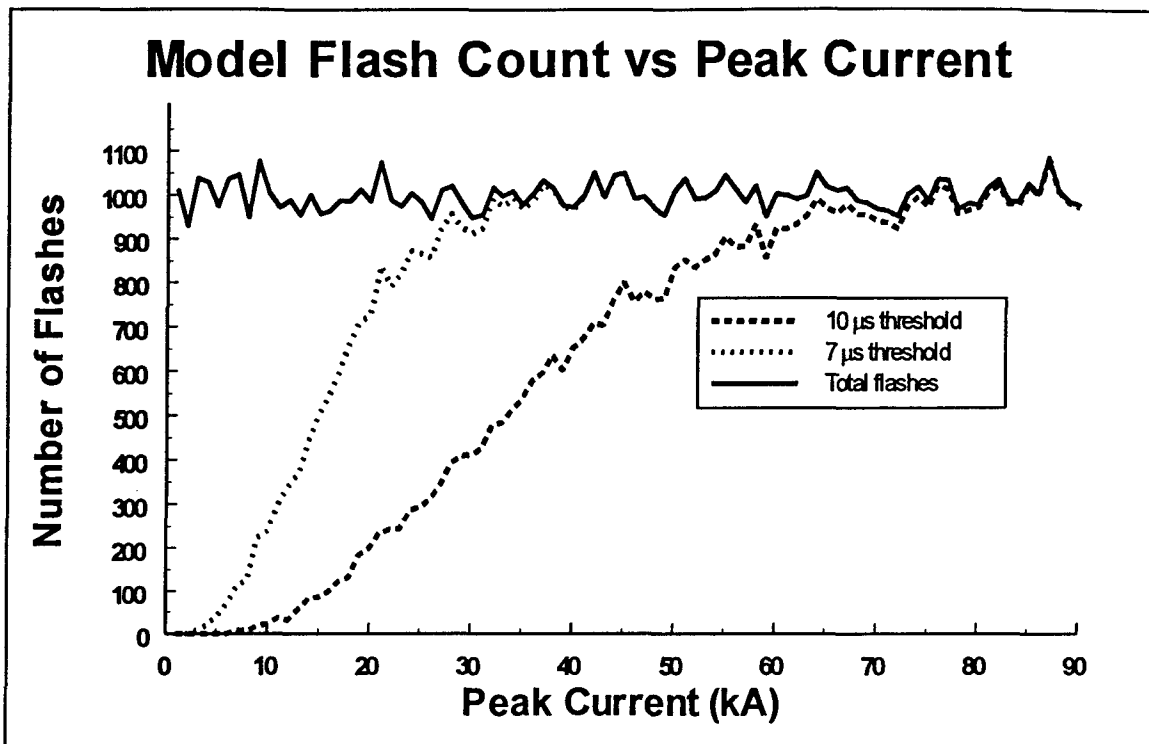


Fig. 5.8. Modeled return stroke detected flash count vs. peak current and detected flash counts at 10  $\mu$ s and 7  $\mu$ s pulsewidth criteria.

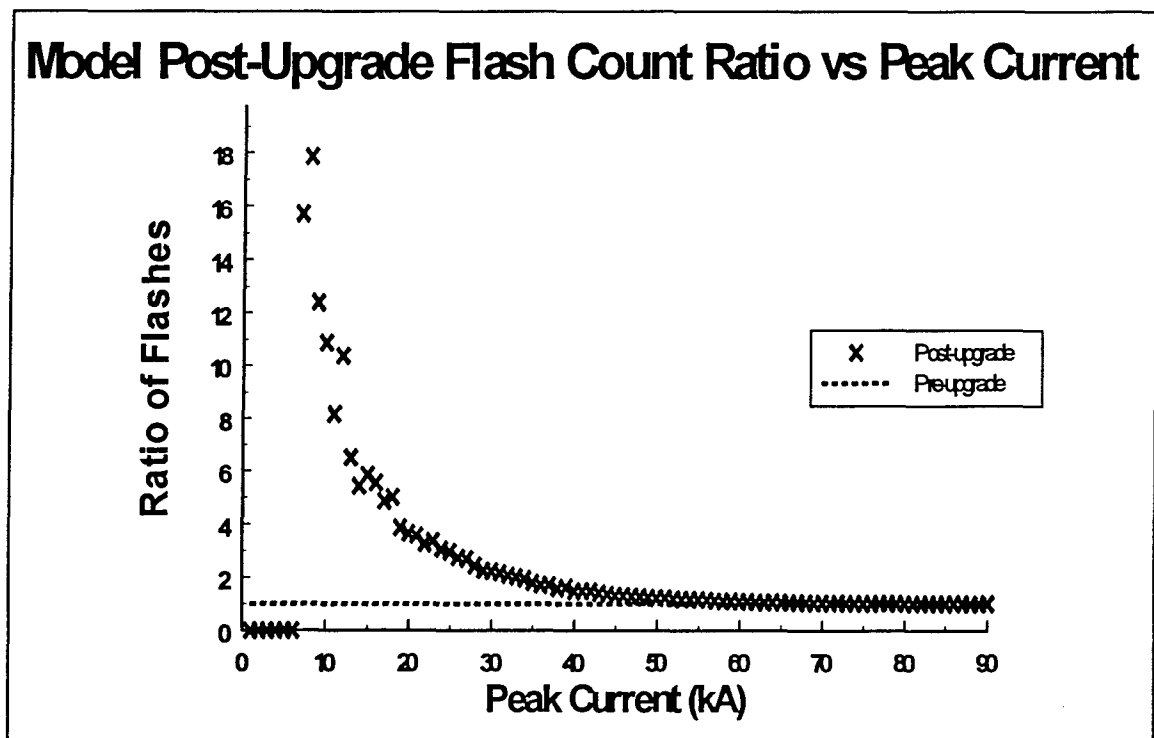
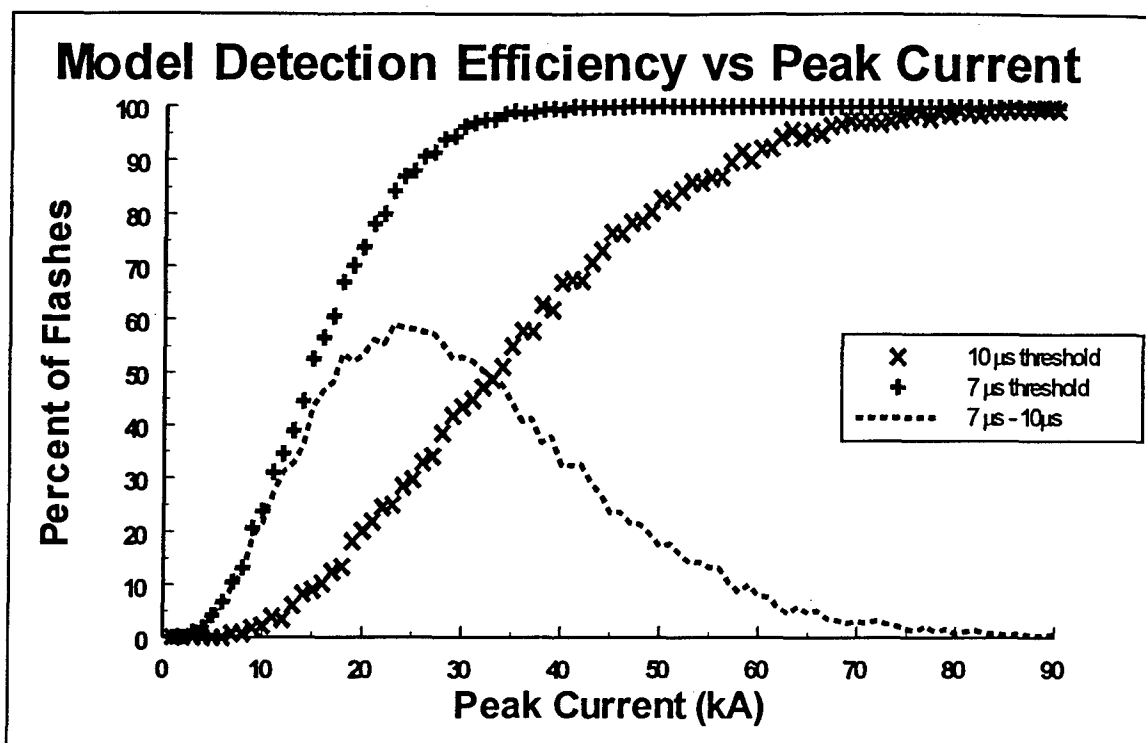


Fig. 5.9. Model detection efficiency vs. peak current at 10  $\mu$ s and 7  $\mu$ s pulsewidth criteria (top) and model post-upgrade flash count vs. peak current normalized to pre-upgrade flash count (bottom).

each pulsewidth criterion, and the difference in detection efficiencies. At high peak currents, both pulsewidth criteria result in near 100% detection efficiency due to the very large maximum detection range for those flashes compared to the DF spacing. As peak current decreases, the detection efficiency falls off more rapidly for the 10  $\mu$ s pulsewidth criteria. At 0 kA, both criteria result in 0% detection efficiency. The pre- to post-upgrade detection efficiency increase is maximized at 22 kA.

The bottom half of Fig. 5.9 depicts the post-upgrade flash count vs. peak current normalized to the pre-upgrade value. Comparing the bottom half of Fig. 5.9 with Figs. 4.18 and 4.20 reveals some qualitative similarities. Both the actual and the model post-upgrade flash count ratios are approximately 1 for large peak currents. This ratio increases to a peak of many times the pre-upgrade flash count below 10 kA, then decreases toward 0 as peak current decreases toward 0 kA.

In the US NLDN data, the post-upgrade negative flash count peaks at 7 times the pre-upgrade count at 6 kA and is approximately equal to the pre-upgrade count for peak currents above 30 kA. The modeled post-upgrade negative flash count peaks at 18 times the pre-upgrade count at 8 kA and is approximately equal to the pre-upgrade count for peak currents above 50 kA. The mean peak current of the model-

detected return strokes decreases from 65.3 kA before the hypothetical upgrade to 57.4 kA after.

Although the results are not presented here, the use of the  $\chi^2$  peak current distribution does not qualitatively affect the results.

## CHAPTER VI

## DISCUSSION AND CONCLUSIONS

## 1. Statistical significance of data

If we assume that the yearly mean peak current and flash counts are normally distributed about pre-upgrade mean values, then approximately 2.3% of the yearly mean values will lie more than two standard deviations above and 2.3% will lie more than two standard deviations below the pre-upgrade mean (Ott 1993). A two standard deviation increase or decrease in mean peak current or flash count after the upgrade therefore allows us to conclude with 97.7% certainty that the post-upgrade observed value is not caused by natural variance in the data. For the purposes of this discussion, a two standard deviation increase or decrease will define a significant, artificial change in the data.

As discussed in Chapter IV, the US post-upgrade negative flash count lies within two standard deviations of the pre-upgrade negative mean peak current, so we cannot conclude with much certainty that the observed increase in negative flash count has other than natural causes. By contrast, the US post-upgrade positive flash count is approximately six standard deviations higher than the pre-upgrade mean, leading us to conclude that the observed positive flash count is due to factors other than natural variability.

The US post-upgrade negative mean peak current is approximately three standard deviations lower than the pre-upgrade mean, leading us to conclude that the observed change is not a natural phenomenon. Finally, the US post-upgrade positive mean peak current is approximately five standard deviations below the pre-upgrade value, also leading us to conclude that something other than natural variability is responsible for the observed change.

In summary, then, we conclude that since the upgrade the NLDN is detecting significantly more positive flashes and that the mean peak current of detected negative and positive flashes is significantly lower.

## **2. Detection modeling results**

The return stroke radiation model presented in Chapter V shows that decreasing the pulsewidth detection criterion used by the DFs in the NLDN effectively increases the maximum detection range of a return stroke with any given peak current.

The return stroke detection model further shows that if the maximum detection range of return strokes is increased in a network of DFs with constant spacing, the increase in flash count occurs primarily for weak flashes. Using a random sample of return strokes with normally distributed positions and uniformly distributed peak currents, post- to pre-upgrade flash count ratios similar to those found in the

archived NLDN data result. Additionally, the mean peak current of detected flashes decreases.

### **3. Possible explanation of peak current decrease and flash count increase**

Based on the combined results of Chapters IV and V, a possible explanation of the post-upgrade mean peak current decrease is the increased detection efficiency of weak flashes in the NLDN, caused by the decrease in DF detection pulsewidth criterion from 10  $\mu$ s to 7  $\mu$ s during the upgrade.

Decreasing the pulsewidth detection criterion effectively increases the detection range of a given flash. The detection range of strong flashes exceeds the average spacing between DFs using either criterion and therefore guarantees that multiple DFs will detect strong flashes, regardless of pulsewidth criterion used. Weak flashes, on the other hand, may have detection ranges significantly less than DF spacing using one or both pulsewidth criteria. But by decreasing the pulsewidth criterion and thereby increasing the detection range vs. peak current relation, more weak flashes are detectable by the NLDN after the upgrade.

So we observe an increase in weak flash count and little or no change on strong flash count. The net effect of the increased presence of weak flashes in the NLDN data is to decrease the mean peak current of detected flashes.

Decreasing the pulsewidth detection criteria is not the only sensor change that would produce this result. In fact, any change which increases DF detection range for a given flash would have the same effect. Since all of the changes incorporated into the DFs during the upgrade were intended to improve detection efficiency, they all had the complementary effect of increasing the percentage of weak flashes detected.

Note that this explanation does not account for the larger increase in weak positive flash count than in weak negative flash count. A possible clue to the difference can be found in the nature of cloud flashes. Since cloud flashes move charge between cloud charge regions, they typically move negative charge upward or positive charge downward (as a consequence of the double-dipole cloud charge structure). Both processes result in emitted radiation from cloud flashes of positive polarity (i.e. positive charge moving downward). Cloud flashes tend to have small peak currents (<10 kA), and have pulsewidths on the order of 10  $\mu$ s (Krider et al. 1979).

So cloud flashes with unusually long (>10  $\mu$ s) pulsewidths may meet the CG flash detection criteria and be mistaken for CG flashes. Decreasing the DF pulsewidth detection criteria from 10  $\mu$ s to 7  $\mu$ s would allow even more

cloud flashes to be accepted by the CG flash detection criteria.

The increased percentage of positive flashes observed after the NLDN upgrade may therefore be a consequence of increased contamination of CG flash data by cloud flashes caused by decreasing the pulsewidth detection criterion. Increasing sensor gain may also increase detection of the weak cloud flash radiation signal that previously went largely undetected.

If we look closely again at Fig. 4.19, we see that the positive peak current distributions for pre-upgrade years are bimodal. There is a large peak between 10 and 15 kA and a much more subtle peak between 40 and 45 kA. The two separate peaks in the distribution hint at two separate processes taking place, i.e. detection of both cloud flashes and positive CG flashes. Fig. 4.19 shows that the increase in positive flash count is largest near the lower peak.

So in addition to decreasing the mean peak current of detected positive and negative flashes, the NLDN upgrade may have had the unwanted effect of increasing the contamination of positive CG flash data by cloud flashes.

Another possibility is that the NLDN is now able to detect a new type of positive CG lightning waveform (Brook 1996).

#### 4. Recommendations

These results suggest that caution must be used in comparing lightning data from before and after the 1994 network upgrade. As Cummins et al. (1995) point out, "variations in [detection efficiency] can seriously affect the measured peak current distribution, as well as the measured percent of events that have a positive polarity". With this in mind, it may be beneficial to attempt to develop a correction factor to convert pre-upgrade flash distributions to equivalent post-upgrade values in order to eliminate the effects of the upgrade in comparing annual data sets.

A more extensive detection model that incorporates the actual DF positions would be useful in determining the post-upgrade effects on detected flash count distributions using the actual NLDN DF locations. This would enable an estimate of the actual NLDN detection efficiency before and after the upgrade, and provide a basis for such a conversion.

Finally, further DF calibration studies are needed. The existing calibrations by Orville (1991) and Idone et al. (1993) consider only negative triggered return strokes with peak currents less than 60 kA detected by a handful of DFs in a limited geographical area. This allows the conductivity of Florida soil and possible azimuthal biases of the DFs used in the calibration to skew the results. A

new post-upgrade calibration including a wide geographic range within the NLDN, a wider peak current range, and both negative and positive flashes, would improve the accuracy of NLDN peak current measurements.

## REFERENCES

- Bass, Randall G., 1996: A Decision Model for Thunderstorm Prediction at Whiteman Air Force Base, Missouri. M.S. thesis, Texas A&M University, 138 pp.
- Beasley, William H., Paula V. Reid, and Douglas M. Jordan, 1993: Animated Cartoon of a Cloud-to-Ground Lightning Flash. *17th Conference on Severe Local Storms/Conference on Atmospheric Electricity*, St. Louis, Missouri, 4-8 Oct 1993.
- Brook, Marx, 1996: Personal communication to Dr. Richard E. Orville, 28 May 1996.
- Cooray, Vernon and Hugo Pérez, 1994: HF Radiation at 3 MHz Associated with Positive and Negative Return Strokes. *J. Geophys. Res.*, **99**, 10633-40.
- Cummins, Kenneth L., 1995: Personal communication to Dr. Richard E. Orville, 2 Feb 1995.
- , Edward A. Bardo, William L. Hiscox, Richard B. Pyle, and Albur E. Pifer, 1995: NLDN '95: A Combined TOA/MDF Technology Upgrade of the U.S. National Lightning Detection Network. *International Aerospace and Ground Conference on Lightning and Static Electricity*, Williamsburg, Virginia, 26-28 Sept 1995.
- , John Cramer, and Bill Hiscox, 1996: NLDN Peak Current Estimates - 1996 Update. Technical note, Global Atmospheric, Inc., Tucson, Arizona, 15 Jul 1996.
- , 1996: Personal communication to Dr. Richard E. Orville, 27 Aug 1996.
- Griffiths, David J, 1989: *Introduction to Electrodynamics*. Prentice-Hall, 532 pp.
- Hiscox, Bill and Ken Cummins, 1993: Report on Signal Strength Measurements in the NLDN. Technical note, GeoMet Data Services, Inc., Tucson, Arizona, 15 Jul 1993.
- Idone, Vincent P., Arsalan B. Saliougy, Ronald W. Henderson, Paul K. Moore, and Richard B. Pyle, 1993: A Reexamination of the Peak Current Calibration of the National Lightning Detection Network. *J. Geophys. Res.*, **98**, 18323-32.
- Krider, E.P., C.D. Weidman, and D.M. Levine, 1979: The Temporal Structure of the HF and VHF Radiation Produced by Intracloud Lightning Discharges. *J. Geophys. Res.*, **84**, 5760-2.

- , R.C. Noggle, A.E. Pifer, and D.L. Vance, 1980: Lightning Direction-Finding Systems for Forest Fire Detection. *Bull. Amer. Met. Soc.*, **61**, 980-6.
- LeVine, D.M. and R. Meneghini, 1978: Electromagnetic Fields Radiated from a Lightning Return Stroke: Applications of an Exact Solution to Maxwell's Equations. *J. Geophys. Res.*, **83**, 2377-84.
- , L. Gesell, and Michael Kao, 1986: Radiation from Lightning Return Strokes Over a Finitely Conducting Earth. *J. Geophys. Res.*, **91**, 11897-908.
- Lightning Location and Protection, Inc. 1992: Advanced Lightning Direction Finder Manual. Lightning Location and Protection, Inc., Tucson, Arizona. Revised 22 Jul 1992.
- Lin, Y.T., M.A. Uman, J.A. Tiller, R.D. Brantley, W.H. Beasley, E.P. Krider, and C.D. Weidman, 1979: Characterization of Lightning Return Stroke Electric and Magnetic Fields from Simultaneous Two-Station Measurements. *J. Geophys. Res.*, **84**, 6307-14.
- , M.A. Uman, and R.B. Standler, 1980: Lightning Return Stroke Models. *J. Geophys. Res.*, **85**, 1571-83.
- Lucas, Christopher and Richard E. Orville, 1996: TOGA COARE: Oceanic Lightning. *Mon. Wea. Rev.*, **124**, 2077-82.
- Master, M.J., M.A. Uman, Y.T. Lin, and R.B. Standler, 1981: Calculations of Lightning Return Stroke Electric and Magnetic Fields Above Ground. *J. Geophys. Res.*, **86**, 12127-32.
- Nucci, C.A., G. Diendorfer, M.A. Uman, F. Rachidi, M. Ianoz, and C. Mazzetti, 1990: Lightning Return Stroke Current Models With Specified Channel-Base Current: A Review and Comparison. *J. Geophys. Res.*, **95**, 20395-408.
- Orville, Richard E., R. W. Henderson, and L.F. Bosart, 1983: An East Coast Lightning Detection Network. *Bull. Amer. Meteor. Soc.*, **64**, 1029-37.
- , 1990: Peak-Current Variations of Lightning Return Strokes as a Function of Latitude. *Nature*, **343**, 149-51.
- , 1991: Calibration of a Magnetic Direction Finding Network Using Measured Triggered Lightning Return Stroke Peak Currents. *J. Geophys. Res.*, **96**, 17135-42.

- , 1993: Lightning: Impacts and Applications in Aviation Meteorology Forecasting. *Second Aviation Weather Workshop*, Boulder, CO, 16-19 Nov 1993.
- , 1994: Cloud-to-Ground Lightning Flash Characteristics in the Contiguous United States: 1989-91. *J. Geophys. Res.*, **99**, 10833-41.
- Ott, R. Lyman, 1993: *An Introduction to Statistical Methods and Data Analysis*. Wadsworth, 1051 pp.
- Rachidi, Farhad, and Rajeev Thottapillil, 1993: Determination of Lightning Currents from Far Electromagnetic Fields. *J. Geophys. Res.*, **98**, 18315-21.
- Rakov, Vladimir A., Rajeev Thottapillil, and Martin A. Uman, 1992: On the Empirical Formula of Willett et al. Relating Lightning Return-Stroke Peak Current and Peak Electric Field. *J. Geophys. Res.*, **97**, 11527-33.
- Thottapillil, Rajeev and Martin A. Uman, 1993: Comparison of Lightning Return-Stroke Models. *J. Geophys. Res.*, **98**, 22903-14.
- and Martin A. Uman, 1994: Lightning Return Stroke Model with Height-Variable Discharge Time Constant. *J. Geophys. Res.*, **99**, 22773-80.
- Uman, Martin A. and Kenneth McLain, 1970: Lightning Return Stroke Current from Magnetic and Radiation Field Measurements. *J. Geophys. Res.*, **75**, 5143-7.
- , D. Kenneth McLain, and E. Philip Krider, 1975: The Electromagnetic Radiation from a Finite Antenna. *Amer. J. Phys.*, **43**, 33-8.
- , 1987: *The Lightning Discharge*. Academic Press, 377 pp.
- Weidman, Charles D. and E. Philip Krider, 1978: The Fine Structure of Lightning Return Stroke Wave Forms. *J. Geophys. Res.*, **83**, 6239-47.
- Willet, J.C., J.C. Bailey, V.P. Idone, A. Eybert-Berard, and L. Barret, 1989: Submicrosecond Intercomparison of Radiation Fields and Currents in Triggered Lightning Return Strokes Based on the Transmission-Line Model. *J. Geophys. Res.*, **94**, 13275-86.

**APPENDIX A****ORVILLE AND IDONE ET AL. PEAK CURRENT CALIBRATIONS**

This appendix contains the MathCAD 6.0+ files used to duplicate the Orville 1991 and Idone et al. 1993 DF calibrations, correct the Orville 1991 calibration for an error in the position of one of the DFs, and recalculate each with the intercept of the best-fit line constrained to 0 kA.

## Verification of Calibration Paper by Orville (1991)

25 June 96

Constants:   ORIGIN=1   kA := 10<sup>3</sup>·amp   LLP := 1·tesla   (LLP units are proportional to teslas)

DF ranges from trigger site:

117.9	LA
145.1	FP
197.2	Jk (note: this range is incorrect)
259.1	Im
379.4	Sa
426.8	Qu

range := [ ] · km

Read in data:                   data := READPRN(dataorv)

nflashes := rows(data)        i := 1..nflashes

French measured peak current (kA):   i\_french<sub>i</sub> := data<sub>i,1</sub>·kA

ndfs := cols(data) - 1        j := 1..ndfs

DF signal amplitudes (LLP units):   dfamp<sub>i,j</sub> := data<sub>i,j+1</sub>·LLP

Normalized DF amplitudes to 100 km:

$$\text{normamp}_i := \frac{\sum_j \left( \text{dfamp}_{i,j} \cdot \frac{\text{range}_j}{100 \cdot \text{km}} \right)}{\sum_j (\text{dfamp}_{i,j} \neq 0)}$$

Linear regression:

$$\bar{x} := \frac{\sum_i \text{normamp}_i}{\text{nflashes}} \quad \bar{y} := \frac{\sum_i i \text{ french}_i}{\text{nflashes}}$$

$$S_{xx} := \sum_i (\text{normamp}_i - \bar{x})^2$$

$$S_{xy} := \sum_i (\text{normamp}_i \cdot i \text{ french}_i) - \text{nflashes} \cdot \bar{x} \cdot \bar{y}$$

$$S_{yy} := \sum_i (i \text{ french}_i - \bar{y})^2$$

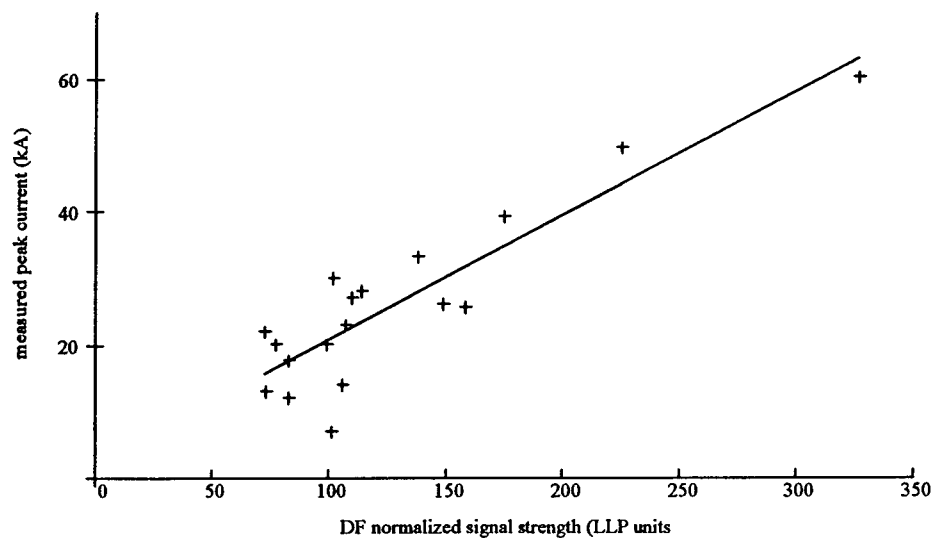
Slope, intercept, and best-fit line:

$$b := \frac{S_{xy}}{S_{xx}} \quad a := \bar{y} - \bar{x} \cdot b \quad \hat{y}(x) := a + b \cdot x$$

Correlation coefficient and standard deviation:

$$r := \frac{S_{xy}}{\sqrt{S_{xx} \cdot S_{yy}}} \quad s := \sqrt{\frac{\sum_i (i \text{ french}_i - \hat{y}(\text{normamp}_i))^2}{\text{nflashes} - 2}}$$

Measured peak current vs. DF signal strength (normalized to 100 km)



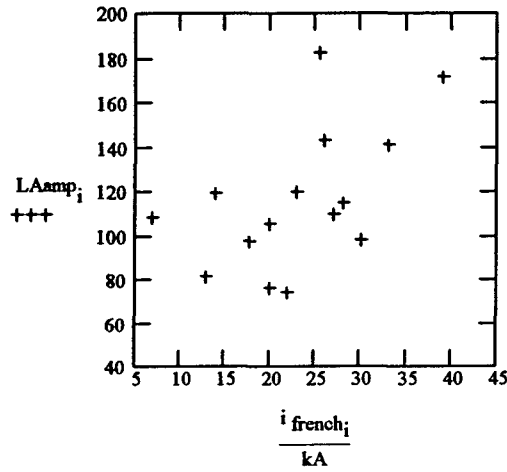
Best-fit intercept:  $a = 2.275 \cdot \text{kA}$

correlation coefficient:  $r = 0.893$

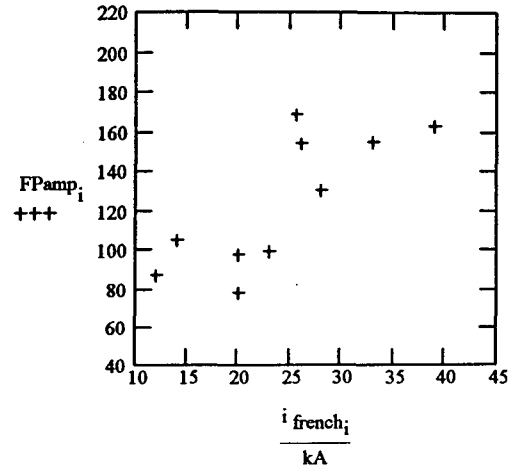
slope:  $b = 0.186 \cdot \frac{\text{kA}}{\text{LLP}}$

standard deviation:  $s = 6.132 \cdot \text{kA}$

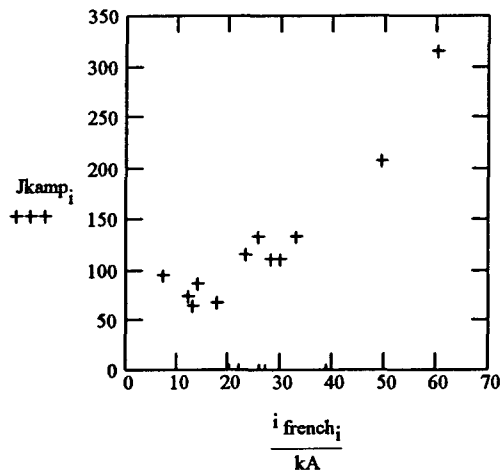
$$LAmp_i := dfamp_{i,1} \cdot \frac{range_1}{100 \cdot km}$$



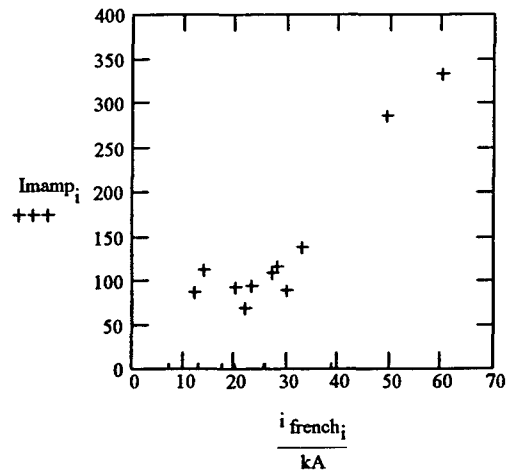
$$FPamp_i := dfamp_{i,2} \cdot \frac{range_2}{100 \cdot km}$$



$$Jkamp_i := dfamp_{i,3} \cdot \frac{range_3}{100 \cdot km}$$



$$Imamp_i := dfamp_{i,4} \cdot \frac{range_4}{100 \cdot km}$$

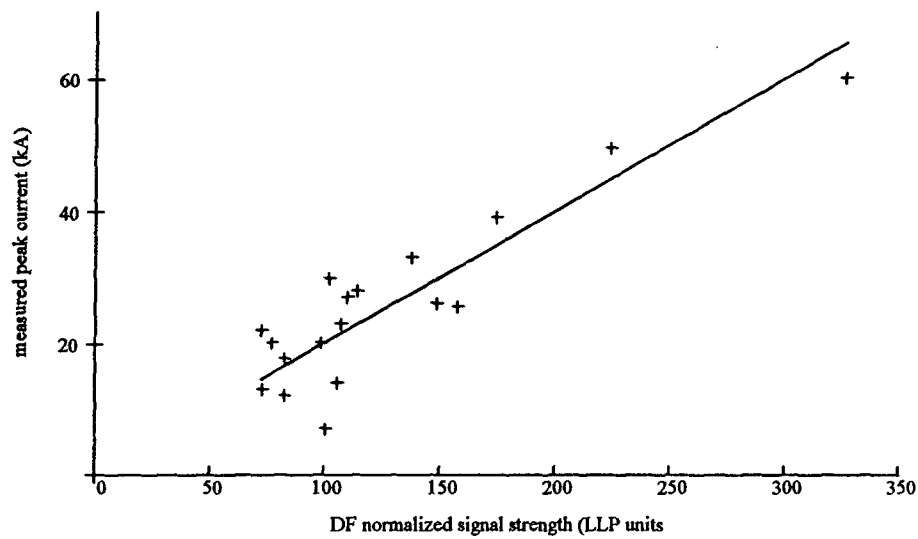


Consider driving the intercept to 0:

$$b := \frac{\sum_i \text{normamp}_i \cdot i \text{ french}_i}{\sum_i (\text{normamp}_i)^2} \quad b = 0.2 \cdot \frac{\text{kA}}{\text{LLP}} \quad \text{yhat}(x) := b \cdot x$$

$$r := \frac{S_{xy}}{\sqrt{S_{xx} \cdot S_{yy}}} \quad s := \sqrt{\frac{\sum_i (i \text{ french}_i - \text{yhat}(\text{normamp}_i))^2}{\text{nflashes} - 2}}$$

Measured peak current vs. DF signal strength (normalized to 100 km)



$$s = 6.223 \cdot \text{kA}$$

## Verification of Calibration Paper by Idone (1993)

25 June 96

Constants:   ORIGIN=1   kA :=  $10^3 \cdot \text{amp}$    LLP := 1·tesla   (LLP units are proportional to teslas)

DF ranges from trigger site:

117.9	LA
145.1	FP
220	Jk (note: this range is corrected)
259.1	Im
379.4	Sa
426.8	Qu

range :=  $\left[ \begin{array}{c} 117.9 \\ 145.1 \\ 220 \\ 259.1 \\ 379.4 \\ 426.8 \end{array} \right] \cdot \text{km}$

Read in data:                   data := READPRN(dataido)

nflashes := rows(data)        i := 1 .. nflashes

French measured peak current (kA):   i french<sub>i</sub> := data<sub>i,1</sub>·kA

ndfs := cols(data) - 1        j := 1 .. ndfs

DF signal amplitudes (LLP units):   dfamp<sub>i,j</sub> := data<sub>i,j+1</sub>·LLP

Normalized DF amplitudes to 100 km:

$$\text{normamp}_i := \frac{\sum_j \left( \text{dfamp}_{i,j} \cdot \frac{\text{range}_j}{100 \cdot \text{km}} \right)}{\sum_j (\text{dfamp}_{i,j} \neq 0)}$$

Linear regression:

$$\bar{x} := \frac{\sum_i \text{normamp}_i}{\text{nflashes}} \quad \bar{y} := \frac{\sum_i i \text{ french}_i}{\text{nflashes}}$$

$$S_{xx} := \sum_i (\text{normamp}_i - \bar{x})^2$$

$$S_{xy} := \sum_i (\text{normamp}_i \cdot i \text{ french}_i) - \text{nflashes} \cdot \bar{x} \cdot \bar{y}$$

$$S_{yy} := \sum_i (i \text{ french}_i - \bar{y})^2$$

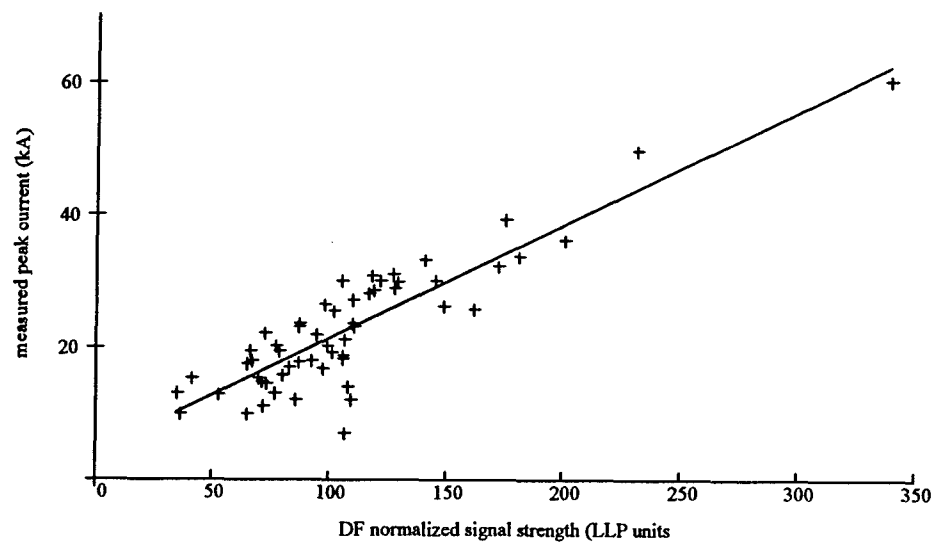
Slope, intercept, and best-fit line:

$$b := \frac{S_{xy}}{S_{xx}} \quad a := \bar{y} - \bar{x} \cdot b \quad y(x) := a + b \cdot x$$

Correlation coefficient and standard deviation:

$$r := \frac{S_{xy}}{\sqrt{S_{xx} \cdot S_{yy}}} \quad s := \sqrt{\frac{\sum_i (i \text{ french}_i - y(\text{normamp}_i))^2}{\text{nflashes} - 2}}$$

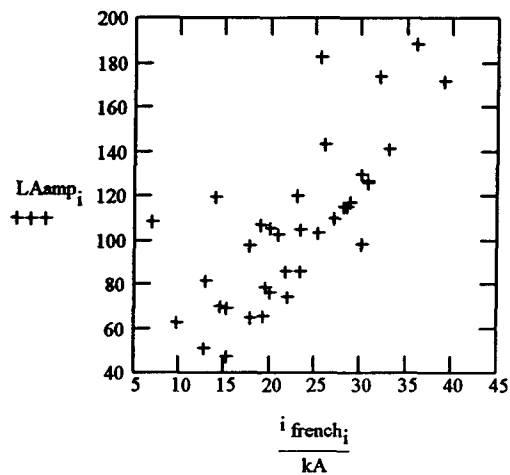
Measured peak current vs. DF signal strength (normalized to 100 km)



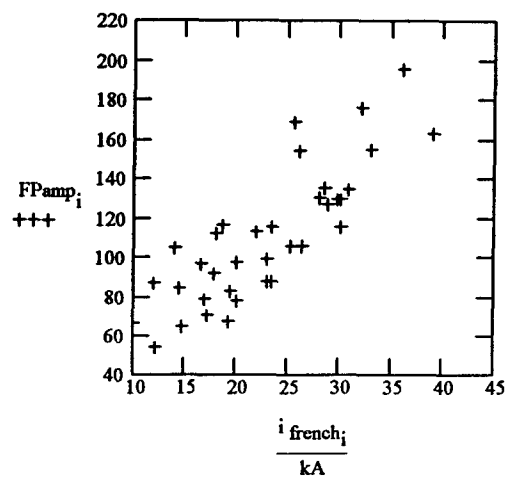
Best-fit intercept:  $a = 4.208 \cdot \text{kA}$       correlation coefficient:  $r = 0.881$

slope:  $b = 0.171 \cdot \frac{\text{kA}}{\text{LLP}}$       standard deviation:  $s = 4.649 \cdot \text{kA}$

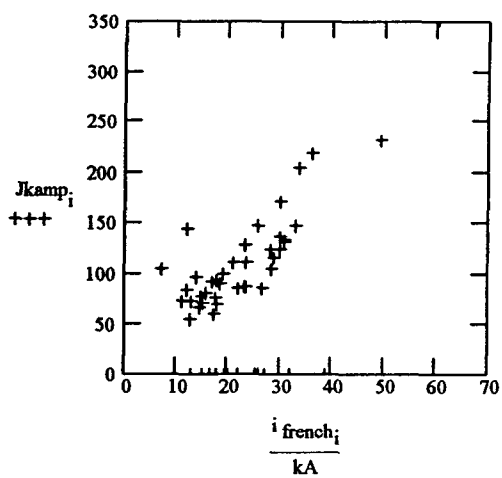
$$LAamp_i := dfamp_{i,1} \cdot \frac{range_1}{100 \cdot km}$$



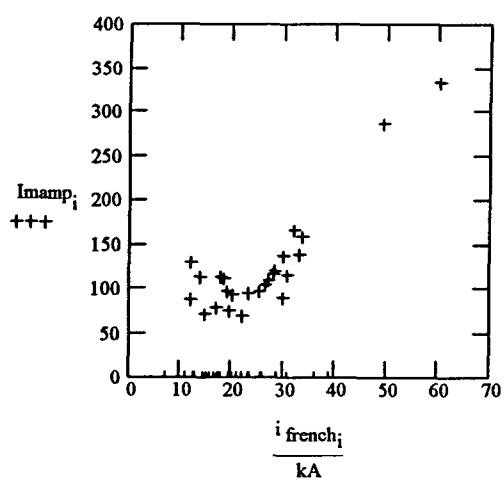
$$FPamp_i := dfamp_{i,2} \cdot \frac{range_2}{100 \cdot km}$$



$$Jkamp_i := dfamp_{i,3} \cdot \frac{range_3}{100 \cdot km}$$



$$Imamp_i := dfamp_{i,4} \cdot \frac{range_4}{100 \cdot km}$$

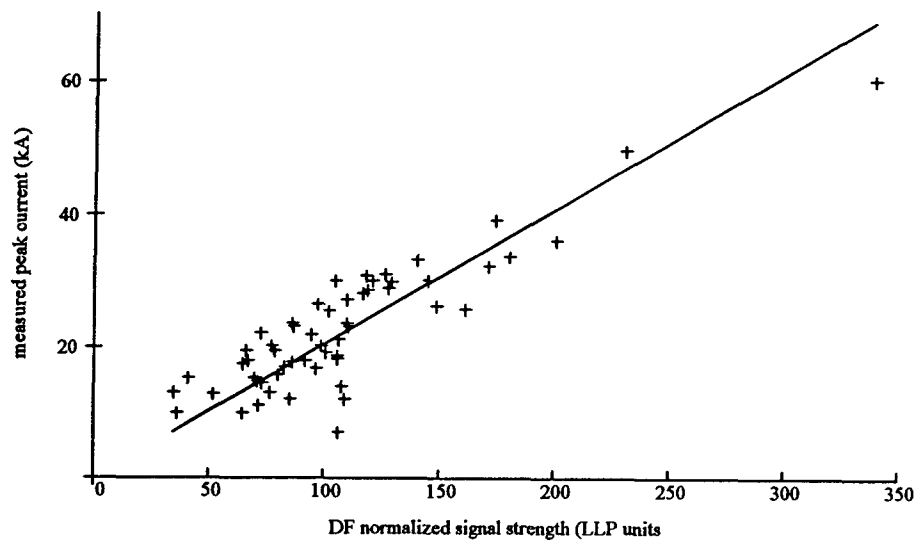


Consider driving the intercept to 0:

$$b := \frac{\sum_i \text{normamp}_i \cdot i \text{ french}_i}{\sum_i (\text{normamp}_i)^2} \quad b = 0.203 \cdot \frac{\text{kA}}{\text{LLP}} \quad \text{yhat}(x) := b \cdot x$$

$$r := \frac{S_{xy}}{\sqrt{S_{xx} \cdot S_{yy}}} \quad s := \frac{\sqrt{\sum_i (i \text{ french}_i - \text{yhat}(\text{normamp}_i))^2}}{\sqrt{\text{nflashes} - 2}}$$

Measured peak current vs. DF signal strength (normalized to 100 km)



$$s = 4.984 \cdot \text{kA}$$

## Correction to Calibration Paper by Orville (1991)

25 June 96

Constants:    ORIGIN=1    kA := 10<sup>3</sup>·amp    LLP := 1·tesla    (LLP units are proportional to teslas)

DF ranges from trigger site:

range :=	$\begin{bmatrix} 117.9 \\ 145.1 \\ 220 \\ 259.1 \\ 379.4 \\ 426.8 \end{bmatrix}$	·km	<b>LA</b> <b>FP</b> <b>Jk</b> (note: this range is corrected) <b>Im</b> <b>Sa</b> <b>Qu</b>
----------	--	-----	--

Read in data:                    data := READPRN(dataorv)

nflashes := rows(data)            i := 1 .. nflashes

French measured peak current (kA):    i french<sub>i</sub> := data<sub>i,1</sub>·kA

ndfs := cols(data) - 1            j := 1 .. ndfs

DF signal amplitudes (LLP units):    dfamp<sub>i,j</sub> := data<sub>i,j+1</sub>·LLP

Normalized DF amplitudes to 100 km:

$$\text{normamp}_i := \frac{\sum_j \left( \text{dfamp}_{i,j} \cdot \frac{\text{range}_j}{100 \cdot \text{km}} \right)}{\sum_j (\text{dfamp}_{i,j} \neq 0)}$$

Linear regression:

$$\bar{x} := \frac{\sum_i \text{normamp}_i}{\text{nflashes}} \quad \bar{y} := \frac{\sum_i i \text{ french}_i}{\text{nflashes}}$$

$$S_{xx} := \sum_i (\text{normamp}_i - \bar{x})^2$$

$$S_{xy} := \sum_i (\text{normamp}_i \cdot i \text{ french}_i) - \text{nflashes} \cdot \bar{x} \cdot \bar{y}$$

$$S_{yy} := \sum_i (i \text{ french}_i - \bar{y})^2$$

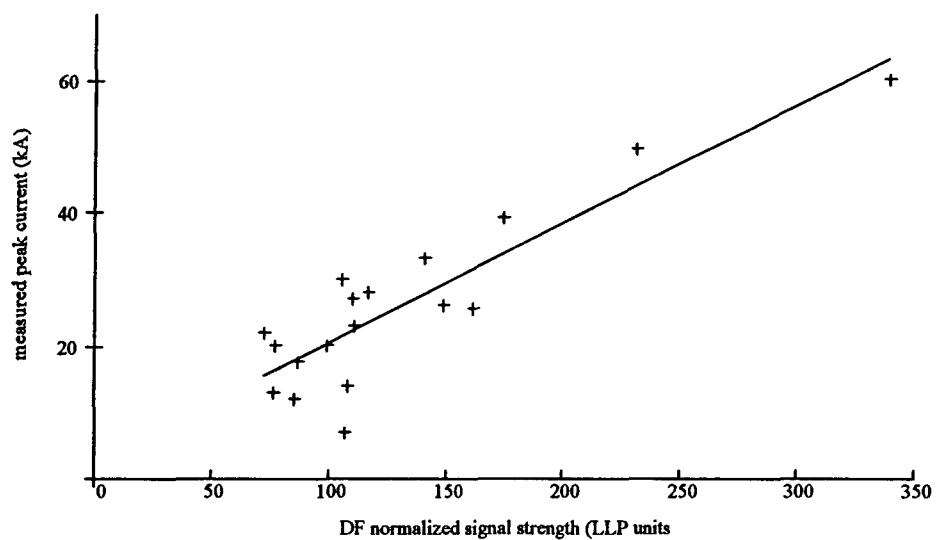
Slope, intercept, and best-fit line:

$$b := \frac{S_{xy}}{S_{xx}} \quad a := \bar{y} - \bar{x} \cdot b \quad y(x) := a + b \cdot x$$

Correlation coefficient and standard deviation:

$$r := \frac{S_{xy}}{\sqrt{S_{xx} \cdot S_{yy}}} \quad s := \frac{\sqrt{\sum_i (i \text{ french}_i - y(\text{normamp}_i))^2}}{\sqrt{\text{nflashes} - 2}}$$

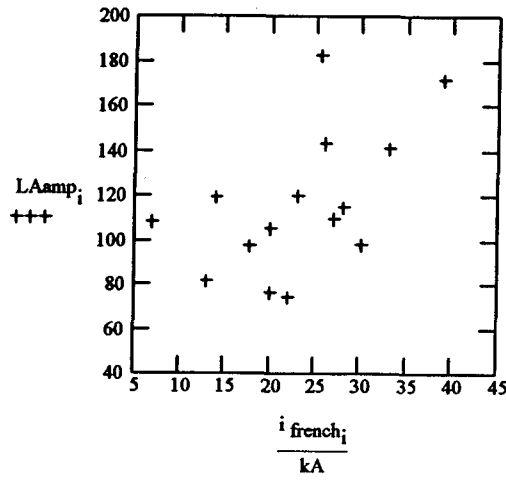
Measured peak current vs. DF signal strength (normalized to 100 km)



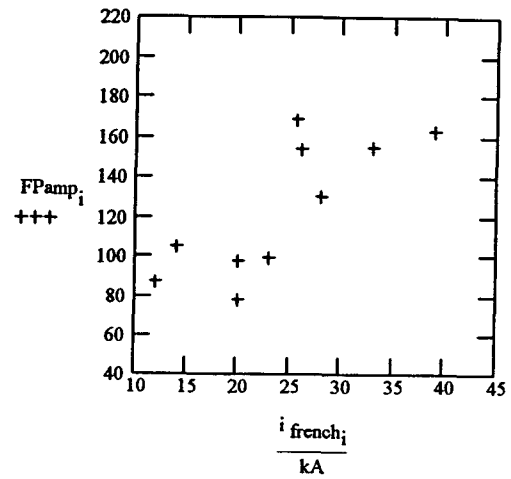
Best-fit intercept:  $a = 2.684 \cdot \text{kA}$       correlation coefficient:  $r = 0.887$

slope:  $b = 0.178 \cdot \frac{\text{kA}}{\text{LLP}}$       standard deviation:  $s = 6.304 \cdot \text{kA}$

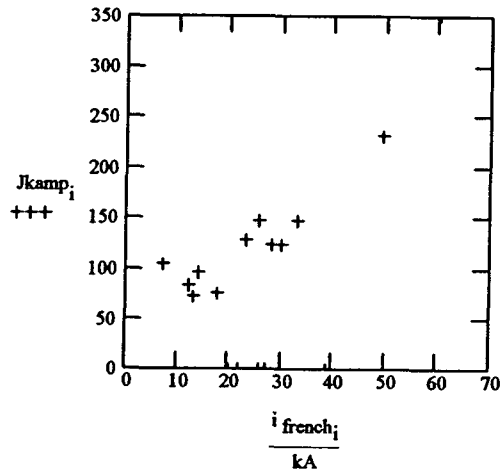
$$LAamp_i := dfamp_{i,1} \cdot \frac{range_1}{100 \cdot km}$$



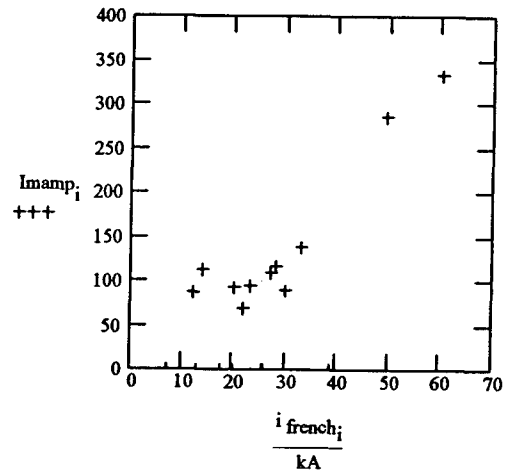
$$FPamp_i := dfamp_{i,2} \cdot \frac{range_2}{100 \cdot km}$$



$$Jkamp_i := dfamp_{i,3} \cdot \frac{range_3}{100 \cdot km}$$



$$Imamp_i := dfamp_{i,4} \cdot \frac{range_4}{100 \cdot km}$$

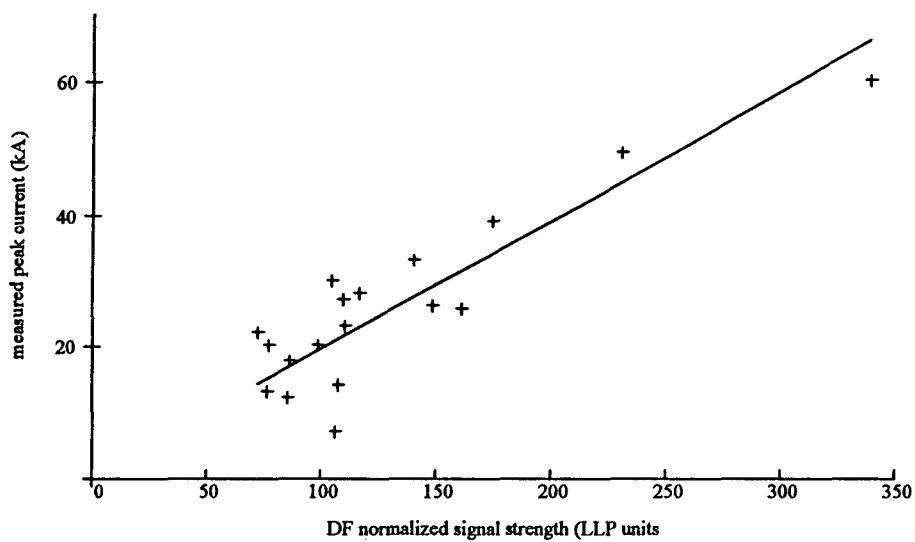


Consider driving the intercept to 0:

$$b := \frac{\sum_i \text{normamp}_i \cdot i \text{ french}_i}{\sum_i (\text{normamp}_i)^2} \quad b = 0.195 \cdot \frac{\text{kA}}{\text{LLP}} \quad \text{yhat}(x) := b \cdot x$$

$$r := \frac{S_{xy}}{\sqrt{S_{xx} \cdot S_{yy}}} \quad s := \frac{\sqrt{\sum_i (i \text{ french}_i - \text{yhat}(\text{normamp}_i))^2}}{\sqrt{\text{nflashes} - 2}}$$

Measured peak current vs. DF signal strength (normalized to 100 km)



$$s = 6.427 \cdot \text{kA}$$

**APPENDIX B****NLDN DATA ANALYSIS SAMPLE**

This appendix contains an example of the MathCAD 6.0+ files used to perform the statistical analysis presented in Chapter IV. A separate file was used for positive and negative flashes for Kansas, the Ohio Valley, and Florida, and the entire continental United States. *FLASH* and the FORTRAN code mentioned in Chapter IV were used to obtain the flash counts, mean peak currents, and peak current distributions processed by these MathCAD files.

## Statistical Summary of U.S. Negative Flashes, 1989-95

26 Jul 96

*Read in data and compute totals, means, standard deviations, and distributions*

ORIGIN=1

n := READPRN(usnneg)

number of flashes by month and year

years := cols(n)      y := 1..years

matrix indices

months := rows(n)      m := 1..months

yearsbefore := years - 2

$$ntot_y := \sum_m n_{m,y}$$

total annual flash count

$$nbar_{\text{annual}} := \frac{\sum_{y=1}^{\text{yearsbefore}} ntot_y}{\text{yearsbefore}}$$

pre-upgrade annual mean flash count

$$nsd_{\text{annual}} := \sqrt{\frac{\sum_{y=1}^{\text{yearsbefore}} (ntot_y - nbar_{\text{annual}})^2}{\text{yearsbefore}}}$$

pre-upgrade annual flash count standard deviation

$$nbar_{\text{month}_m} := \frac{\sum_{y=1}^{\text{yearsbefore}} n_{m,y}}{\text{yearsbefore}}$$

pre-upgrade monthly mean flash count

$$nsd_{\text{month}_m} := \sqrt{\frac{\sum_{y=1}^{\text{yearsbefore}} (n_{m,y} - nbar_{\text{month}_m})^2}{\text{yearsbefore}}}$$

pre-upgrade monthly flash count standard deviation

$i := \text{READPRN}(\text{usineg})$

mean peak current by month and year

$$\text{ibar}_{\text{annual}_y} := \frac{\sum_m n_{m,y} \cdot i_{m,y}}{\sum_m n_{m,y}}$$

annual mean peak current (weighted by flash count)

$$\text{isd}_{\text{annual}_y} := \sqrt{\frac{\sum_m n_{m,y} \cdot (i_{m,y} - \text{ibar}_{\text{annual}_y})^2}{\sum_m n_{m,y} - 1}}$$

annual peak current standard deviation (weighted by flash count)

$$\text{ibar}_{\text{month}_m} := \frac{\sum_{y=1}^{\text{yearsbefore}} n_{m,y} \cdot i_{m,y}}{\sum_{y=1}^{\text{yearsbefore}} n_{m,y}}$$

pre-upgrade monthly mean peak current (weighted by flash count)

$$\text{isd}_{\text{month}_m} := \sqrt{\frac{\sum_{y=1}^{\text{yearsbefore}} n_{m,y} \cdot (i_{m,y} - \text{ibar}_{\text{month}_m})^2}{\sum_{y=1}^{\text{yearsbefore}} n_{m,y} - 1}}$$

pre-upgrade monthly peak current standard deviation (weighted by flash count)

dist := READPRN(usdistr)

peak current distribution by season

bins := 4                    j := 1..bins

matrix index

$n_{\text{winter}_{j,y}} := \text{dist}_{j,y}$

seasonal flash count distributions

$n_{\text{spring}_{j,y}} := \text{dist}_{j+4,y}$

j bin  
1 <20 kA  
2 20-30 kA  
3 30-40 kA  
4 >40 kA

$n_{\text{summer}_{j,y}} := \text{dist}_{j+8,y}$

$n_{\text{autumn}_{j,y}} := \text{dist}_{j+12,y}$

$n_{\text{tot}_{j,y}} := \text{dist}_{j+16,y}$

total annual flash count distribution

$$P_{\text{winter}_{j,y}} := \frac{n_{\text{winter}_{j,y}}}{\sum_j n_{\text{winter}_{j,y}}}$$

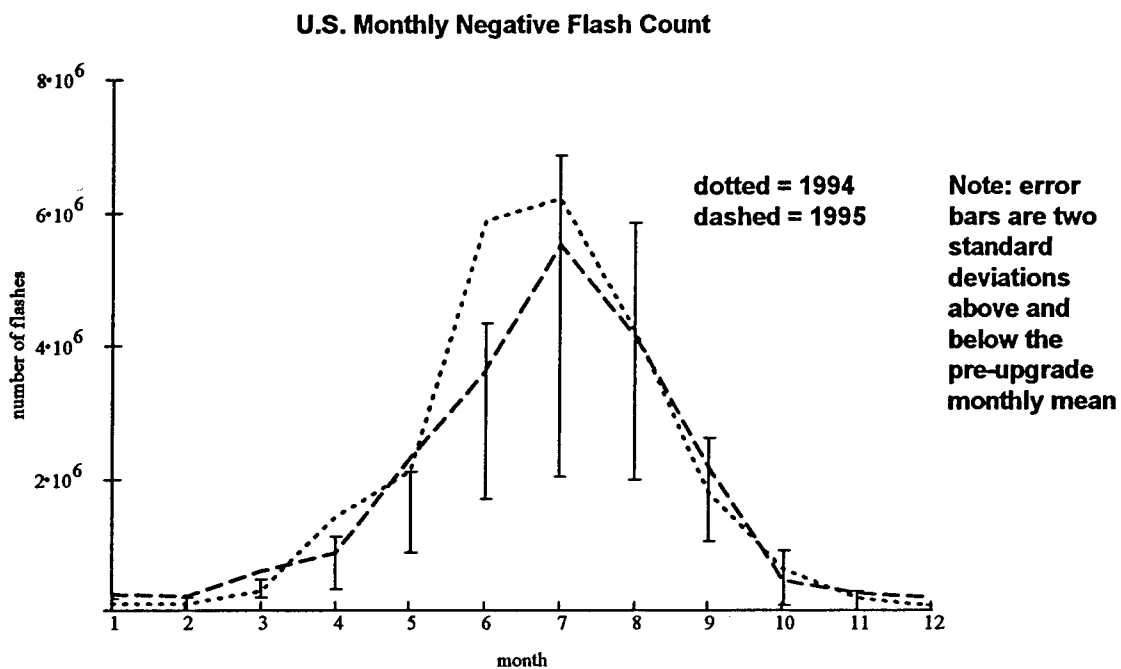
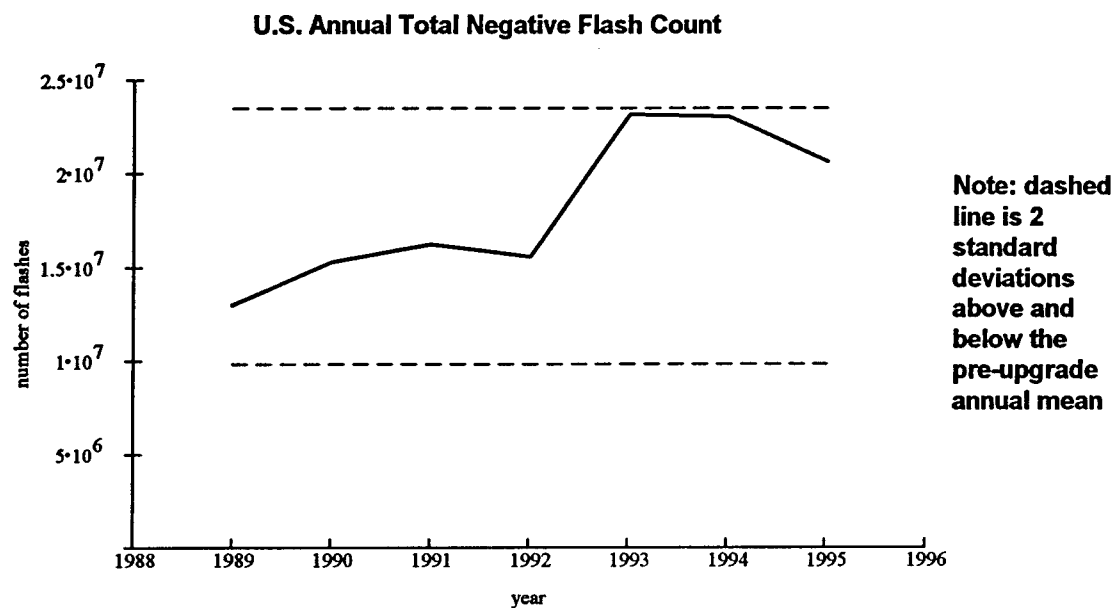
$$P_{\text{spring}_{j,y}} := \frac{n_{\text{spring}_{j,y}}}{\sum_j n_{\text{spring}_{j,y}}}$$

$$P_{\text{summer}_{j,y}} := \frac{n_{\text{summer}_{j,y}}}{\sum_j n_{\text{summer}_{j,y}}}$$

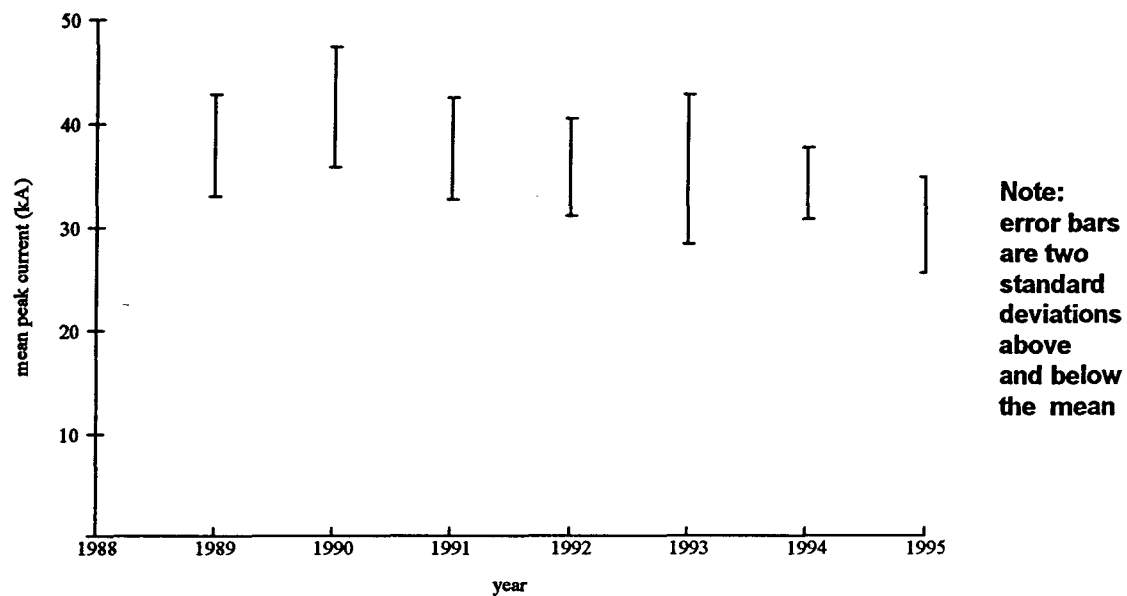
$$P_{\text{autumn}_{j,y}} := \frac{n_{\text{autumn}_{j,y}}}{\sum_j n_{\text{autumn}_{j,y}}}$$

seasonal flash count distributions  
expressed as a fraction of the annual total

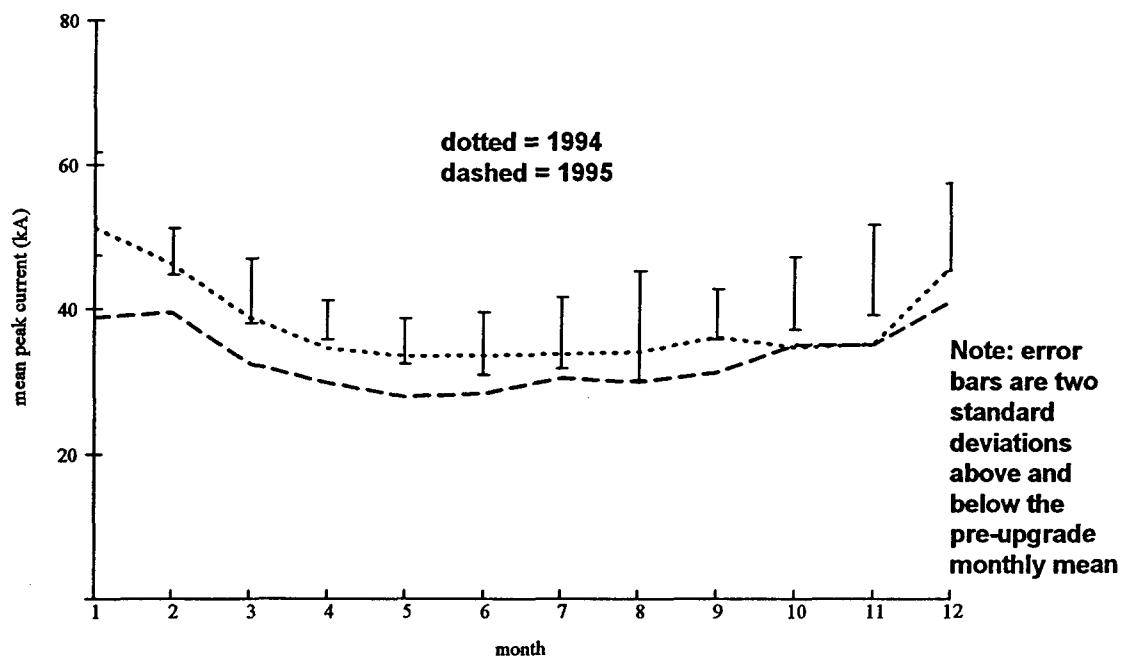
### Graphical Results



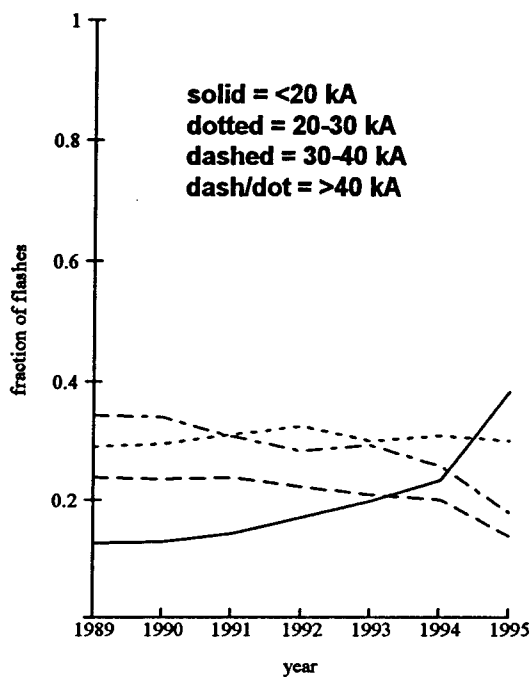
### U.S. Annual Mean Negative Peak Current



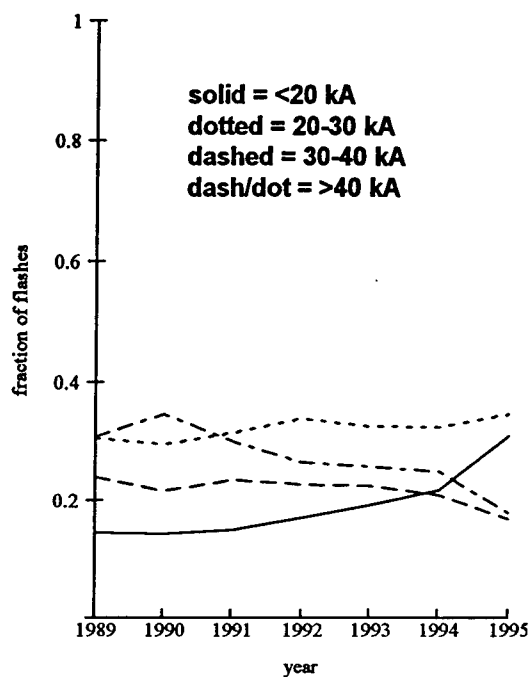
### U.S. Monthly Negative Mean Peak Current



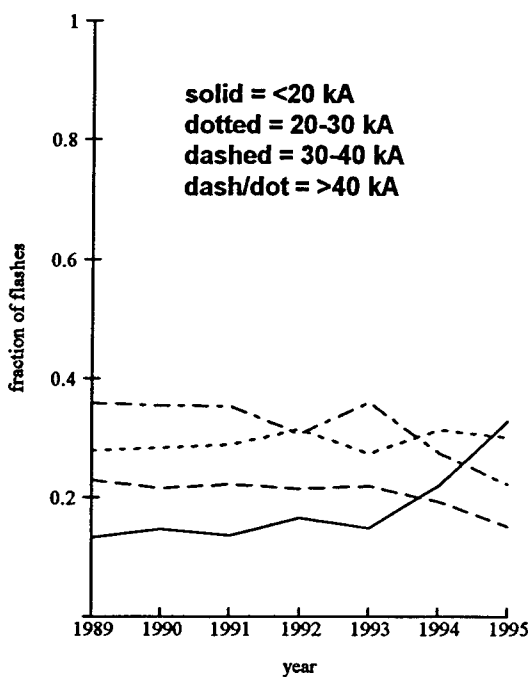
**U.S. Spring Negative Peak  
Current Distribution**



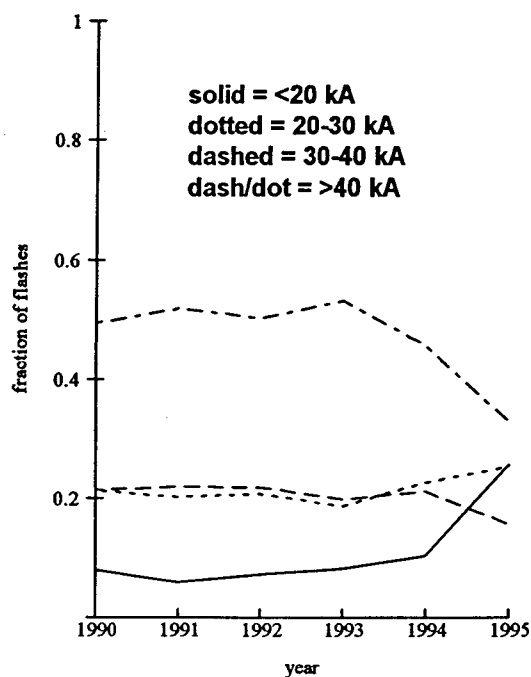
**U.S. Summer Negative Peak  
Current Distribution**



**U.S. Autumn Negative  
Peak Current Distribution**



**U.S. Winter Negative Peak  
Current Distribution**



## Supplemental stats (11/25/96):

$$\text{ibarpre} := \frac{\sum_{y=1}^{\text{yearsbefore}} \text{ibar\_annual}_y \cdot \text{ntot}_y}{\sum_{y=1}^{\text{yearsbefore}} \text{ntot}_y}$$

$$\text{isdpre} := \sqrt{\frac{\sum_{y=1}^{\text{yearsbefore}} \left[ \text{ntot}_y \cdot (\text{ibar\_annual}_y - \text{ibarpre})^2 \right]}{\sum_{y=1}^{\text{yearsbefore}} \text{ntot}_y - 1}}$$

$$Zn_y := \frac{\text{ntot}_y - \text{nbar\_annual}}{\text{nsd\_annual}}$$

$$Zi_y := \frac{\text{ibar\_annual}_y - \text{ibarpre}}{\text{isdpre}}$$

$$\text{ntot} = \begin{bmatrix} 1.3 \cdot 10^7 \\ 1.532 \cdot 10^7 \\ 1.623 \cdot 10^7 \\ 1.558 \cdot 10^7 \\ 2.313 \cdot 10^7 \\ 2.302 \cdot 10^7 \\ 2.061 \cdot 10^7 \end{bmatrix} \quad \begin{array}{l} \sum_y \text{ntot}_y = 1.269 \cdot 10^8 \\ \text{nbar\_annual} = 1.665 \cdot 10^7 \\ \text{nsd\_annual} = 3415772.271 \\ 2 \cdot \text{nsd\_annual} = 6831544.542 \end{array} \quad Zn = \begin{bmatrix} -1.069 \\ -0.389 \\ -0.124 \\ -0.314 \\ 1.895 \\ 1.865 \\ 1.159 \end{bmatrix}$$

$$\text{ibar\_annual} = \begin{bmatrix} 37.957 \\ 41.574 \\ 37.657 \\ 35.821 \\ 35.626 \\ 34.259 \\ 30.249 \end{bmatrix} \quad \text{isd\_annual} = \begin{bmatrix} 2.425 \\ 2.853 \\ 2.446 \\ 2.316 \\ 3.59 \\ 1.727 \\ 2.267 \end{bmatrix} \quad \begin{array}{l} \text{ibarpre} = 37.517 \\ \text{isdpre} = 2.144 \\ 2 \cdot \text{isdpre} = 4.287 \end{array} \quad Zi = \begin{bmatrix} 0.205 \\ 1.893 \\ 0.065 \\ -0.791 \\ -0.882 \\ -1.52 \\ -3.391 \end{bmatrix}$$

## Finite Difference Lightning Return Stroke Field Model

02 Oct 96

## Units and Constants

$$kA := 10^3 \cdot \text{amp} \quad \mu s := 10^{-6} \cdot \text{sec}$$

$$c := 3 \cdot 10^8 \frac{\text{m}}{\text{sec}} \quad \mu_0 := 4 \cdot \pi \cdot 10^{-7} \frac{\text{newton}}{\text{amp}^2} \quad \epsilon_0 := 8.85 \cdot 10^{-12} \frac{\text{coul}^2}{\text{newton} \cdot \text{m}^2} \quad \text{Electromagnetic constants}$$

$$LLP_B := 1.5 \cdot 10^{-10} \frac{\text{weber}}{\text{m}^2} \quad LLP_E := c \cdot LLP_B \quad \text{LLP Units}$$

## Return Stroke Current Model

$$i_{\text{peak}} := 30 \cdot kA \quad v := 10^8 \frac{\text{m}}{\text{sec}}$$

Return stroke peak current and wavefront velocity

$$i_{\text{mod}}(h, t) := \left[ i_{\text{peak}} \cdot e^{-\left(\frac{v \cdot t - h}{.5 \cdot \text{km}}\right)} \right] \cdot (h \leq v \cdot t)$$

Exponentially decaying current after initial breakdown peak

## Channel Parameters

$$h_{\text{min}} := 0 \cdot \text{km} \quad h_{\text{max}} := 2 \cdot \text{km} \quad nh := 40$$

Channel top and bottom heights and number of steps for integration

$$\Delta h := \frac{h_{\text{max}} - h_{\text{min}}}{nh} \quad j := 0..nh \quad h_j := h_{\text{min}} + j \cdot \Delta h \quad \text{Channel step size: } \Delta h = 50 \cdot \text{m}$$

$$\rho_0(h) := 0 \cdot \frac{\text{coul}}{\text{m}} \quad \text{Initial return stroke channel charge density}$$

## Channel Current and Charge Density

$$t_{\text{max}} := 50 \cdot \mu s \quad nt := 1000$$

Time limit and number of time steps for channel current density computation

$$\Delta t := \frac{t_{\text{max}}}{nt} \quad k := 0..nt \quad t_k := k \cdot \Delta t \quad \text{Time step size: } \Delta t = 0.05 \cdot \mu s$$

Courant condition:  $v \cdot \Delta t = 5 \cdot \text{m}$ 

$$i_{j,k} := \begin{cases} 0 \cdot kA & \text{if } j=nh \\ i_{\text{mod}}(h_j, t_k) & \text{otherwise} \end{cases}$$

Channel current (constrained to 0 at top of channel)

$$\rho_{j,0} := \rho_0(h_j)$$

Initial channel charge density

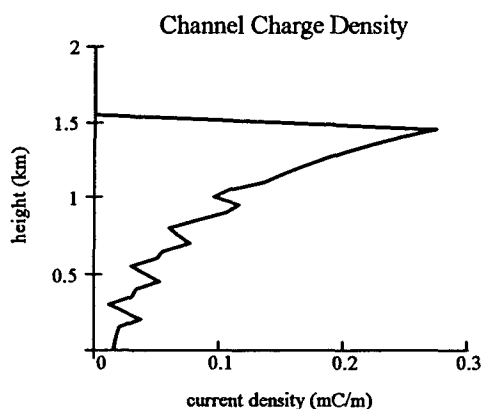
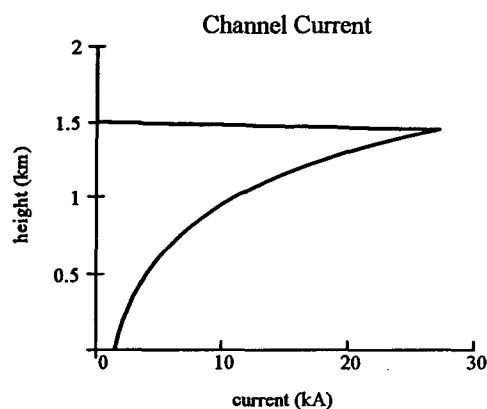
$$k := 1..nt$$

$$\rho_{j,k} := \begin{cases} \rho_{j,k-1} - \left( \frac{i_{1,k-1} - i_{0,k-1}}{\Delta h} \right) \cdot \Delta t & \text{if } j=0 \\ \rho_{j,k-1} - \left( \frac{i_{nh,k-1} - i_{nh-1,k-1}}{\Delta h} \right) \cdot \Delta t & \text{if } j=nh \\ \rho_{j,k-1} - \left( \frac{i_{j+1,k-1} - i_{j-1,k-1}}{2 \cdot \Delta h} \right) \cdot \Delta t & \text{otherwise} \end{cases}$$

Channel charge density (determined by continuity from the vertical derivative of channel current)

$$k := 300$$

$$t_k = 15 \cdot \mu\text{s}$$



### Vector and Scalar Potentials

$$R(r,h) := \sqrt{r^2 + h^2}$$

Slant range expression

$$kret(r,t,h) := \begin{cases} 0 & \text{if } \left( t - \frac{R(r,h)}{c} \right) \leq 0 \cdot \mu\text{s} \\ \text{floor} \left( \frac{t - \frac{R(r,h)}{c}}{\Delta t} \right) & \text{otherwise} \end{cases}$$

Retarded time index (accounts for time required for radiation to travel from a spot on the channel to the observer)

$$A_z(r,t) := \frac{\mu_0}{4 \cdot \pi} \sum_{j=1}^{nh} \left[ \left( \frac{i_{j,kret(r,t,h_j)} + i_{j-1,kret(r,t,h_{j-1})}}{R(r,h_j)} + \frac{i_{j-1,kret(r,t,h_{j-1})}}{R(r,h_{j-1})} \right) \cdot \left( \frac{\Delta h}{2} \right) \right] \cdot 2$$

Vertical component of the vector potential (factor of 2 accounts for image current)

$$\phi(r, z, t) := \frac{1}{4 \cdot \pi \cdot \epsilon_0} \cdot \sum_{j=1}^{nh} \left[ \left( \frac{\rho_{j, kret}(r, t, h_j - z)}{R(r, h_j - z)} + \frac{\rho_{j-1, kret}(r, t, h_{j-1} - z)}{R(r, h_{j-1} - z)} \right) \cdot \left( \frac{\Delta h}{2} \right) \dots \right. \\ \left. + \left( \frac{-\rho_{j, kret}(r, t, h_j + z)}{R(r, h_j + z)} + \frac{-\rho_{j-1, kret}(r, t, h_{j-1} + z)}{R(r, h_{j-1} + z)} \right) \cdot \left( \frac{\Delta h}{2} \right) \right]$$

Scalar potential (sum within summation accounts for image charge)

### Azimuthal Magnetic and Vertical Electric Fields

$$\Delta r := .2 \cdot \text{km}$$

Radial distance step for spatial derivative of vector potential

$$\Delta z := 1 \cdot \text{km}$$

Vertical distance step for spatial derivative of scalar potential

$$\Delta t := .5 \cdot \mu\text{s}$$

Time step for temporal derivative of vector potential

$$\text{Courant condition: } c \cdot \Delta t = 0.15 \cdot \text{km}$$

$$B\phi(r, t) := - \left( \frac{Az(r + \Delta r, t) - Az(r - \Delta r, t)}{2 \cdot \Delta r} \right)$$

Azimuthal component of the magnetic field

$$Ez(r, t) := - \left( \frac{\phi(r, \Delta z, t) - \phi(r, -\Delta z, t)}{2 \cdot \Delta z} \right) - \left( \frac{Az(r, t + \Delta t) - Az(r, t - \Delta t)}{2 \cdot \Delta t} \right)$$

Vertical component of the electric field

### Detection Criteria

$$\text{time}(r, \text{thresh}) := \left| \begin{array}{l} \text{time} \leftarrow 0 \cdot \mu\text{s} \\ t \leftarrow \frac{r}{c} \\ \text{while } t \leq \left( \frac{r}{c} + 40 \cdot \mu\text{s} \right) \\ \left| \begin{array}{l} (\text{time} \leftarrow \text{time} + 1 \cdot \mu\text{s}) \text{ if } (Ez(r, t) \geq \text{thresh}) \\ t \leftarrow t + 1 \cdot \mu\text{s} \end{array} \right. \\ \text{time} \end{array} \right.$$

Amount of time detected signal is above a given signal strength threshold at a particular range

$$\text{peak}(r) := \left| \begin{array}{l} \text{peak} \leftarrow 0 \cdot \frac{\text{weber}}{\text{m}^2} \\ t \leftarrow \frac{r}{c} \\ \text{while } t \leq \left( \frac{r}{c} + 40 \cdot \mu\text{s} \right) \\ \left| \begin{array}{l} (\text{peak} \leftarrow B\phi(r, t)) \text{ if } (B\phi(r, t) \geq \text{peak}) \\ t \leftarrow t + 1 \cdot \mu\text{s} \end{array} \right. \\ \text{peak} \end{array} \right.$$

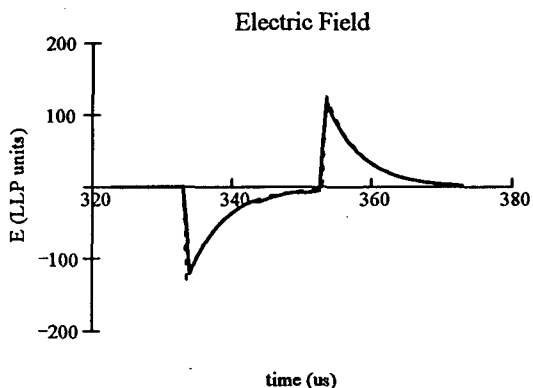
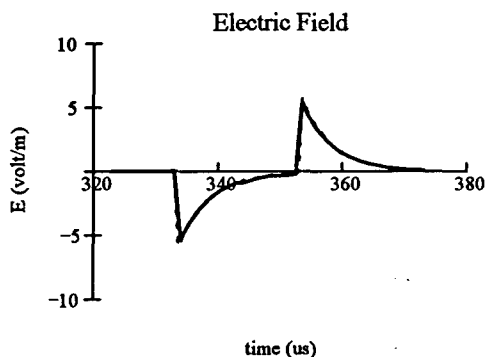
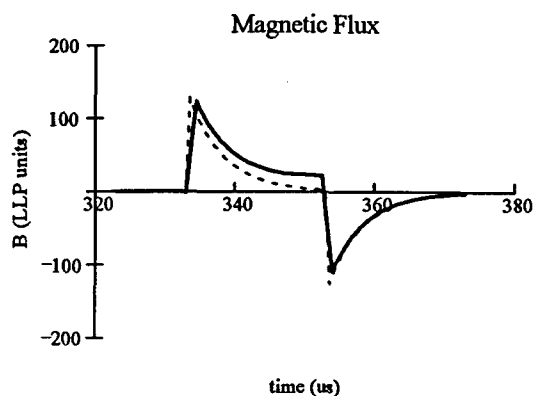
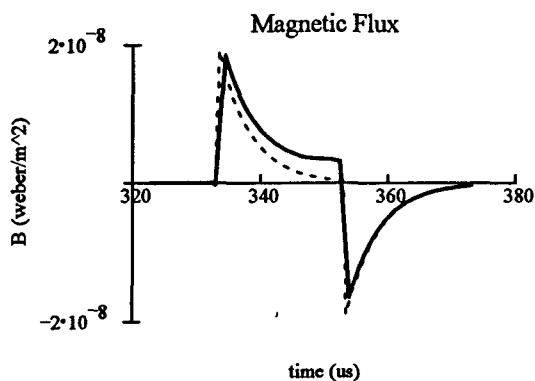
Peak (magnetic) signal strength of detected radiation

$$\text{rns}(r) := \text{peak}(r) \cdot \frac{r}{100 \cdot \text{km}}$$

Range-normalized signal strength (peak magnetic field strength normalized to 100km)

**Radiation Waveform**

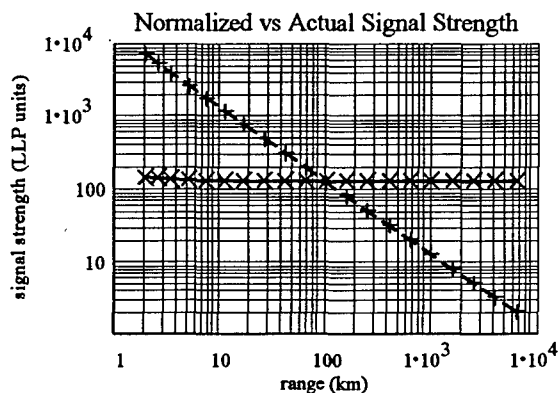
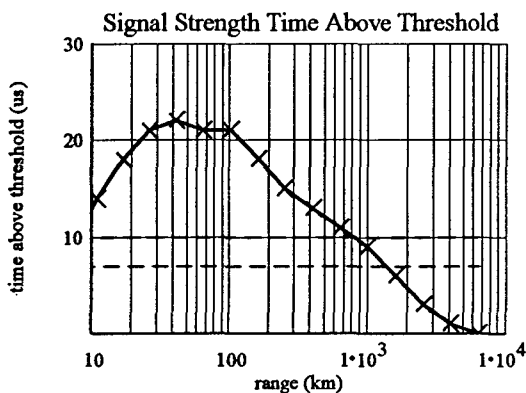
$r := 100 \cdot \text{km}$      $np := 100$   
 $p := 0..np$      $t_{\text{minplot}} := \text{floor}\left(\frac{r}{c} - 10\right) \cdot \mu\text{s}$      $dt_{\text{plot}} := \frac{t_{\text{max}}}{np}$      $t_p := t_{\text{minplot}} + p \cdot dt_{\text{plot}}$



**Signal Strength Characteristics**

$\text{thresh} := .112 \cdot \frac{\text{volt}}{\text{m}}$

$l := 0..19$      $mg_l := 1 \cdot \text{km} + 10^{\left(\frac{l}{5}\right)} \cdot \text{km}$      $dur_l := \text{time}(mg_l, \text{thresh})$      $pk_l := \text{peak}(mg_l)$      $\text{normal}_l := \text{rms}(mg_l)$



**Vital statistics:**     $\text{ipeak} = 30 \cdot \text{kA}$      $mg_{14} = 631.957 \cdot \text{km}$      $dur_{14} = 11 \cdot \mu\text{s}$      $\text{normal}_{14} = 126.638 \cdot \text{LLP}_B$   
 $mg_{15} = 1.001 \cdot 10^3 \cdot \text{km}$      $dur_{15} = 9 \cdot \mu\text{s}$      $\text{normal}_{15} = 126.617 \cdot \text{LLP}_B$

## APPENDIX C

### FINITE DIFFERENCE FIELD MODEL

This appendix contains the MathCAD 6.0+ file used in the return stroke radiation model discussed in Chapter V. The user supplies the return stroke model characteristics as a function of time and height and the model computes the electromagnetic fields radiated by the return stroke, the raw and normalized signal strength vs. range, and the signal pulsewidth vs. range. Multiple runs of this model using return strokes of various peak currents produces the detection range vs. peak current relation used in the detection model.

**APPENDIX D****STOCHASTIC DETECTION MODEL**

This appendix contains the MathCAD 6.0+ file used to model return stroke detection with pulsewidth detection criteria of 10  $\mu$ s and 7  $\mu$ s. It generates a large number of randomly located return strokes with random peak currents and determines the flash count distributions of detected flashes using each detection criterion.

## Return Stroke Radiation Detection Model

04 Oct 96

## Units and Constants

$$kA := 10^3 \cdot \text{amp} \quad LLP_B := 1.5 \cdot 10^{-10} \cdot \frac{\text{weber}}{\text{m}^2} \quad \text{ORIGIN} = 1$$

## Data from Previous Finite Difference Model Runs

peak currents

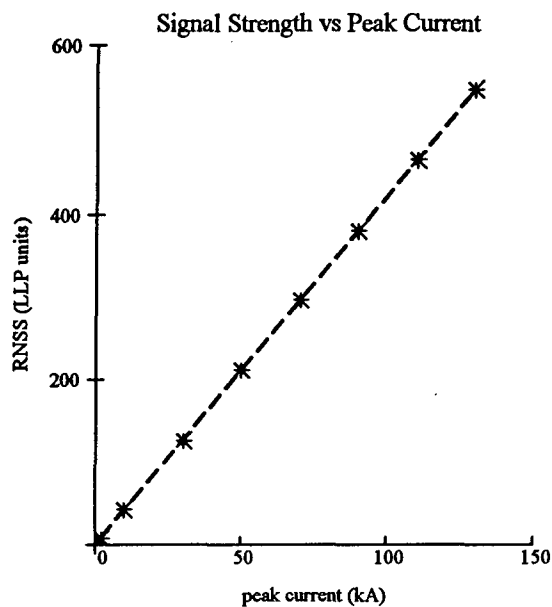
ranges and range-normalized signal strengths

ipeak :=	$\begin{bmatrix} 2 \\ 10 \\ 30 \\ 50 \\ 70 \\ 90 \\ 110 \\ 130 \end{bmatrix} \cdot kA$	rng10 :=	$\begin{bmatrix} 40.811 \\ 252.189 \\ 631.957 \\ 1.001 \cdot 10^3 \\ 1.586 \cdot 10^3 \\ 1.586 \cdot 10^3 \\ 2.513 \cdot 10^3 \\ 2.513 \cdot 10^3 \end{bmatrix} \cdot km$	rng7 :=	$\begin{bmatrix} 64.096 \\ 399.107 \\ 1.001 \cdot 10^3 \\ 2.513 \cdot 10^3 \\ 2.513 \cdot 10^3 \\ 3.982 \cdot 10^3 \\ 3.982 \cdot 10^3 \\ 6.311 \cdot 10^3 \end{bmatrix} \cdot km$				
						mss10 :=	$\begin{bmatrix} 8.496 \\ 42.24 \\ 126.638 \\ 211.029 \\ 295.411 \\ 379.814 \\ 464.187 \\ 548.585 \end{bmatrix} \cdot LLP_B$	mss7 :=	$\begin{bmatrix} 8.475 \\ 42.223 \\ 126.617 \\ 210.994 \\ 295.392 \\ 379.774 \\ 464.169 \\ 548.549 \end{bmatrix} \cdot LLP_B$

i := 1..rows(ipeak)

counting index for data

## Graphical Results



Best-fit parameters for 10us threshold

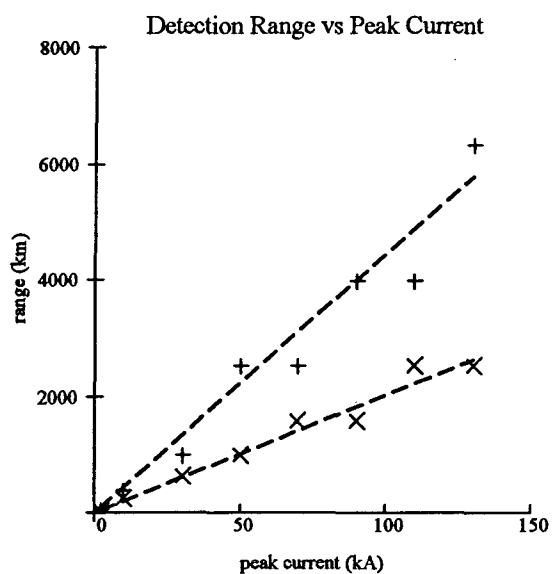
$$\text{slope(ipeak, rns10)} = 4.219 \cdot \frac{\text{LLP}_B}{\text{kA}}$$

$$\text{intercept(ipeak, rns10)} = 0.053 \cdot \text{LLP}_B$$

Best-fit parameters for 7us threshold

$$\text{slope(ipeak, rns7)} = 4.219 \cdot \frac{\text{LLP}_B}{\text{kA}}$$

$$\text{intercept(ipeak, rns7)} = 0.033 \cdot \text{LLP}_B$$



Best-fit parameters for 10us threshold

$$\text{slope(ipeak, rng10)} = 20.062 \cdot \frac{\text{km}}{\text{kA}}$$

$$\text{intercept(ipeak, rng10)} = 31.667 \cdot \text{km}$$

Best-fit parameters for 7us threshold

$$\text{slope(ipeak, rng7)} = 44.305 \cdot \frac{\text{km}}{\text{kA}}$$

$$\text{intercept(ipeak, rng7)} = -129.128 \cdot \text{km}$$

## Model Detection Efficiency Calculations

### Predefined functions

$$\text{detectrng10}(i) := \text{slope}(\text{ipeak}, \text{mg10}) \cdot i$$

$$\text{detectrng7}(i) := \text{slope}(\text{ipeak}, \text{mg7}) \cdot i$$

$$\text{mg}(x1, y1, x2, y2) := \sqrt{(x1 - x2)^2 + (y1 - y2)^2}$$

Maximum detection range as a function of return stroke peak current at 10 and 7 $\mu$ s thresholds

Distance formula

### Model Parameters

$$\text{dfx} := \begin{pmatrix} -125 \\ 125 \end{pmatrix} \cdot \text{km} \quad \text{dfy} := \begin{pmatrix} 0 \\ 0 \end{pmatrix} \cdot \text{km}$$

$$\text{ndfs} := \text{rows}(\text{dfx})$$

$$\text{nflashes} := 10^5 \quad i := 1 \dots \text{nflashes}$$

$$x := \text{morm}(\text{nflashes}, 0, 500) \cdot \text{km}$$

$$y := \text{morm}(\text{nflashes}, 0, 500) \cdot \text{km}$$

$$\text{current}_i := \text{md}(100) \cdot \text{kA}$$

DF locations

Number of dfs

Number of flashes

Flash location distribution

Flash current distribution

### Detection Determination

$$j := 1 \dots \text{ndfs}$$

$$\text{dist}_{i,j} := \text{mg}(x_i, y_i, \text{dfx}_j, \text{dfy}_j)$$

$$\text{detect10}_i := \left[ \prod_j (\text{dist}_{i,j} \leq \text{detectrng10}(\text{current}_i)) \right] \cdot \text{current}_i$$

$$\text{detect7}_i := \left[ \prod_j (\text{dist}_{i,j} \leq \text{detectrng7}(\text{current}_i)) \right] \cdot \text{current}_i$$

Distance from flash to each df

Determine if range from flash to each df is less than detection range at each threshold—if so, then the flash is detected

**Flash Detection Histogram**

$$n := 1..100$$

$$ipeak_n := n \cdot kA$$

$$htot := hist(ipeak, current)$$

$$h10 := hist(ipeak, detect10)$$

$$h7 := hist(ipeak, detect7)$$

$$n := 1..99$$

$$eff10_n := \frac{h10_n}{htot_n} \quad eff7_n := \frac{h7_n}{htot_n}$$

$$frac_n := \begin{cases} \frac{h7_n}{h10_n} & \text{if } h10_n \neq 0 \\ 0 & \text{otherwise} \end{cases}$$

$$mean10 := \frac{\sum_n h10_n \cdot ipeak_n}{\sum_n h10_n}$$

$$mean7 := \frac{\sum_n h7_n \cdot ipeak_n}{\sum_n h7_n}$$

Peak current bins for histogram

Total number of flashes vs peak current

Number of flashes detected vs peak current with 10 and 7us thresholds

Detection efficiency expressed as percent of flashes detected at 10us and 7us thresholds

Number of flashes detected at 7us threshold expressed as a fraction of number of flashes detected at 10us threshold

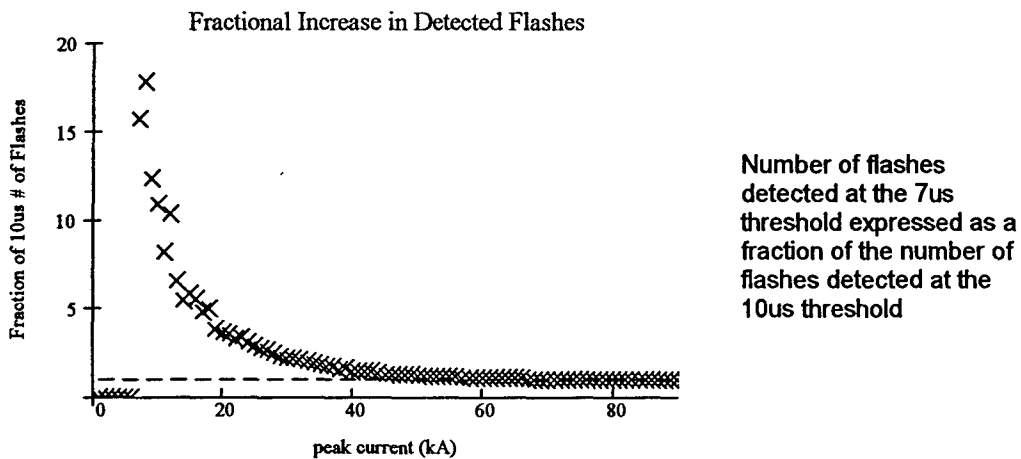
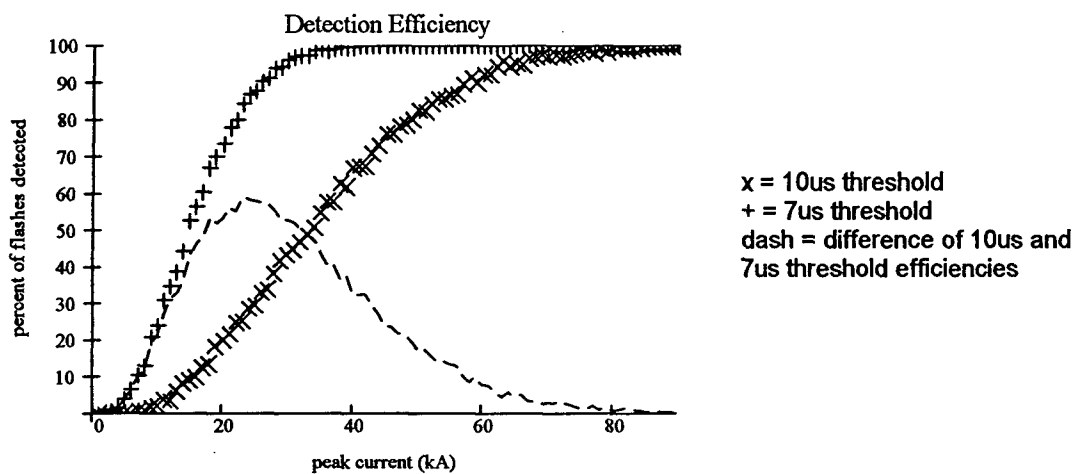
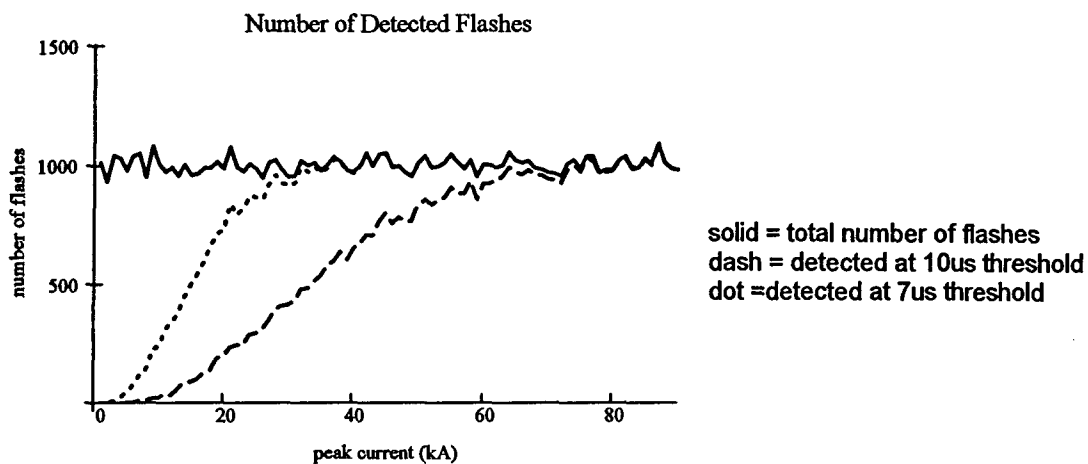
Mean peak current of detected flashes at 10us threshold

$$mean10 = 65.3 \cdot kA$$

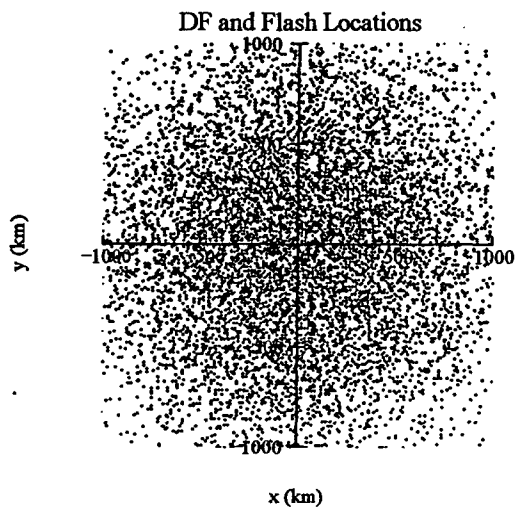
Mean peak current of detected flashes at 7us threshold

$$mean7 = 57.381 \cdot kA$$

Graphical Results



ii := 10,20..10<sup>5</sup>



DF locations (x's) and  
locations of every tenth  
randomly generated flash

## VITA

Robert Scott Wacker [REDACTED],  
[REDACTED] and grew up in Wichita, Kansas, where he graduated  
from Northwest High School in May 1991. He attended the  
United States Air Force Academy and in May 1995 earned a  
bachelor of science in physics and a commission as a second  
lieutenant in the United States Air Force. He studied at  
Texas A&M University during 1995-96 under a Fannie and John  
Hertz Foundation fellowship. His next assignment takes him  
to Kadena Air Base, Okinawa, where he will serve as a  
weather officer. His interests include flying and golf.  
Permanent address: 1616 Valleyview Ct., Wichita, KS, 67212.